A feasibility test for measuring the proton charge radius in high-energy muon-proton elastic scattering

Martin Hoffmann

Masterarbeit in Physik
angefertigt im Helmholtz-Institut für Strahlen- und Kernphysik

vorgelegt der
Mathematisch-Naturwissenschaftlichen Fakultät
der
Rheinischen Friedrich-Wilhelms-Universität
Bonn

Mai 2019

I hereby declare that this thesis was formulated by myself and that no sources or tools other than those cited were used.

Bonn, ...
Date   Signature

1. Gutachter: Prof. Dr. Bernhard Ketzer
2. Gutachter: Prof. Dr. Reinhard Beck

Acknowledgements

I would like to thank my supervisor Professor Bernhard Ketzer for the possibility to research on such an exciting experiment and the great help in case of a problem.

Furthermore, I am very thankful that Professor Reinhard Beck accepted to be the second reviewer.

I want to thank the proton radius subgroup of the COMPASS collaboration, especially Christian Dreisbach for the very informative and pleasant time during the measurement and for answering my questions about details of the experimental setup. Additionally, I want to thank Alexander Inglessi for answering all my questions about the setup and analysis of the time projection chamber.

I want to thank Mathias Wagner for all the fruitful discussions and the great help in general.

I would like to thank my friends and colleagues for all the support.

I am grateful for the support from my family.

Contents

CHAPTER 1

Introduction

Stable matter is composed of protons, neutrons and electrons. Accordingly, the proton has a large importance for various researches. The magnetic moment of orthohydrogen was measured in 1933 by Frisch to have a value of 2 to 3 nuclear magnetic moments [1]. This was the first hint that a proton is not a point-like particle, but has a substructure instead. Therefore, it has to have a finite size. The proton charge radius was measured with electron-proton scattering by several experiments, which led to a CODATA value of (0.8751 ± 0.0061) fm in 2016 [2]. Measurements with hydrogen spectroscopy yield a CODATA value of (0.8759 ± 0.0077) fm [2]. The CREMA collaboration has measured the proton charge radius with muonic hydrogen spectroscopy in 2010 to be (0.84184 ± 0.00067) fm and 2013 to be (0.84087 ± 0.00039) fm [3, 4]. The results of the measurement with muonic hydrogen are more precise than results from hydrogen spectroscopy, as the distance between the muon and the proton is smaller than the Bohr radius, leading to a larger sensitivity to the substructure of the proton. This has led to a 5.6 σ-discrepancy to the 2014-CODATA value [2]. As electrons and muons behave equally according to the standard model, this large discrepancy between the measurements is very surprising and became known as the "proton radius puzzle", which is illustrated in figure 1.1. There are two spectroscopy measurements on ordinary hydrogen that were published after the 2016-CODATA value, one of which is in agreement with the result of muonic hydrogen spectroscopy [5] [6]. There are several explanations for the discrepancy within the standard model, namely a wrong determination of the Rydberg constant, radiative corrections and the two-photon exchange [7]. The proton charge radius in an elastic scattering experiment is determined with the slope of the electric form factor at a momentum transfer of 0. As the form factor can be measured only to a certain momentum transfer larger than 0, the extraction of the radius depends on the fit model. This is emphasized by several working groups fitting the same data extracted by the Mainz A1 collaboration and extracting different results [8]. This model dependency can be reduced by measuring down to the smallest possible momentum transfer. One explanation beyond the standard model is a violation of the lepton universality.

There is a wide experimental effort in order to study different effects, which is shortly summarized in the following.

The PRad experiment at the Jefferson Lab wants to measure the form factor with electron-proton scattering down to a momentum transfer of $2 \times 10^{-4}\,\mathrm{GeV}^2$. The scattering angle has to be determined with a precision of 10 µrad, which should be achieved with a windowless target [9].

An experiment with muons and electrons up to momenta of 210 MeV is planned by the Paul

Scherrer Institute [10]. This experiment should yield a good systematic comparison between muon- and electron-proton elastic-scattering. The momentum transfer should be measured between 0.0016 to 0.0820 GeV^2 for electrons and between 0.0016 to 0.0799 GeV^2 for muons.

The OLYMPUS experiment at DESY has aimed to study the impact of the hard two-photon exchange on the elastic electron-proton cross section. The ratio of elastic positron-proton and electron-proton scattering was measured with a precision of 1 % up to momentum transfers of 2.2 GeV^2, recommending to measure the elastic electron-proton cross section to even higher momentum transfers [11].

The A1 collaboration at the Mainz university accelerator MAMI aims to measure the form factors between 0.001 to 0.040 GeV^2 with a low-intensity electron beam. The recoil proton is detected with an active hydrogen target. The direct measurement of the recoil proton constraints radiative corrections. The differential cross section is measured absolutely [12].

The COMPASS++/AMBER-collaboration plans to measure the proton charge radius with a 60 or 100 GeV muon beam in 2022/2023 [13][14]. Similar to the experiment at MAMI, an active hydrogen target is used in order to overconstrain the reaction. The spectrometer is used to select scattering events in the target region and the active target gives precise information about the recoil proton kinematics, which limits the uncertainty on the momentum transfer. Using this information, the elastic muon-proton cross section can be measured in the momentum-transfer range between 0.001 to 0.020 GeV^2 with discussions to extend this range to 0.040 GeV^2. The experiment should run with a trigger-less readout, as triggering on the recoil proton could lead to a efficiency, which depends on the momentum transfer. Then one could use a veto trigger, if the scattering angle of the muon is below 5 µrad. To verify the working principle of this experiment, a test measurement was conducted in 2018.

The setup of this test measurement was positioned at the end of the COMPASS spectrometer located at the M2 beam line at CERN. The setup is made up of eight double-sided silicon tracking detectors and a **T**ime **P**rojection **C**hamber (TPC) filled with hydrogen gas, functioning as an active target. The setup and especially the duration of the measurement is not designed to yield a value for the proton charge radius. Challenges of the experiment are the extremely small scattering angles of the muon, requiring a high precision of the silicon tracking stations. The detection of low-energy recoil protons is a challenge for the TPC together with background due to a wide muon beam, as the used TPC was built for a thin electron beam at MAMI.

As part of this thesis, the following analyses are performed. The data of the silicon tracking station is used to select events in the active readout area of the TPC. Therefore, the resolution of the silicon tracking stations has to be measured and improved. The energy and direction of the recoil proton in the TPC should be measured. To achieve this, a tracking algorithm for the TPC data is written.

Since both detector systems have their own data acquisition, one has to combine the data sets in order to have full information about the scattering process. This can be done using the time stamps of the events. As the combination of independent data acquisitions should be verified, correlations between parameters, that can be measured by both systems, have to be checked. These parameters are the energy and the direction of the recoil proton. The drift velocity can be checked as well through the time difference between both systems and the interaction vertex.

Monte-Carlo simulations are performed to have a comparison for the expected performance of the detectors. These simulations are mainly focussing on the resolution of the silicon tracking stations which is determined from multiple scattering and the intrinsic detector resolution. A simple TPC response is introduced in order to study the expected correlation parameters for the proton direction and energy.

The results are discussed and possible improvements for the experiment in 2022/2023 are presented.

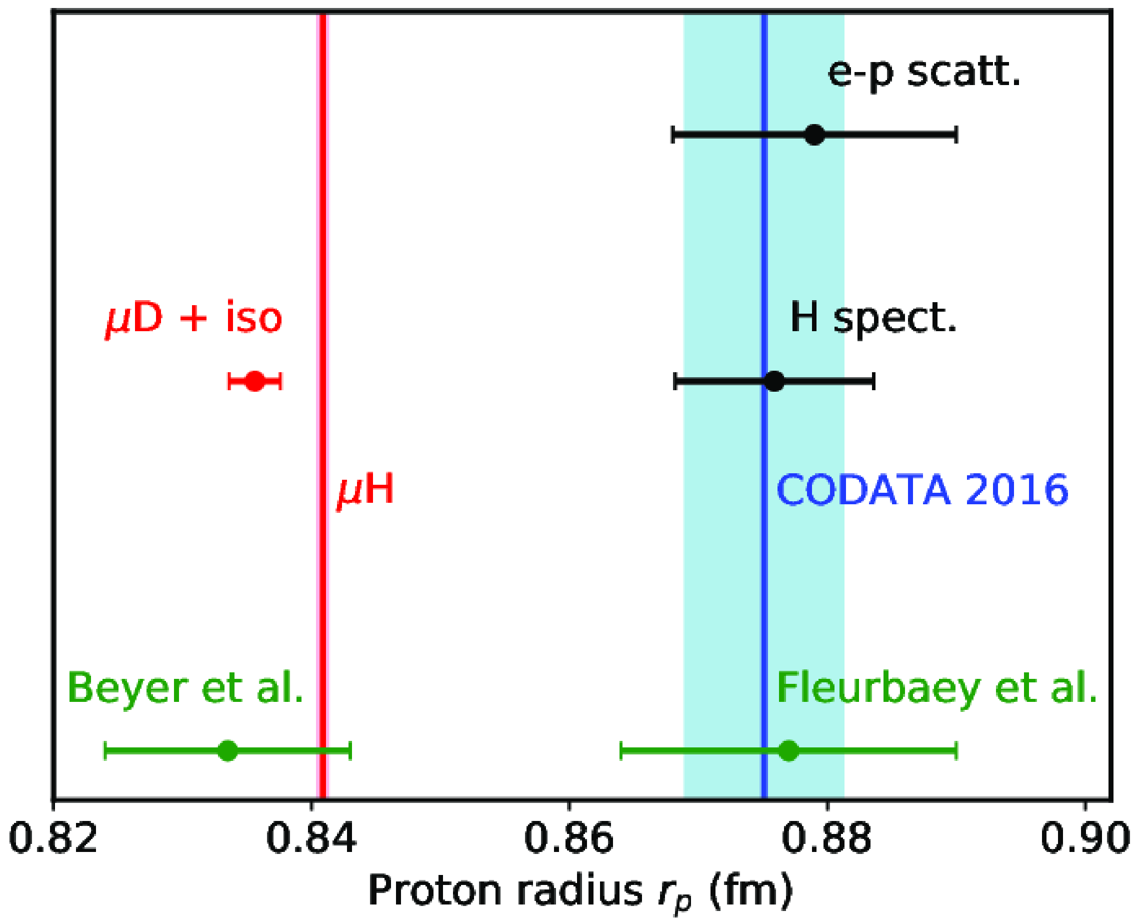

Figure 1.1: The picture shows the status of the proton radius puzzle in 2018 [15]. Results from hydrogen spectroscopy that were published after the 2016-CODATA value are marked in green. The blue line shows the CODATA-2016 recommended value for the proton charge radius, excluding the measurements with muonic hydrogen, which are marked in red.

CHAPTER 2

Theoretical background

In this chapter, a short overview over the Mott and Rosenbluth parametrization of the elastic scattering cross section is given. The formula to extract the proton charge radius from the form factor is presented. A detailed discussion can be found in [16]. The Feynman diagram of the process is pictured in figure 2.1.

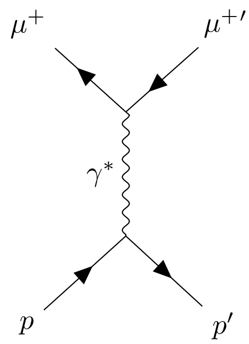

Figure 2.1: This is the Feynman diagram of the elastic scattering process.

2.1 Rosenbluth cross section

The Mott cross section describes the elastic scattering of a point-like particle with spin on a spinless target with finite mass:

$$\left(\frac{d\sigma}{d\Omega}\right)_{\text{Mott}} = 4 \cdot \alpha^2 \cdot (\hbar c)^2 \cdot E_\mu'^2 \cdot (\cos(\theta/2))^2 \cdot \frac{E_\mu'}{E_\mu} \frac{1}{Q^4} \tag{2.1}$$

with the negative squared four-momentum transfer Q^2:

$$Q^2 = -\left(p_\mu - p_\mu'\right)^2 = 2\left(E_\mu E_\mu' - |\vec{p_\mu}||\vec{p_\mu'}|\cos(\theta) - m_\mu^2\right) \quad . \tag{2.2}$$

Here, α is the fine-structure constant; $\hbar$ the reduced Planck constant; c the speed of light; E_μ and E_μ' the energy of the incoming and scattered muon, respectively; θ the scattering angle of the muon in the lab frame; p_μ, $\vec{p_\mu}$, p'_μ, $\vec{p'_\mu}$ the four-momentum and three-momentum of the incoming and scattered muon, respectively; and m_μ the mass of the muon.

One has to include the electric and magnetic form factors G_E and G_M of the target, which depends on the target spin and substructure. This is done in the Rosenbluth formula:

$$\left(\frac{d\sigma}{d\Omega}\right)_{\text{Rosenbluth}} = \left(\frac{d\sigma}{d\Omega}\right)_{\text{Mott}} \cdot \left(\frac{G_E^2(Q^2) + \tau \cdot G_M^2(Q^2)}{1+\tau} + 2\tau \cdot G_M^2(Q^2) \cdot \tan^2(\theta/2)\right) \tag{2.3}$$

with $\tau = \frac{Q^2}{4 \cdot m_p^2}$. For protons, which are the targets in our case, the form factor can be approximated by the dipole form factor:

$$\frac{G_M^p(Q^2)}{Q_M^p(Q^2=0)} = \frac{G_E^p(Q^2)}{Q_E^p(Q^2=0)} = \left(1 + \frac{Q^2}{0.71\ \text{GeV}^2}\right)^{-2} \tag{2.4}$$

with $G_M^p(Q^2 = 0) = 2.793$ and $G_E^p(Q^2 = 0) = 1$ and the parameter $0.71\,\text{GeV}^2$ is extracted from electron scattering.

2.2 Extracting the proton charge radius from a scattering experiment

The charge radius can be extracted from the slope of the electric form factor at $Q^2 = 0$:

$$\langle r^2 \rangle = -6\hbar^2 \left.\frac{dG_E(Q^2)}{dQ^2}\right|_{Q^2=0} . \tag{2.5}$$

Using the dipole form factor, this results in $\langle r^2 \rangle \approx (0.81\ \text{fm})^2$.

By measuring the cross section over a wide Q^2-range, parametrizations with higher orders of Q^2 can be made. This reduces the systematic error on the slope due to a better determination of the magnetic form factor. The up to now most elaborate parametrization is used at MAMI [17].

CHAPTER 3

Setup of the 2018 test measurement

In this chapter the setup of the test experiment is described. The working principle of the used detector systems is explained and the beam parameters like the energy, the position and the beam slope are shown. In addition, the effect of multiple scattering and the expected number of events is estimated.

3.1 COMPASS at CERN

The **CO**mmon **M**uon **P**roton **A**pparatus for **S**tructure and **S**pectroscopy (COMPASS) located at the European Organization for Nuclear Research (CERN) in Geneva is a fixed target experiment aiming to study the structure of hadrons. A proton beam is extracted from the **S**uper **P**roton **S**ynchrotron (SPS) and focused on a primary target creating a high intensity pion or muon beam. This beam is directed onto the COMPASS target. After this the 60 m long spectrometer will reconstruct energy, momentum and initial vertices of the reaction products.

The test experiment is located at the end of COMPASS and does not use any part of the spectrometer, as can be seen in figure 3.1.

3.2 Setup of the experiment at COMPASS

The setup to measure the scattering of muons on protons is given in figure 3.2. The tracks of the muon before and after the scattering process are measured by two silicon tracking stations each (SI01, SI02 and SI03, SI04, respectively). The scattering process itself takes place in a time projection chamber. The TPC contains hydrogen with a pressure of mostly 8 bar and for a small period 4 bar. The TPC is an active target which means that it is not only a target but also a detector, which measures the energy and the projection to the xy-plane of hits created by ionising particles.

The coordinate system of the setup is given with x being the horizontal coordinate, going to larger values from Jura to Salève[1], y as the vertical coordinate, going up and z following the beam direction.

[1] Jura and Salève are the mountains on the left and right, respectively, when looking in the direction of the beam axis in the COMPASS experiment.

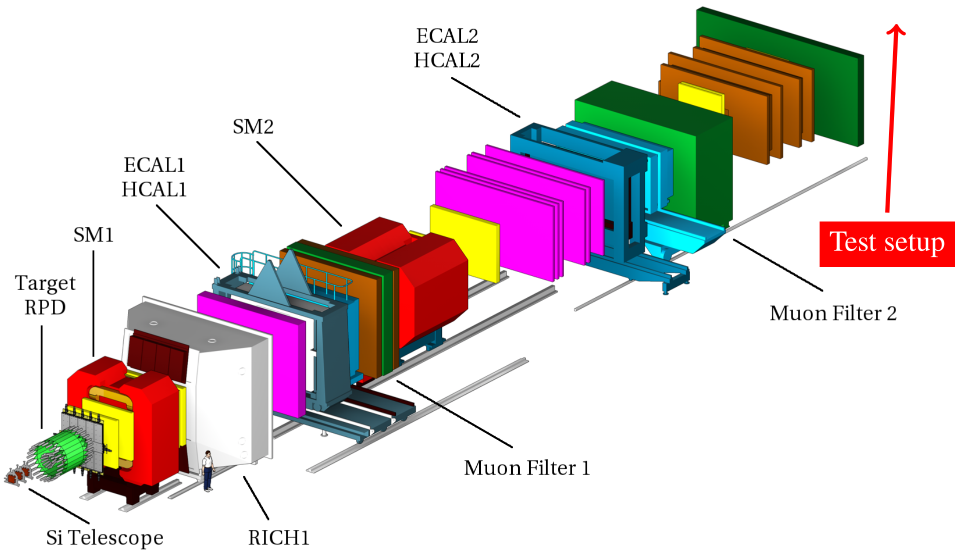

Figure 3.1: An overview of the COMPASS experiment. The beam is coming from the bottom left. The test setup is located at the end of the spectrometer ([18], modified).

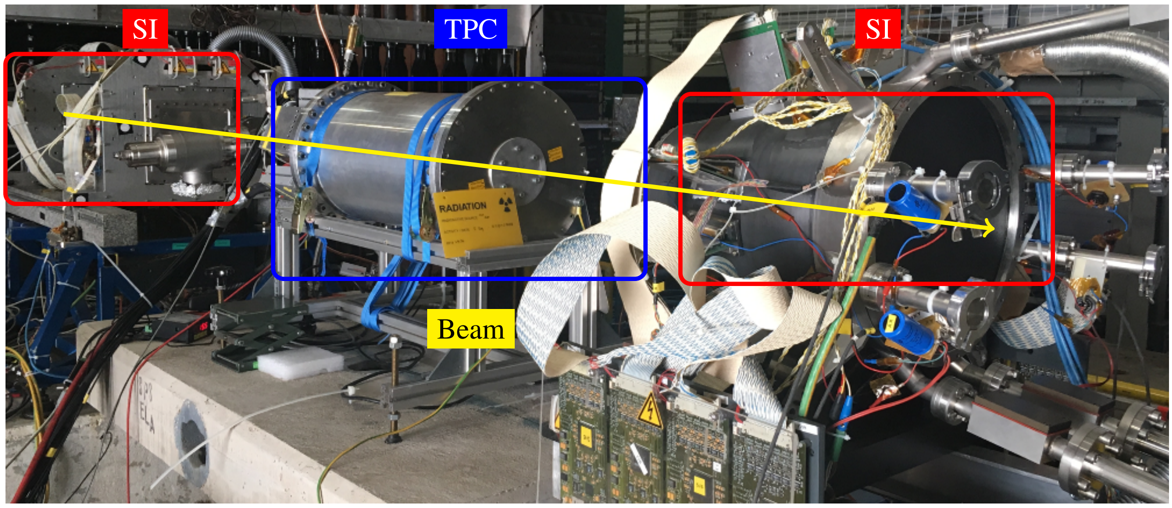

Figure 3.2: A picture of the setup of the proton radius test measurement. From left to right are the following detectors: SI01, SI02, TPC, SI03, SI04. The photograph was taken by Christian Dreisbach.

3.3 Silicon tracking stations

The incoming and outgoing muon beam is measured with four silicon tracking stations. Each station consists of two double-sided silicon-strip detectors (UV and XY). In this experiment, two orthogonal layers of strip detectors are mounted behind each other, functioning as the first readout plane (XY). Roughly 1 cm apart, another readout plane (UV) is placed. Both readout planes have a relative rotation of ±2.5° with respect to the xy-coordinate system. Therefore, the strips in U and X mainly provide information about the x-position, likewise the strips in V and Y mainly provide information about the y-position.

The expected spatial detector resolution σ_{SI} can be approximated by the pitch p, which is the distance of two neighbouring stripes:

$$\sigma_{\mathrm{SI}} = \frac{p}{\sqrt{12}} \quad . \tag{3.1}$$

The resulting resolution is 15.8 µm for the U- and X-planes and 14.9 µm for the V- and Y-planes. The silicon tracking stations are not cooled in this experiment.

3.3.1 Working principle

The silicon-strip detectors are semiconductors. A detailed description of their working principle can be found in [19].

By doting the material and applying a high voltage, a depletion zone is created. When an ionising particle traverses the depletion zone, electron-hole pairs will be freed and induce a measured voltage on the readout pad. For silicon-strip detectors, the voltage is read out at both sides of the strip. From the relative signal strength, the position along the axis can be determined.

3.3.2 Trigger

The information of this section is based on [20]. The trigger setup consists of three BC408 plastic scintillator modules [21]. In front of the first silicon tracking station is one monolithic (70 mm × 50 mm, BT1A) and one segmented (68 mm × 48 mm, BT1B) scintillator. Behind the last silicon tracking station is one monolithic scintillator (BT2A). The schematic view of the scintillators is pictured in figure 3.3. The active area of the trigger system has roughly the same size as the silicon-tracker stations. A schematic of the trigger logic is depicted in figure 3.4. A discriminator sets a threshold for the scintillator signals. Then a coincidence between BT1A and BT2A and any of the seven channels of the segmented scintillator BT1B is required. The trigger signal of the TPC works as a veto for a time of 1 µs and is added directly to the trigger sum after a delay of 500 ns. The resulting trigger rate is larger than the maximal processable rate of the data acquisition (25 kHz). In order to reduce the trigger rate, a prescaler is used, which means that only a percentage of the triggers are used. For example a prescaler of 2 means that only one of two trigger signals are used as a trigger. Additionally to these trigger signals, a random trigger is included.

The time of the readout is saved for the combination with the TPC data.

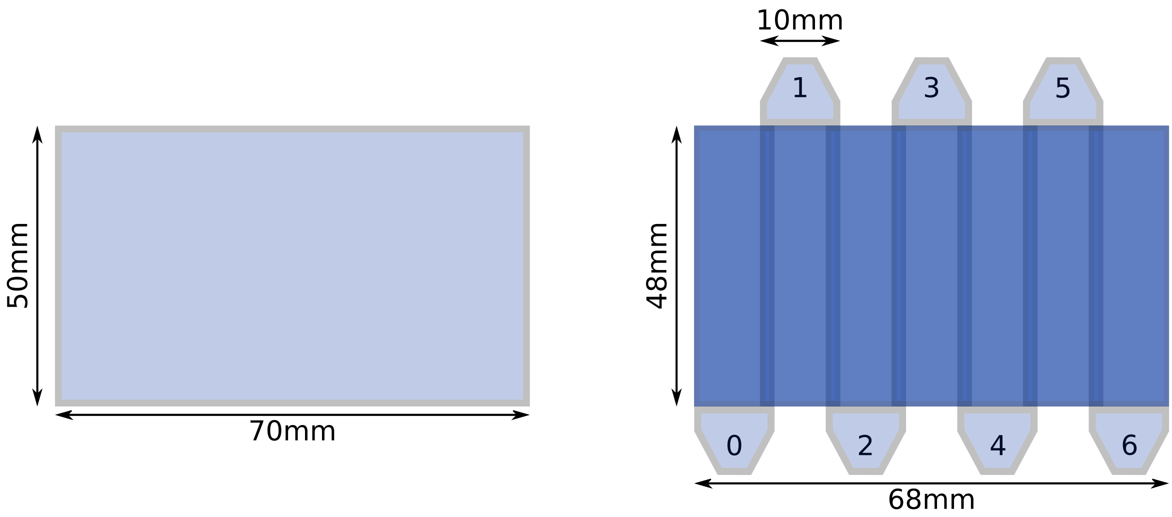

Figure 3.3: A sketch of the monolithic (left) and segmented (right) scintillator that is used to trigger the readout of the silicon-tracker stations [20].

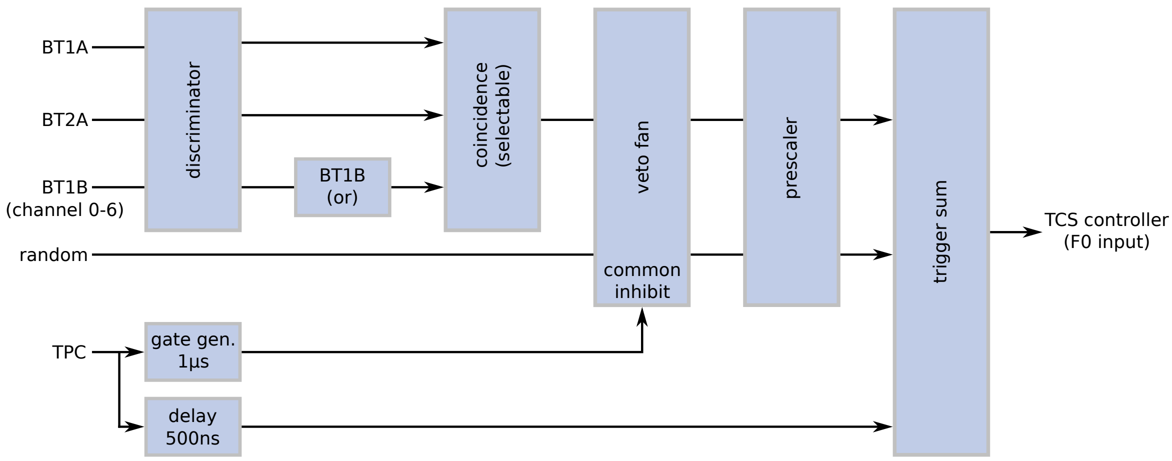

Figure 3.4: The trigger scheme for the silicon tracker readout [20]. The energy signals of all three scintillators are discriminated and a coincidence between both monolithic and any channel of the segmented scintillator is required. In order to reduce the trigger rate, a prescaler is used. A prescaler of 2 means that only one of two trigger signals is used as a trigger. A trigger of the TPC vetoes the normal trigger signal and is added after a delay of 500 ns.

3.4 Time projection chamber

The TPC is a gaseous detector, where an electrical field is applied between an anode and a cathode. If a particle crosses the volume of the TPC, it ionises the gas, hydrogen in this case. The electrons then drift to the anode and the ions to the cathode. The signal induced by the electrons is read out at the anode which is segmented into 66 pads, giving additional information about the xy-position of the signal. The anode signal is read out using SIS3316 14bit FADCs with an input voltage of −2.5 to 2.5 V [22]. The TPC is operated without amplification and low-noise read out. In order to suppress the signal coming from slow ions, a Frisch grid is built 3 mm in front of the anode. The working principle of a TPC is illustrated in figure 3.5 and technical sketch of this TPC is given in figure 3.6. The energy resolution of the pads of the TPC is measured by generating a certain input voltage on the amplifier channels (pad). The resulting standard deviation of the energy for roughly 10k events is between 22 to 36 keV depending on the beam intensity [22]. ^{241}Am is placed at the cathode opposite to pad 7 of the anode for calibration purposes, which is an α-source with an energy of 5.486 MeV. This energy is much larger than the expected signal from recoil protons and is used for the energy calibration, which is described in section 4.2.3.

A high voltage of 18 kV is applied on the cathode and 1 kV on the grid for the 8 bar setting [22]. For the 4 bar setting, both voltages are scaled down to 9 kV and 0.5 kV respectively. The drift velocity and transversal diffusion are simulated by Jonathan Ottnad [23] using GARFIELD++ [24][25] and Magboltz [26] and given in table 3.1. Due to the larger pad size (along φ: 8.64 to 39.27 mm, along r: 11 to 22 mm), effects from diffusion, which are below 0.7 mm, are neglected.

p / bar	Region	$\lvert\vec{E}\rvert/\left(\mathrm{kV\,cm^{-1}}\right)$	$v_{\mathrm{Drift}}/\left(\mathrm{mm\,\mu s^{-1}}\right)$	$D_{\mathrm{trans}}/(\mathrm{\mu m\,cm^{-1/2}})$	$\sigma_{\mathrm{trans}}/\mathrm{\mu m}$
8	Anode-Grid	3.333	7.948	93.1	51
8	Grid-Cathode	0.773	3.702	112.3	527
4	Anode-Grid	1.667	7.856	130.7	613
4	Grid-Cathode	0.386	3.715	160.0	88

Table 3.1: The electric field $\lvert\vec{E}\rvert$ and corresponding drift velocity v_{Drift} for the region between anode and grid as well as between grid and cathode for both settings of the pressure p. The transversal diffusion coefficient D_{trans} and the resulting standard deviation on the transversal coordinate σ_{trans} is given.

When one pad has an energy larger than a threshold energy, all pads are read out. Two thresholds are used at different times in the experiment: 200 and 300 keV. The threshold is enlarged by a factor of 150 for the pads around pad 7 where the α-source is located, so that the readout during the measurement is not triggered by this source. The time of the readout is saved for the combination with the silicon data.

3.5 Time stamp

The detector systems are triggered independently, which leads to two different data sets. In order to combine these data sets, both detectors store a time signal. The TPC stores a **TR**igger **LO**gic (TRLO) time stamp, generated with a frequency of 100 MHz, leading to a time resolution of 10 ns [20]. The silicon-tracking detectors store an event time given by the COMPASS DAQ. These time signals need to be synchronized, which is done with a 1.5 Hz signal. This signal is saved in both data sets. With

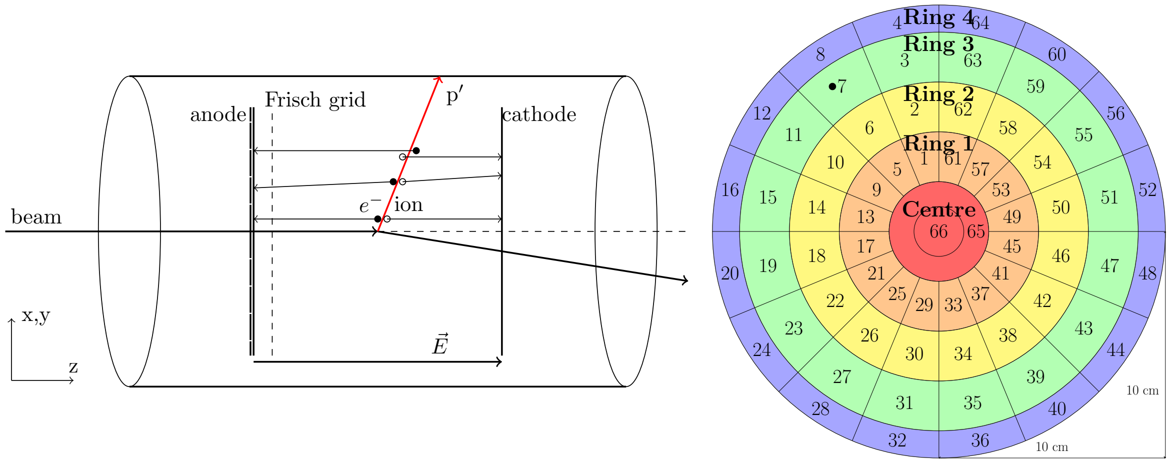

Figure 3.5: The figure on the left shows the working principle of a TPC. Charged particles ionise the gas. Electrons drift to the anode and ions to the cathode due to the applied electrical field. The electrons between the anode and the Frisch grid induce a signal on the readout pads. The pad structure used in the experiment is shown on the right, based on [22]. On the cathode opposite to pad 7, a ^{241}Am α-source is placed for calibration purposes. The anode readout is located in the xy-plane with an arbitrary rotation.

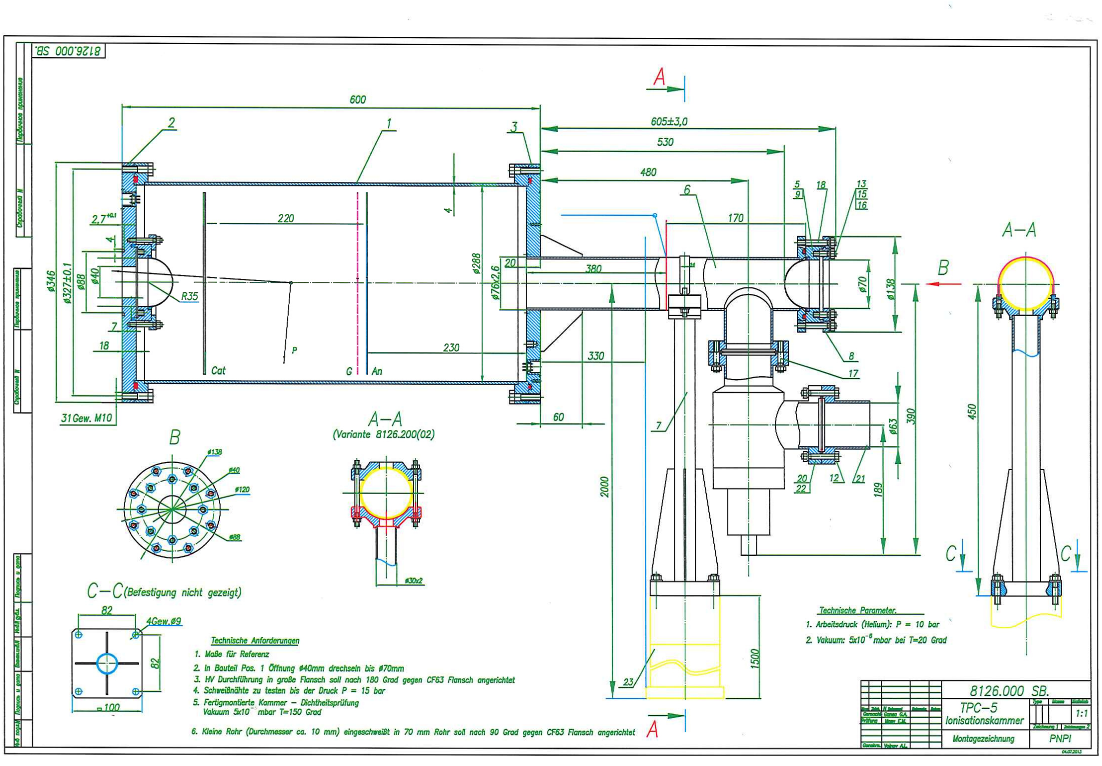

Figure 3.6: A technical sketch of the TPC. The beam comes from the right hand side [22]. The anode is built up of 20 µm copper inside a radius of 22 mm. Outside of this area is 1.5 mm G-10. The cathode is built up of 20 µm aluminium inside a circle of equal size and 1 mm steel. The beam windows consist of 0.5 mm beryllium [27].

one spill taking 4.8 s, this results in 7-8 signals per spill. The TRLO time stamp for the silicon data is determined for every spill with a linear regression of both time signals given by the synchronization signals [20].

3.6 Beam parameters

At the primary target of the COMPASS experiment, a muon or pion beam with a momentum of 190 GeV is produced. The pions can decay into muons. As the setup of COMPASS includes a hadron absorber after the COMPASS target, the beam reaching the end of the spectrometer, which is the beginning of the test setup, should consist only of muons. The beam momentum distribution of the muons at the position of the test experiment could not be measured but is simulated to follow a Gaussian distribution with a mean of (186.8 ± 0.1) GeV and a standard deviation of (6.262 ± 0.044) GeV [28]. The xy-distribution was simulated to have the standard deviations $\sigma_x = 81$ mm and $\sigma_y = 84$ mm. The muons originating from a pion beam have a momentum distribution with a long tail to smaller momenta with a mean value of 172.7 GeV and a standard deviation of 20.14 GeV. The xy-distribution has the standard deviations of $\sigma_x = 92.83$ mm and $\sigma_y = 89.59$ mm [29]. The beam profile can be reconstructed from the measurement of SI01 and SI02 and is shown in figure 3.7 for a muon run with 4 bar. The beam profile in x shows a rising edge, which means that the beam is not centred on the silicon stations. The larger amount of events at an x-position between −3 to −2 cm probably comes from scattering on the entrance pipe, which leads to a higher acceptance of the scattered events at the downstream silicon stations. The beam profile in y shows a slight decrease.

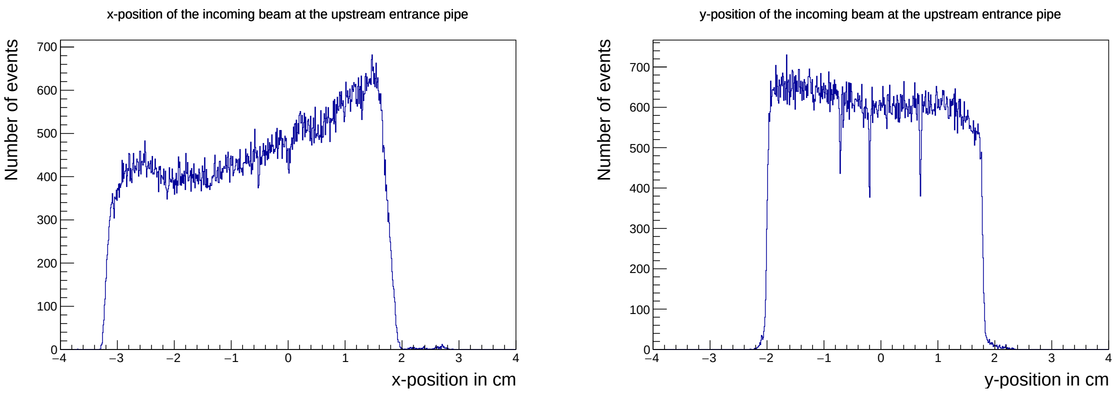

Figure 3.7: The beam position at the upstream entrance pipe is measured with SI01 and SI02. The beam profile in x (left) shows a slope and the beam profile in y (right) is roughly constant. There are much less at x-positions between 2 to 3 cm, which are caused by a disabled APV chip [30]. The beam profiles shown here are taken from run 282500.

The transversal component of the beam direction can be measured with the first silicon stations as well, see figure 3.8. The beam direction in x shows an x-dependence, which will come from the divergence due to a beam-energy spread at the position of the horizontal dipole magnets of the COMPASS spectrometer. The beam direction in y shows a dependence on the y-position as well, which will originate from the SPS beam-energy spread at the position of the bending magnet, which bends the beam from the underground M2 beam line to the overground experimental hall.

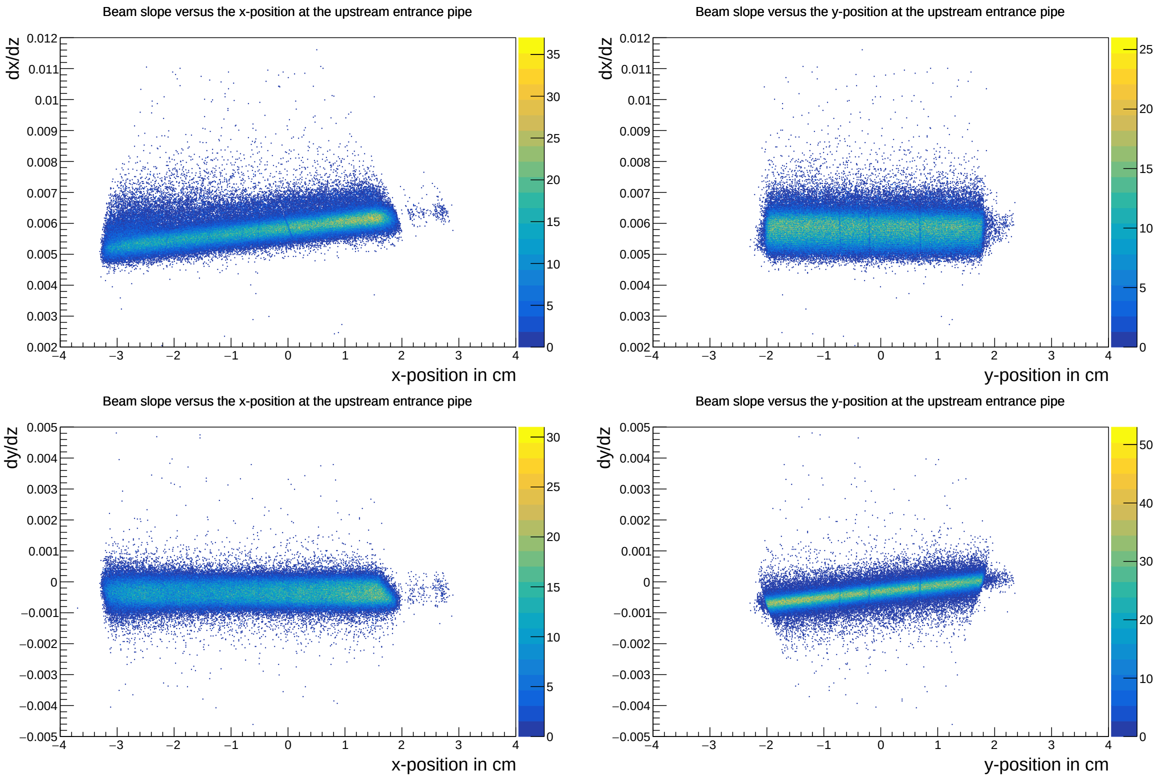

Figure 3.8: The transversal beam direction is measured by SI01 and SI02. The slope dx/dz (top) and dy/dz (bottom) is drawn versus the x- (left) and y-position (right). The number of events is shown with the colour scheme. It is visible that the beam direction in x has a dependence on the x-position and the beam direction in y has a dependence on the y-position. The transversal beam directions shown here are taken from run 282500 with a muon beam at a pressure of 4 bar.

3.7 Expected multiple scattering

The uncertainty of the measurement greatly depends on multiple scattering. This effect can be calculated with the following equation [19]:

$$\Delta\theta_{\mathrm{MS}} = \frac{13.6\,\mathrm{MeV}}{p\beta} z \sqrt{\frac{x}{X_0}} \left(1 + 0.0038 \ln\left(\frac{x}{X_0}\right)\right) \tag{3.2}$$

with the length x, the radiation length X_0 and the charge $z = 1$, normalized velocity $\beta = 1$ and momentum p =186.8 MeV of the incident particle. For several materials in the setup, the factor of the length over the radiation length is summed up and the standard deviation of the angle is calculated. The results can be seen in table 3.2. In order to calculate the expected standard deviation on the scattering angle in in two dimension, one has to multiply the result by $\sqrt{2}$. This results in an expectation of 18.189 µrad for a pressure of 8 bar and a momentum of 186.8 GeV. For a pressure of 8 bar and a momentum of 172.7 GeV this results in 19.674 µrad.

Structure	Material	x / cm	X_0 / cm	x/X_0	$\Delta\theta_{\mathrm{MS}}$/ µrad
SI station (1 of 4)	Silicon	0.06	9.370	0.006403	5.7140
Beam window (1 of 2)	Beryllium	0.05	35.28	0.001417	2.6723
Anode	Copper	0.002	1.436	0.001393	2.6494
Cathode	Aluminium	0.002	8.897	0.000225	1.0572
Conical cryostat window	Mylar	0.02	28.54	0.000701	1.8744
Gas 8 bar	Hydrogen	120	94,100	0.001275	2.5338
Gas 4 bar	Hydrogen	120	188,200	0.000638	1.7876
Sum (8 bar)	-	-	-	0.032040	12.8615
Sum (4 bar)	-	-	-	0.031403	12.732

Table 3.2: The table shows the expected influence of all structures on the multiple scattering. The radiation lengths of all materials are listed in [31]. The materials of the TPC are given in [27]. The factor of length over radiation length is summed up and then the 1-dimensional standard deviation of the scattering angle is calculated for a momentum of 186.8 GeV.

3.8 Expected number of events

It is important to know the number of elastic scattering events that we expect. The number of reactions is given by the integrated luminosity times the cross section σ:

$$N_{\text{reactions}} = \sigma \cdot \int \mathscr{L} dt \quad . \tag{3.3}$$

The integrated luminosity is given by the number of beam particles and the number of protons in the target per area. Using the ideal gas equation, one can calculate the proton density in the target with the pressure p, the Boltzmann constant k_B and the temperature T:

$$\int \mathscr{L} dt = \left(N_{\text{beam, scaled}}\right) \cdot \frac{N_{\text{target}}}{A} = \left(N_{\text{beam}} \cdot f_{\text{Cut}}\right) \cdot \frac{2p}{k_B T} \cdot l_{\text{TPC}} \tag{3.4}$$

with the factor of two originating from two protons per hydrogen molecule and N_{target} is the number of protons in the active volume. The average temperature was 23 °C. The active length of the TPC l_{TPC} is 22.3 cm. The number of beam particles N_{beam} is given by the beam trigger used for the silicon readout. $N_{\text{beam, scaled}}$ is the total number and f_{Cut} is the percentage of incoming beam particles that are accepted by the radial cuts, which are applied on the data, see section 4.1.2. As the beam position was varied over the measurement, especially at the beginning, this factor is calculated for every run using the first chunk and varies between 30 to 47 %. This leads to a integrated luminosity per accepted beam particle of $8.72630 \times 10^{-6}\,\text{mb}^{-1}$ at a pressure of 8 bar and $4.36315 \times 10^{-6}\,\text{mb}^{-1}$ at a pressure of 4 bar. For example, run 282500 lasted 72 minutes with a pressure of 4 bar and collected 311,718 events with a scaling factor of 0.459, this leads to an integrated luminosity of $0.625\,\text{mb}^{-1}$.

The cross section is given by the Rosenbluth cross-section, see section 2.1, integrated over the measured Q^2-range. The lower integration border of the squared momentum transfer is given by the beam momentum and the minimal scattering angle θ of 0.2 mrad, see section 4.1.2. The upper integration border is given by the trigger of the TPC, which requires that a certain threshold energy has to be deposited on a single pad. By looking at a stopping power table [32], one can determine the maximal energy of a recoil proton which still creates a TPC signal. For simplification, the interaction process is expected to occur in the centre of the readout. This leads to the cross-sections given in table 3.3.

Pressure / bar	threshold / keV	$Q^2_{\mathrm{min}}/\mathrm{GeV}^2$	$Q^2_{\mathrm{max}}/\mathrm{GeV}^2$	σ / mb	$\mathscr{L}_{\mathrm{int}}/\mathrm{mb}^{-1}$	N_{exp}
8	200	0.001396	0.014638	0.166636	5120	850
8	300	0.001396	0.008445	0.154102	1150	180
4	200	0.001396	0.006005	0.141889	820	120
8	200	0.001193	0.014638	0.198214	10750	2130

Table 3.3: The cross section, integrated luminosity and expected number of events are given for the settings of the measurement. For a beam momentum of 186.8 GeV, corresponding to a muon beam, and a scattering angle of 0.2 mrad, the minimal Q^2 is 1.396×10^{-3} GeV^2. For a beam momentum of 172.7 GeV, corresponding to muons from a hadron beam, the minimal Q^2 is 1.193×10^{-3} GeV^2.

With 1.95×10^9 measured events in the silicon trigger that pass the radial cuts with 8 bar hydrogen and 1.88×10^8 events in 4 bar hydrogen, there are 3160 events expected with 8 bar and 120 with 4 bar pressure.

CHAPTER 4

Analysis of the 2018 test measurement

This chapter deals with the analysis of the 2018 test measurement. First, the data from the silicon trackers and the TPC are looked at separately. The focus of the silicon data is to obtain and improve the z-vertex resolution of the detector, from which one can calculate the angular and energy resolution. The data is also used for the data selection, e.g. the position of the active readout part of the TPC and the radius of the pipes attached to the TPC vessel. The data of the TPC is used to reconstruct the energy and the direction of the recoil proton.

The TPC has a different data acquisition, as it was built for an experiment at MAMI. Due to time constraints, it was decided to combine the data sets by using time stamps. After the combination different cuts are applied to reduce noise. Correlations between parameters measured in the TPC and in the tracking systems, like the energy and the direction of the recoil proton, are analysed.

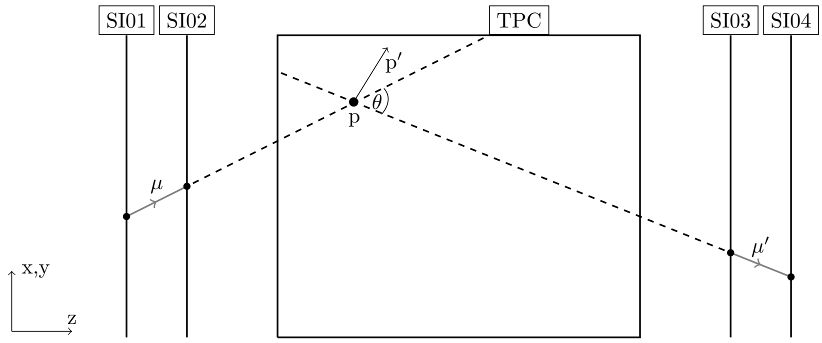

Figure 4.1: This is a sketch of the experimental setup. The direction of the incoming muon is measured with SI01 and SI02 while the direction of the scattered muon is measured in SI03 and SI04. The intersection of both tracks defines the scattering vertex point. The energy and the direction in the xy-plane of the recoil proton is measured in the TPC. The sketch is not to scale.

4.1 Silicon data

4.1.1 Analysis procedure

The reconstruction of tracks from the hits in the silicon trackers is illustrated in figure 4.1. Starting from the hits on all 8 planes of SI01 and SI02 the direction of the incoming muon is reconstructed, as well as the direction of the scattered muon by using the information of SI03 and SI04. The intersection of the incoming and scattered muon track defines the scattering vertex point. From this, the scattering angle θ and the polar angle φ are extracted. The incoming beam does not move parallel with respect to the z-axis. This is corrected by a rotation of the beam particle into the z-axis. All other particles are rotated equally. Using the scattering angle θ and the assumption of a recoil proton, one can calculate the kinetic energy of the recoil proton, see equation (B.3) in the appendix B.2.

4.1.2 Applied cuts

The z-resolution of the reconstructed vertex depends on the scattering angle θ. For small θ, the direction of the incoming and scattered muon track are very similar. Due to multiple scattering and the intrinsic resolution of the silicon trackers, an uncertainty on the scattering angle is added, which has a higher influence on the z-vertex for smaller scattering angles. The z-vertex resolution is investigated in section 4.1.5. In order to achieve a reasonable z-resolution, only events with $\theta \geq 0.2\,\mathrm{mrad}$ are used.

To avoid multiple scattering on massive material inside the TPC, in this case the downstream end cap and the holding structure of the cathode, a radial cut is applied at these positions. The end cap can be seen in figure 3.6. The downstream end cap can be estimated as a circle around the position ($x_0 = 0.23\,\mathrm{cm}$, $y_0 = -0.01\,\mathrm{cm}$) at $z = 60\,\mathrm{cm}$, see figure 4.2. The radius for the cut is chosen to be 1.99 cm, as figure 4.2 shows. The cathode has a holding structure which is shifted with respect to the beam windows. This is estimated with a circle around the position ($x_0 = 0.31\,\mathrm{cm}$, $y_0 = -0.66\,\mathrm{cm}$) at $z = 46.2\,\mathrm{cm}$. A radius of 1.9 cm is chosen in order to reject all events originating from scattering on this holding structure. The distributions of the incoming muon beam are given in figures C.1, C.2 in section C.1. Events where the extrapolation of the initial muon or the scattered muon was outside of the circle of the end cap or the circle of the cathode are rejected. The upstream entrance pipe has a diameter of 7 cm and should not be visible in our data. Nevertheless, the central position of the beam at the upstream entrance window is estimated to be around ($\mathrm{x}_0 = -0.46\,\mathrm{cm}$, $\mathrm{y}_0 = 0.00\,\mathrm{cm}$) which is used later for the transformation of the silicon coordinate system into the TPC system.

4.1.3 Z-positions of the setup

By looking at the distribution of the z-vertices with $\theta \geq 3\,\mathrm{mrad}$, the structures in the experimental setup are clearly visible, see figure 4.3. The stricter cut on the scattering angle is used to have the best possible resolution of the z-vertex with a reasonable amount of events. The z-vertex distribution is fitted with different Gaussian functions to account for all structures. The gas volume is parametrised as a rectangular distribution convoluted with a Gaussian function. The silicon stations are parametrised with three Gaussian functions of different widths. The resulting positions are given in table 4.1.

As the peak between 10 to 20 cm has no corresponding analogue in the technical sketch of the TPC, see figure 3.6, this has to be investigated. By looking at the xy-positions of the incoming beam track extrapolated to the anode position, one can see cable-like structures, see figure 4.4. Here one

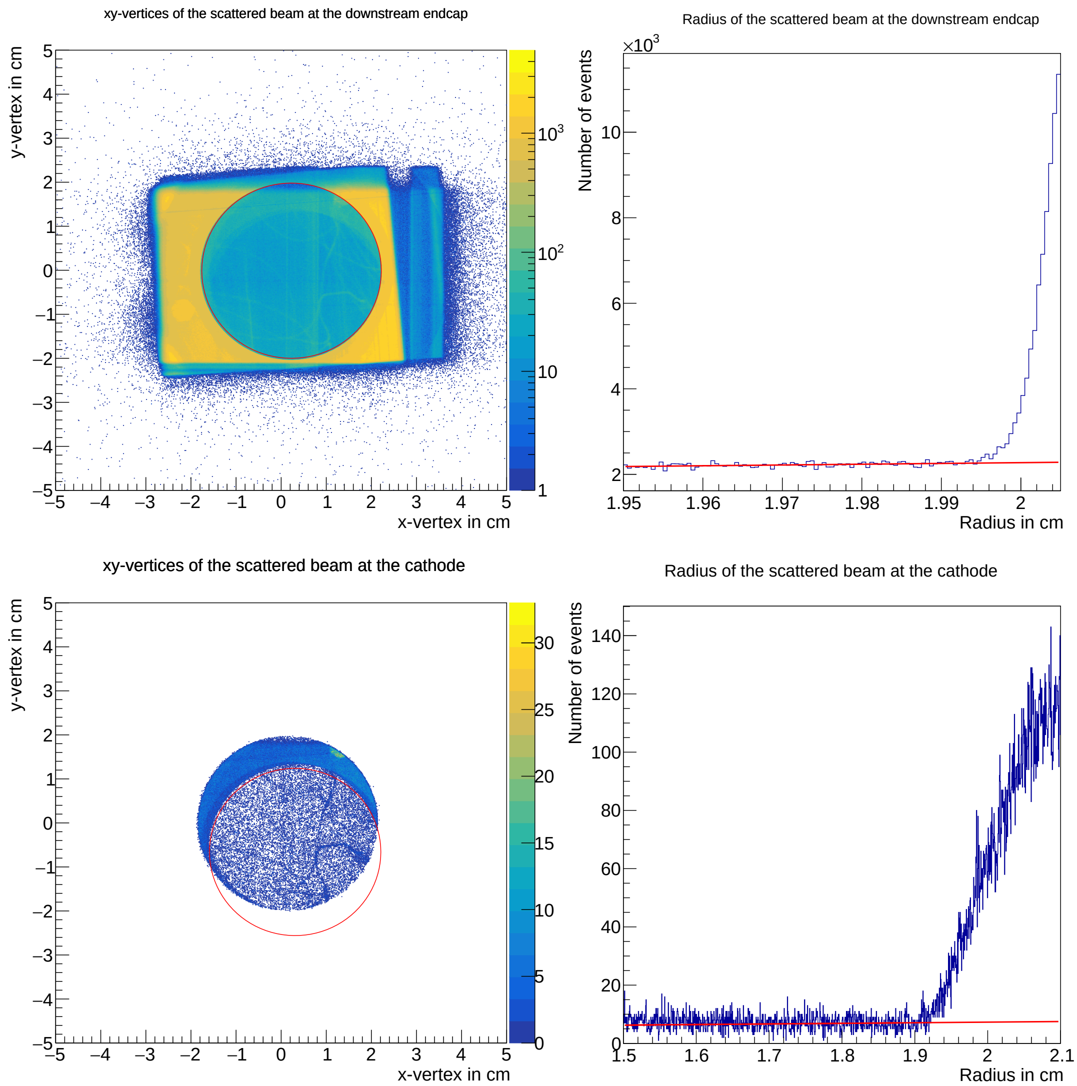

Figure 4.2: The figures show the xy-positions of the scattered (left) beam extrapolated to the position of the downstream exit window (top) and to the cathode (bottom). The extrapolations to the cathode have an additional cut that the z-vertex position is between 42 to 50 cm, so that the holding structure is better visible. The number of events is shown with the colour scheme and the red circle shows the applied cut. On the right hand side, the number of events are plotted against the radius. A radius of 1.99 cm is chosen for the cut on the end cap and 1.9 cm for the cut at the cathode position.

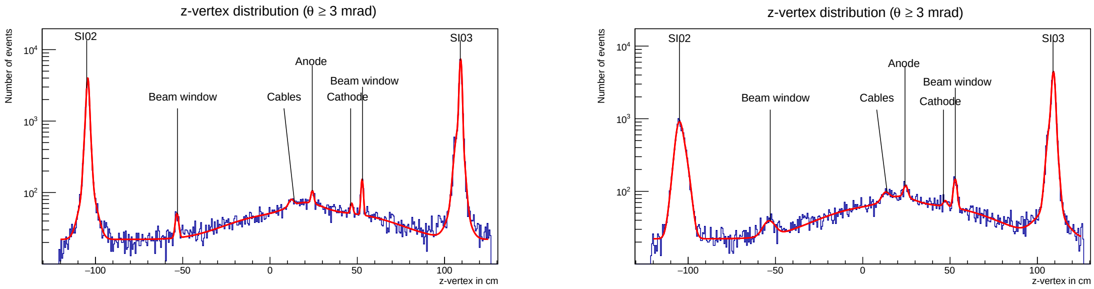

Figure 4.3: The figure shows the distribution of the z-vertex with $\theta \geq 3$ mrad for the run-by-run alignment (left, χ^2/dof= 900.16/395), and the preliminary alignment (right, χ^2/dof= 748.31/395). The fits are used in order to fix the positions of the peaks. The alignment is described in section 4.1.4.

can search for all bins which have at least 25 entries and assign them to cables. By looking at the distribution of the z-vertex without the cables, the peak between 10 to 20 cm disappears, see figure 4.5.

Detector	z-position / cm	
	Run-by-run alignment	Preliminary alignment
SI02	-104.5 ± 0.1	-105.2 ± 0.1
SI02	-104.4 ± 0.1	-104.3 ± 0.2
SI02	-104.3 ± 0.1	-104.2 ± 0.1
Entrance window	-53.3 ± 0.2	-53.7 ± 0.2
Cables	12.2 ± 0.8	13.0 ± 0.3
Cables	20.1 ± 0.9	21.0 ± 1.3
Anode	24.3 ± 0.2	24.6 ± 0.3
Gas (smeared box)	24.8 ± 0.6	24.9 ± 0.9
Cathode	46.8 ± 0.3	47.3 ± 0.2
Exit window	53.0 ± 1.1	53.0 ± 0.1
SI03	107.7 ± 0.2	107.4 ± 0.1
SI03	108.3 ± 0.1	108.4 ± 0.1
SI03	109.2 ± 0.1	109.3 ± 0.1
Tail of SI04 (used for $\theta < 1.31$ mrad)	125.5 ± 0.5	not used

Table 4.1: The z-positions of important parts of the experiment with the corresponding fit error for the preliminary and run-by-run alignment. The alignment procedure is explained in section 4.1.4.

4.1.4 Alignment and residuals

Due to changes in the temperature, the positions of the silicon stations shift slightly over time, resulting in a deterioration of the resolution. Therefore, the positions of the stations have to be aligned for each run ("run-by-run alignment"). Alignment means that the position and orientation of the detectors is implemented correctly in the reconstruction program. A preliminary alignment was done using tracks from run 281835 during the measurement [33].

The preliminary alignment is taken as a starting point. For the preliminary alignment, the spatial resolution of the silicon trackers was enlarged up to a factor of 100 to allow for larger shifts to take

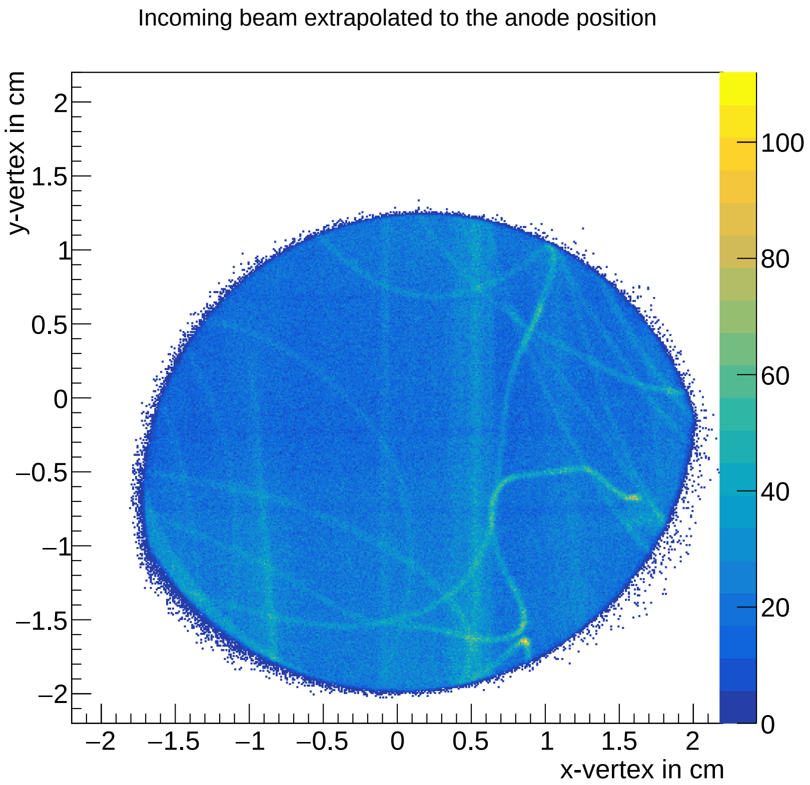

Figure 4.4: The xy-distribution of the beam track extrapolated to the anode position with $\theta > 0.2$ mrad. The number of events is shown with the colour scheme. One can see cable-like structures. The events on bins, which have at least 25 entries in this histogram, are treated as events which scattered on the cables.

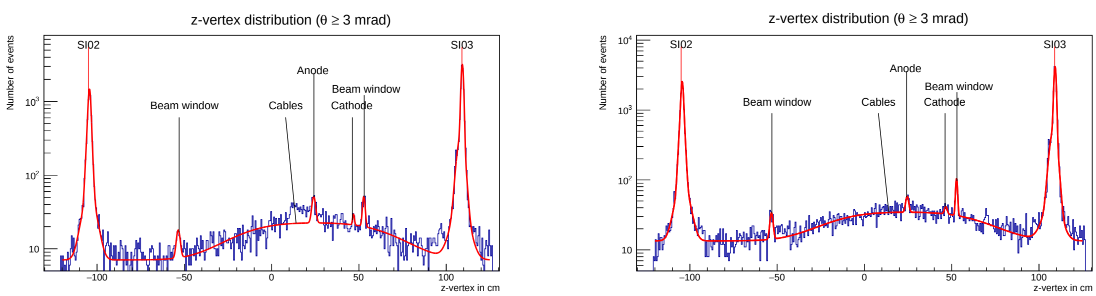

Figure 4.5: The distribution of the z-vertex with $\theta \geq 3$ mrad, run-by-run alignment (see section 4.1.4), and with only (left, χ^2/dof= 725.361/401) or without the cables (right, χ^2/dof=788.67/401) seen in the xy-vertex plot. The corresponding cable peak is taken out of the fit model on both figures and is not seen on the right. Still, the reduced χ^2 is better with the cables than without, as this is dominated mainly by the large number of events at the silicon tracking stations. Therefore, this peak corresponds to cables upstream of the anode.

place. This was not done in this case, as the preliminary alignment should be close enough to the real value.

The alignment is done with the Millepede procedure [34], which is described in the next passage and implemented as part of CORAL[1]. In this case 100k events are reconstructed using the hypothesis of straight tracks with all detector planes. With the reconstructed events, the distance between the reconstructed track position at each plane to the real hit position on this plane is stored, the so called residuals. The residuals should be centred around 0 and for this reason, their absolute values are minimised by shifting the xy-centre of the detector planes and the rotation angle perpendicular to the beam axis. In order to have no overall shift of all detector planes, the pitch and z-positions of all planes are fixed as well as the xy-positions of SI01XY, SI02XY and the angle of SI01XY. This procedure was iterated two times because at this point the positions only change by less than 1 µm.

An ionizing particle induces not only a signal on one strip, but as well on neighbouring strips. This behaviour is described with charge sharing functions. Up to this point only default charge sharing functions are used which is changed now [36]. With these functions, a third iteration of the alignment is done.

In figure 4.6 one can see that there is an overall shift of the x-position of SI04V with time[2]. It is visible that there are daily fluctuations which seemingly correspond to the daily fluctuations of the temperature of the silicon station and the ambient temperature [3]. The origin of the overall shift is not known. The mean value of both the silicon and the ambient temperature is rising slowly over the measurement. From the daily fluctuations, one would expect that the x-shift should go to positive values. The silicon setup is mounted on concrete. Therefore, one possibility might be that the temperature has an effect on the silicon planes as well as on the concrete but with different strength and opposite sign.

For the change of the y-position, one can only see daily fluctuations due to temperature changes with opposite sign but no overall trend. An example is given in the appendix, see figure C.3.

As a quality check of the alignment, one can look at the residual distribution. Therefore, a straight track fit with the updated alignment is performed and the residuals for one detector plane are calculated. They should be centred around 0. The residuals are calculated using the second 100k events of the first chunk, in order to avoid any bias with the data used for the alignment, and the first 100k events of the last chunk. A chunk is a subset of one run, containing up to 1 million events. One can see that the residuals are constant over time, see figure 4.7. It is visible that the residuals taken at the end of the run (blue) vary much more than the ones from the first chunk (red). This originates from a detector movement in the course of each run. One run lasts about 1-2 hours. Nonetheless, this is much better than with the preliminary alignment where jumps of up to 10 µm were measured between different not consecutive runs. In the XY-planes the residuals are not centred at 0, which can be seen in figure C.4 in section C. It is expected that this originates from a wrong determination of the pitch or the angle between the planes as it only affects the XY-plane and not the UV-plane.

[1] **CO**MPASS **R**econstruction **AL**gorithm. This software reconstructs events from the COMPASS experiment. One has to provide information about the detectors, e.g. the position, and the experimental setup, i.e. material for multiple scattering. In our experiment, either one track is reconstructed for SI01, SI02 and another track through SI03, SI04 or one straight track through all stations [35].

[2] One should notice that the coordinate system in the CORAL "detectors.dat" output file is rotated with respect to the lab frame ("detectors.dat" → lab: $x \to z$, $y \to x$, $z \to y$). In the thesis, the coordinate system of the lab frame is used.

[3] The temperature of the silicon stations are measured with PT-100 sensors, which are attached to the U and the X side of the detectors [37].

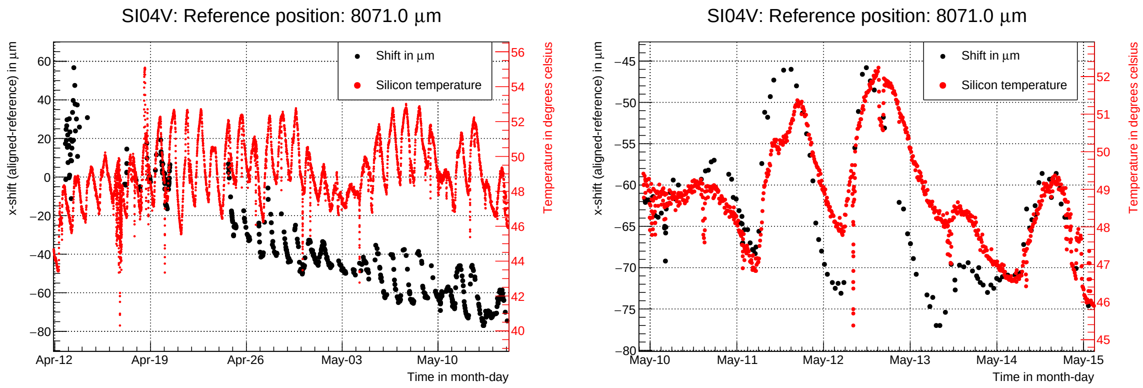

Figure 4.6: The shift in x-position of the SI04V-plane (black) and the temperature measured at the silicon station (red) for the whole measurement (left) and the same for the last week of data taking (right) versus the time. One can see a shift of roughly 100 µm over the whole data taking period. The picture on the right shows that the fluctuations of the shift follow the temperature measured by the silicon stations.

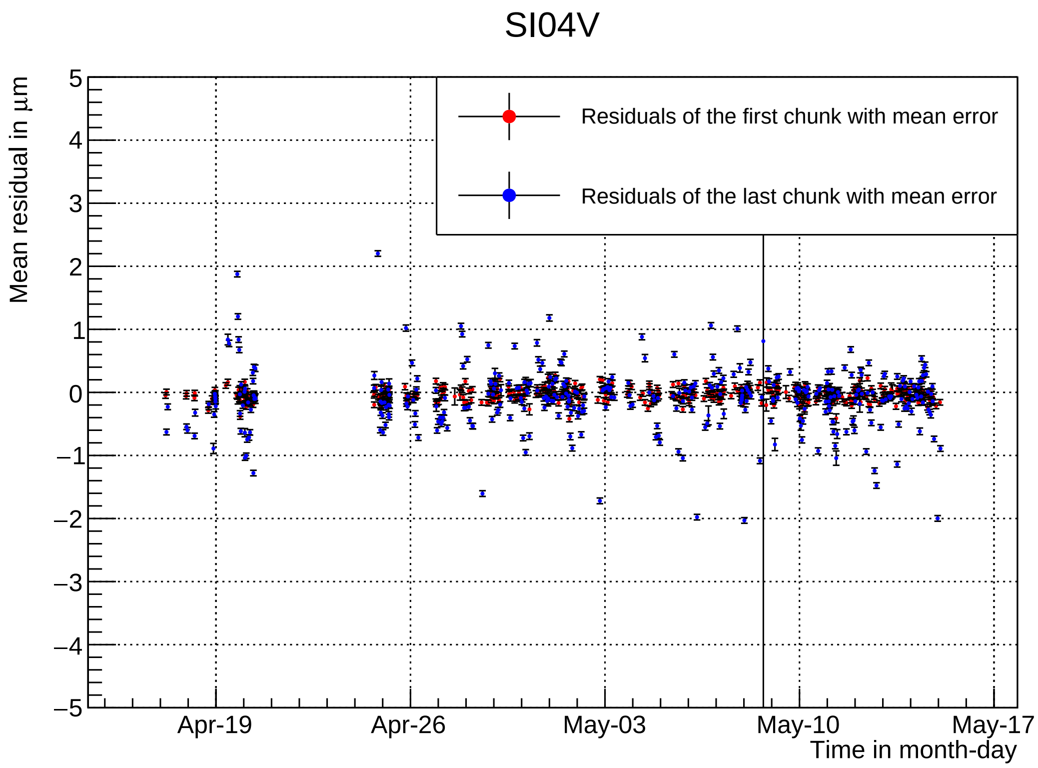

Figure 4.7: The residuals of SI04V measured from the second 100k events of the first chunk (red) and the first 100k events of the last chunk (blue) of each run. The residuals are constant with time. The blue points have larger variations due to a detector movement over time. Only chunks with more than 1,000 events and a reduced χ^2 of less than 10 are plotted.

4.1.5 Resolution of the z-position of the vertex point

The resolution can be measured by determining the width in z of the vertex distribution from a very thin structure inside our active volume. Inside a circle with a radius of 2.2 cm the anode has a thickness of 0.02 mm (Cu). There is the Frisch grid 3 mm apart, and the cathode has a thickness of 0.02 mm (Al) inside the same circle, see figure 3.6. Both could be used for the determination of the resolution, but due to the larger number of events in the anode, the width of this peak is more meaningful and thus used here. The resolution should depend on the z-position of the vertex as one can see in the MC studies in section 5.3. This could not be studied in the real data analysis. The results with a preliminary alignment are compared to the values with the run-by-run alignment.

The same fitting procedure is used to avoid a bias between different fits. The function used in section 4.1.3 is fitted for different $\theta-$bins in order to extract the dependence on the scattering angle. Therefore, the data set is split into several bins with 20k and 60k events for the preliminary and run-by-run alignment, respectively. For smaller θ-values, there are no visible peaks in the spectrum of the preliminary alignment. In case of the run-by-run alignment, the cable and the anode peaks overlap, so that the width cannot be distinguished. The fit results are given in table 4.2. All fits can be found in the appendix, see chapter E.

θ_{min}/mrad	θ_{max}/mrad	σ/cm
Preliminary alignment		
2.580	4.150	3.50 ± 0.34
4.150	7.480	1.39 ± 0.51
7.480	–	1.12 ± 0.22
Run-by-run alignment		
0.500	0.590	8.70 ± 0.12
0.590	0.790	4.66 ± 0.41
0.790	1.310	3.95 ± 0.43
1.310	3.010	1.60 ± 0.07
3.010	–	1.01 ± 0.11

Table 4.2: This table shows the extracted σ-widths of the anode peak in different θ-bins ($\theta_{\text{min}} \leq \theta < \theta_{\text{max}}$) for the preliminary and run-by-run alignment. θ_{max} = " – " means that all events with $\theta_{\text{min}} \leq \theta$ are used.

In figure 4.8, the standard deviation of the anode peak is plotted against the scattering angle. This is used as the uncertainty for the z-position of the vertex point. The plotted θ-value of each bin is given by the average of all θ-values in this bin. The plotted error on the θ-angle corresponds to 1 σ-quantiles, so 68 % of all scattering angles are in this interval. One can see, that the run-by-run alignment improves the resolution a lot. The resulting fit is improved by a factor of roughly 2.3. Also it is possible to extract the σ-width at much smaller θ-angles, where no structures are visible for the preliminary aligned data.

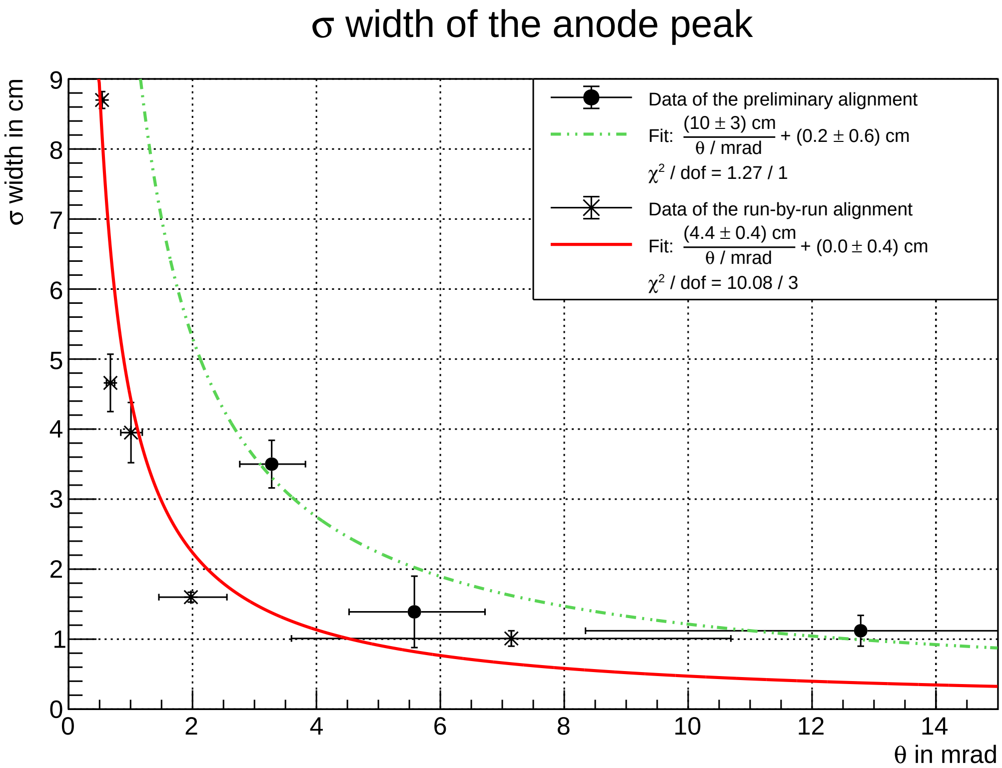

Figure 4.8: The z-vertex resolution with the preliminary (black points, green, dashed line) and the run-by-run alignment (black crosses, red line) is plotted against the scattering angle θ. The positions of the structures are fixed from a fit to all data points with $\theta \geq 3$ mrad, see figure 4.3 and table 4.1. Then the data points are divided into several bins with 60k events for the run-by-run alignment and 20k events for the preliminary alignment. In these bins, the z-vertex distribution is fitted to the data, the results are given in table 4.2. The θ-angle with error plotted here corresponds to the average value and 1σ-quantiles of each bin. For both alignments, a $1/\theta$ curve is fitted, as the resolution should depend on the relative uncertainty on the scattering angle due to multiple scattering.

4.1.6 φ-distribution

The momentum change of the beam in the x- and y-direction due to the scattering process is indicated by the azimuthal φ-angle. The φ-distribution measured by the silicon trackers can be seen in figure 4.9. There are four peaks[4] visible at $\pm\pi, \pm\frac{\pi}{2}, 0$. Most of these events have a z-vertex in the silicon stations. This distribution might come from the geometry of readout strips of the silicon tracking detectors. If there are two hits on one readout plane, it might be indistinguishable which hit corresponds to the track. This leads to a wrong reconstruction. Additionally, the strips are oriented along the x- and y-direction and therefore particles flying in a small angle with respect to these axes will always be reconstructed exactly at the φ-angles seen above. This effect should be limited by the relative rotation of 5° between the UV- and XY-planes.

It is shown in figure C.5 in section C.3 that the φ-distribution is flat for events that are matched with the TPC.

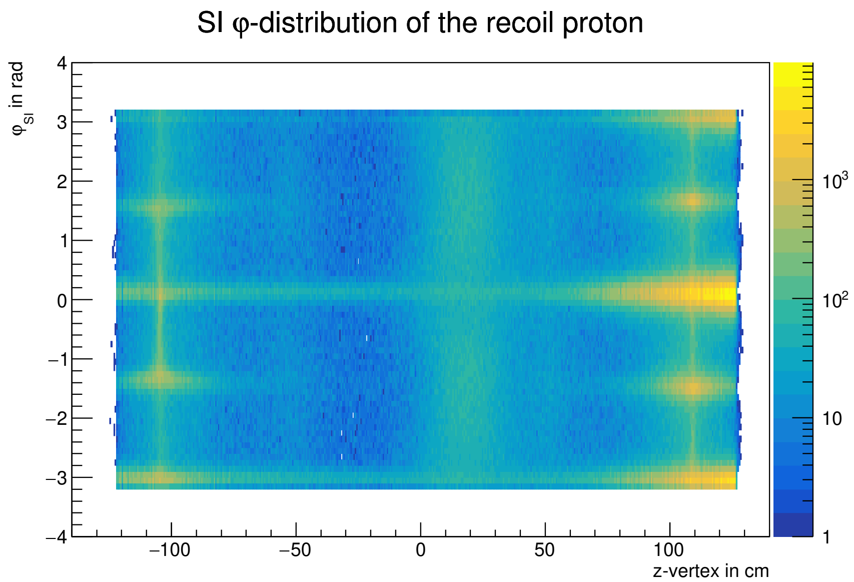

Figure 4.9: The momentum change of the beam in the x- and y-direction due to the scattering process is indicated by the azimuthal φ-angle. The φ-distribution measured by the silicon trackers is plotted here. If the muon has scattered on a proton, this would be the φ-angle of the recoil proton. The number of events is shown with the colour scheme. There are peaks visible at $\varphi = 0, \pm\pi/2, \pm\pi$. Most of these events have a z-vertex near the silicon trackers.

4.2 TPC data

In this section the analysis procedure for the TPC data set is explained. Then the procedure to distinguish a signal from electrical noise and the calibration is presented before coming to the track-fitting algorithm which gives the total energy and the direction of the particle measured in the TPC.

[4] The peaks at $+\pi$ and $-\pi$ are the same due to the periodicity of φ.

4.2.1 Analysis procedure

The first step of the analysis of the data set is done by our colleagues [38][22]. The signal shape is measured over 108 µs, with 2692 channels of 40 ns. This signal is smoothed to improve the signal-to-noise ratio. Then the start and end time of the signal is extracted using the rising and trailing edge. Integrating over the total signal gives the total energy. Signals with a duration outside of 1.8 to 8.0 µs on a single pad are not taken into account for the further analysis.

4.2.2 Background noise

Measuring the background noise is important in order to distinguish a signal from noise. By looking at the pad energies of a run without beam, in this case run 282433, one can get an estimate of the electronic noise. A mean value and standard deviation of electrical noise without any signal is extracted by fitting a Gaussian distribution to the energy spectrum on each pad. If the energy on one pad is larger than the mean pedestal plus three times the standard deviation of the pedestal value, the pad is considered as hit. Otherwise, the pad is considered as not hit and will not be taken into account for the further analysis.

The maximal noise coming from the beam can be estimated. The energy loss of a minimal ionizing particles in 8 bar hydrogen is roughly 3 keV cm^{-1} and the distance between the anode and the cathode is 22.3 cm, resulting in an energy loss of 67 keV per muon. With the average unprescaled beam trigger rate of 420k events per second and a maximal time window of 8 µs, 3.36 muons are expected to create a signal in the TPC which corresponds to a total energy deposition of 225 keV in 8 bar hydrogen. This energy is distributed over the xy-plane, depending on the beam profile. This noise should be already subtracted in the first analysis.

The combined noise per pad is between 22 to 36 keV depending on the beam intensity [22].

4.2.3 Calibration

An α-source is placed at the cathode opposite to pad 7. Its energy of 5.486 MeV is larger than the expected energy deposited by a proton and is used to calibrate the energy signals. Due to absorption inside the α-source, the width of this peak is much larger than the energy resolution of the TPC [22]. In figure 4.10 the energy of pad 7 is drawn against the starting time of the corresponding run. It is visible that the energy decays with time and sometimes jumps. Those jumps can be correlated to re-fillings of the hydrogen gas. Hence, the energy decay probably comes from increasing impurities in the gas which leads to electron attachment to the gas.

Consequently, an energy calibration is necessary for each run. For this calibration only events are taken where pad 7 was above threshold but not the neighbours to reduce the influence of escaping α-events and a recoil proton flying in this direction. A minimum of 25 α-events with an energy between 4 to 6 MeV is needed for a successful calibration. So if the run has not enough measured events, then other runs from the period are taken. A period contains all runs with no longer intervention. This is checked by the difference between the end time of a run and the start time of the consecutive run which should be smaller than one hour. If there are not enough events in a period, the periods before and after are taken into account until enough events are collected. The result of the calibration can be seen in figure 4.11.

For the calibration of events, which do not start at the cathode, the energy loss due to attachment decreases exponentially with the drift length, which is z in our case [39]. As the α-source is positioned

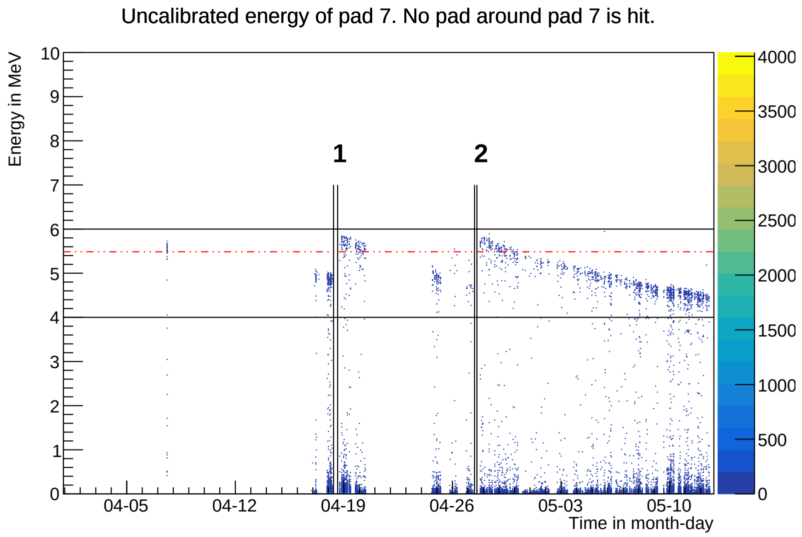

Figure 4.10: The energy of pad 7 is drawn versus the starting time of the corresponding run. Only events are taken into account, where no neighbouring pad of pad 7 was hit. The number of events is shown with the colour scheme. The α-signal decreases due to impurities in the hydrogen gas and jumps back after re-fillings of the gas, which are marked with the vertical lines 1 and 2. Events with an energy between 4 to 6 MeV, indicated by the horizontal lines (black), are considered for the energy calibration. The last horizontal line (red, dashed) shows the energy of the α-source.

at the cathode, the energy loss over the complete drift length is known and one can assume that an electron produced near the anode has no energy loss due to attachment. After combining both data sets, the following calibration $E_{\text{calibrated}} = c(z) \cdot E_{\text{uncalibrated}}$ is used:

$$c(z) = c_{\text{Run}} \left(\frac{c_{\text{Refill}}}{c_{\text{Run}}} \right)^{-(z - z_{\text{Cathode}})/(z_{\text{Cathode}} - z_{\text{Anode}})} \tag{4.1}$$

with c_{Run} being the calibration factor at this run and c_{Refill} the calibration factor at the first run after a re-filling of the TPC, which is indicated in figure 4.10. The calibration is set to c_{Run} for $z \geq z_{\text{Cathode}}$ and c_{Refill} for $z \leq z_{\text{Anode}}$. The uncertainty of the calibration due to the z-vertex resolution of the silicon tracking stations, given by equation (4.2), is added on top of the TPC resolution:

$$\Delta c(z) = -\ln \left(\frac{c_{\text{Refill}}}{c_{\text{Run}}} \right) \frac{\Delta z}{z_{\text{Cathode}} - z_{\text{Anode}}} \cdot c(z) \quad . \tag{4.2}$$

4.2.4 Track reconstruction

Up to this point only information about single pads is described. In order to get the combined information of the TPC, one needs the full track of the particle. The following tracking algorithm is used under the assumption that all tracks start at one of the inner pads (65 or 66) or the inner ring and go outside from there. This is not true for all TPC tracks as there is a broad muon beam. For the events combined with silicon events this is a valid assumption because of the applied radial cuts at the position of the cathode and downstream end cap.

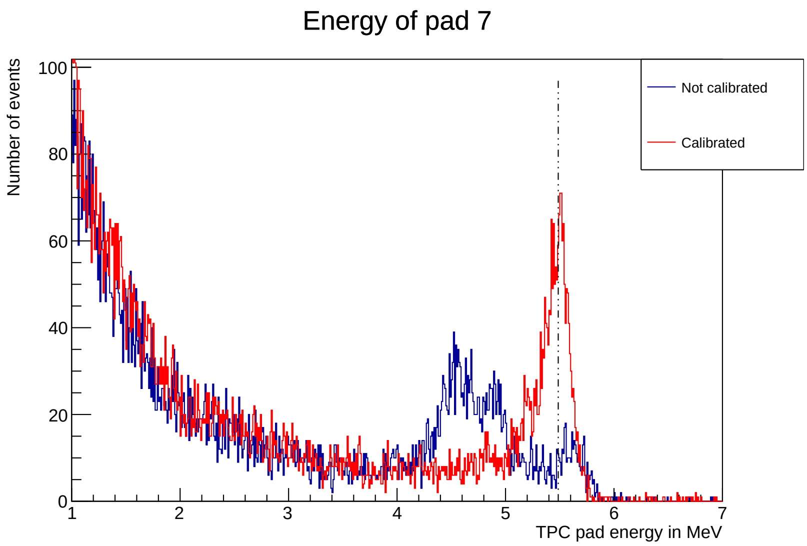

Figure 4.11: The energy of pad 7 before (blue) and after (red) the calibration. Before the calibration there are several small peaks and after the calibration one can see a normal energy spectrum. The energy of the α-source (5.486 MeV) is marked with a dashed vertical line (black).

The tracking algorithm will be explained with the example of the track shown in figure 4.12. The pad with the highest energy (pad 31, $r = 77$ mm, $E = 1.065$ MeV, $\varphi = -1.767$ rad) is the starting point of the algorithm. Due to the higher energy loss of a particle with low energy, as described in the Bethe-Bloch formula, this will be the end point of the track. For each ring up to two neighbours in each direction of the ring are taken into the track if the pads are hit. In this case, no neighbour is hit. Up to two rings above pad 31 are taken into account because many tracks do not stop at the pad with the highest energy but shortly after. In this case, no pad above pad 31 is hit. Then the corresponding pad one ring below pad 31 is checked, which is pad 30 ($r = 55$ mm, $E = 0.978$ MeV, $\varphi = -1.767$ rad). This pad also has no neighbour. The same is done another time. Here pad 29 ($r = 33$ mm, $E = 0.286$ MeV, $\varphi = -1.767$ rad) and pad 33 ($r = 33$ mm, $E = 0.441$ MeV, $\varphi = -1.374$ rad) are hit. The radius of the ring is 33 mm and the centre of gravity φ is calculated by using the pad energies as weight:

$$\varphi = \frac{\varphi_{29} \cdot E_{29} + \varphi_{33} \cdot E_{33}}{E_{29} + E_{33}} = -1.529\,\text{rad} \quad .$$

At last, pad 66 is included in the track. Pad 65 would be included as well if it is hit.

With these pads and their energies, the radius of each ring and the φ-coordinate of the centre of the hit ring is calculated. This procedure results in an array of hit pads for the track and centres of gravity for each ring. The energy of all pads is summed up to the track energy.

After all hit pads of the track are collected, one can get the direction of the track if at least three rings are hit. First, a linear fit in the (x,y)-coordinate-system is made ($m = 2.4 \pm 0.7$, $b = -35 \pm 8$ mm, χ^2/dof= 67.6/1). If the fit crosses one of the central pads, which is also hit, then this pad with the φ-coordinate extracted from the fit is used for the second fit.

In the second fit, all central coordinates of each hit ring are used to make a linear fit. This is done in

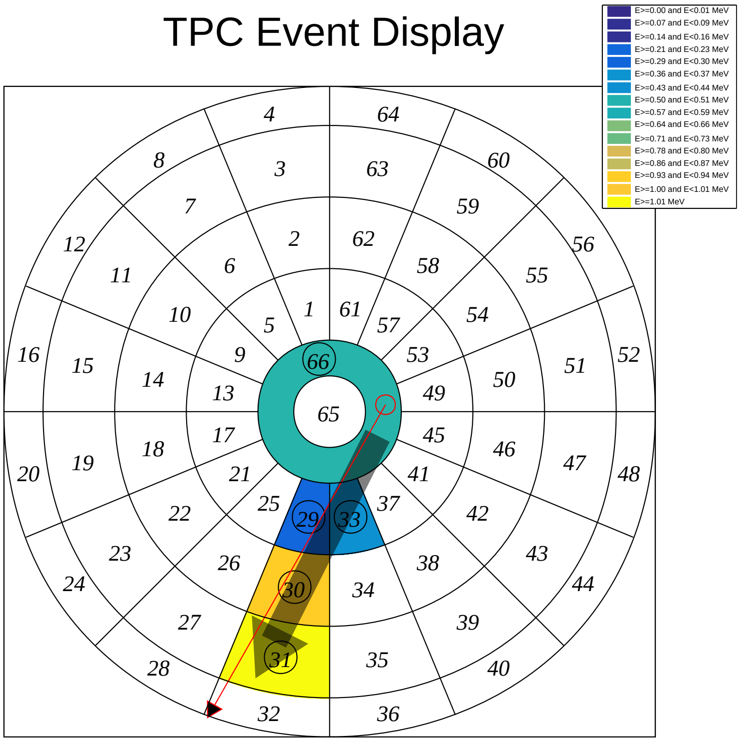

Figure 4.12: One example track to demonstrate the track fitting algorithm. The mean position on each ring is averaged using the energy and then a fit in (r, φ)-plane is performed. The track is drawn in black according to the fit results ($d = (16.50 \pm 0.05)$ mm, $\alpha = (-0.47 \pm 0.06)$ rad, $\chi^2/\text{dof} = 1.44/2$), starting from the shortest distance to the centre until the outermost hit ring. The information of the corresponding silicon event is drawn in red. This track contains the information of the scattering vertex point as well as the direction and the kinetic energy, drawn as range, of the recoil proton, which is described in section 4.4.5.

a (r, φ)-coordinate-system in order to have a smaller correlation in the error of the ring position. The linear fit in (r, φ)-coordinates looks like the following:

$$r(\varphi) = \frac{d}{\cos(\alpha - \varphi)}; \text{ and the inverted function } \varphi(r) = \alpha \pm \arccos\left(\frac{d}{r}\right) \quad . \tag{4.3}$$

The sketch in figure 4.13 shows the variables. The "+" solution works for values where φ is larger than α and the "$-$" solution for $\varphi < \alpha$. The parameter d is the minimal distance to the centre and α describes the angle to the normal vector. It is decided for every data point if the positive or negative solution should be used.

Tracks which are going radially out of the TPC readout cannot be fitted with this function, so they are collected beforehand.

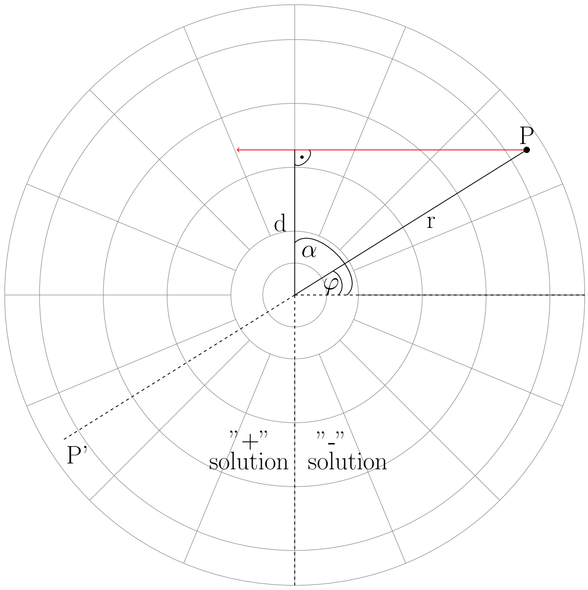

Figure 4.13: This sketch displays the variables used for the parametrisation of a linear curve in the (r,φ)-coordinate-system. It is visible as well that for the same radius, two solutions for φ exist which lead to point P and P'. The "+"-solution is valid for $\varphi > \alpha$, the "-"-solution for $\varphi < \alpha$.

4.2.5 φ-distribution

The φ-distribution of the recoil proton measured by the TPC can be seen in figure 4.14. One can see 16 spikes which come from events that only hit one pad per ring while going radially from the centre to the outer rings. Additionally, one can see less events between $\varphi = 2 to 3$ rad. This might originate from the increased threshold around pad 7 which leads to less measured events.

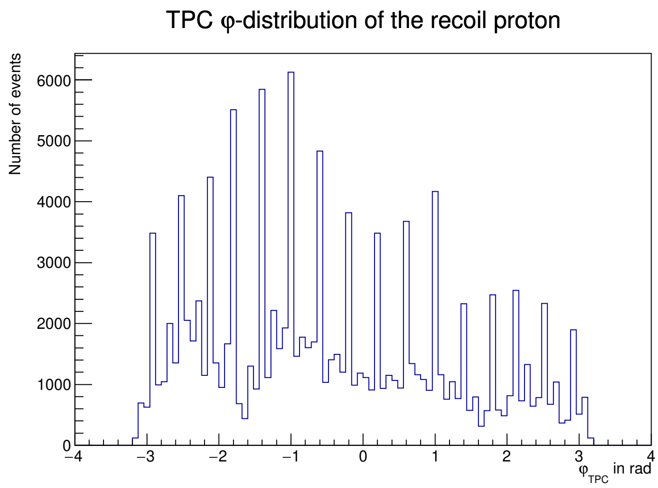

Figure 4.14: The figure shows the φ-distribution measured by the TPC. One can see 16 spikes. Additionally, one can see less events between φ = 2 to 3 rad.

4.3 Combining silicon and TPC data

The combination of silicon and TPC data is done with the timestamp. Looking at the difference between both timestamps in a window of ±500 µs one notices a small peak between 18 µs and 82 µs, see figure 4.15. This peak has 2447 events. By counting the events outside of this time window and scaling these to the time window, one can estimate 1555 noise events in the peak which leads to 892 correctly matched events. The TPC measures only events where the scattering has taken place inside the readout area, which is between anode and cathode: $24.3 \leq z/\mathrm{cm} \leq 46.8$. The cut on the z-vertex to be between those positions is enlarged by the corresponding resolution which is described in section 4.1.5. As the radial cut on the silicon data implies that the muon beam has to hit the TPC in the centre, one can cut on TPC tracks that hit at least one of the central pads 65 or 66. This improves the signal-to-noise ratio of the beam to 700/16. In table 4.3 it is visible that the cuts throw away 21.5 % of the data while cutting away 99.0 % of the noise.

Cut	Signal	Noise	Uncertainty
θ >0.2 mrad and radial cut	892	1555	11
θ >0.2 mrad, radial cut and z-vertex cut	762	153	4
θ >0.2 mrad, radial cut and centre cut	749	147	4
θ >0.2 mrad, radial cut, z-vertex cut and centre cut	700	16	1

Table 4.3: Signal and noise of the time difference peak for different cuts. The noise is calculated with all events between −500 µs and 500 µs outside of 18 μs and 82 μs, scaled with the factor 64/936. The signal is calculated as the number of events between 18 μs and 82 μs minus the noise calculated before. The uncertainty is given by the square root of the number of events between −500 µs and 500 µs outside of 18 μs and 82 μs, scaled with the factor 64/936.

4.4 Combined data

After improving the signal-to-noise ratio of the peak and then cutting on the time difference between 18 and 82 μs the resulting events are mainly matching silicon and TPC events. Without additional cuts, 892 events excluding an average of 1555 mismatched events are measured, which does not fit our predictions of 3280 combined elastic scattering events, given in section 3.8. In the following, possible reasons for this discrepancy are discussed.

The area covered by the scintillators and the silicon tracking stations is roughly equal. Therefore, any misalignment causes a loss of events. By extrapolating events of run 282500 measured by the silicon trackers to the trigger positions, one can see the full trigger area. Thus, no big misalignment is expected. Nonetheless, it is possible that not all events at the edges of the area are measured. This is emphasized by looking at the beam profile shown in figure 3.7. The area of the beam at the upstream entrance pipe is given by 5 cm × 4 cm and therefore covering only 57.1 % of the trigger area (7 cm × 5 cm). The beam is not centred in the x-position, increasing this effect, which is not estimated here.

The reconstruction of a track requires to have at least 7 hits in the detectors and is therefore coupled with the silicon tracking acceptance and efficiency. Looking at the first chunk of run 282500, 97.8 % of the incoming tracks and 84.7 % of the scattered tracks pass this requirement. The combined effect is 82.8 %.

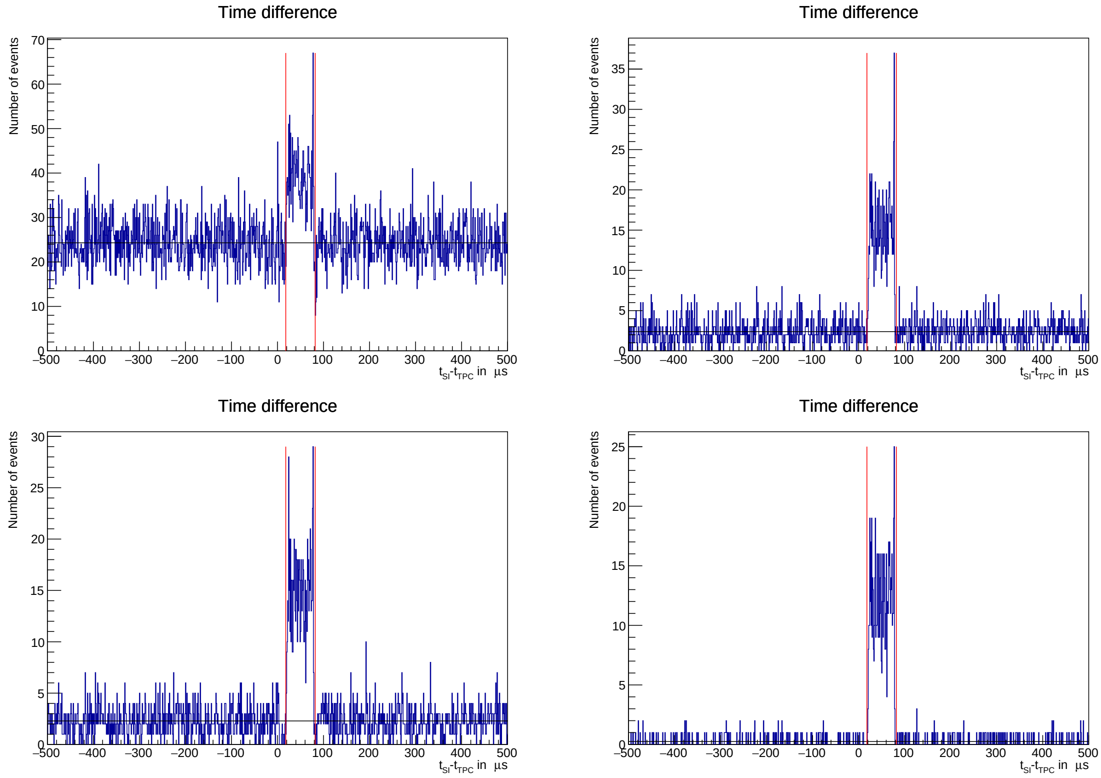

Figure 4.15: The difference between the timestamps of the silicon detector and the TPC with different cuts (top left: θ and radial, top right: θ, radial and z-vertex, bottom left: θ, radial and centre, bottom right: θ, radial, z-vertex and centre). A peak is visible between 18 and 82 μs. The cut on the time difference is plotted with the two vertical lines (red), the average noise level is indicated with the horizontal line (black).

Additionally, the effect of the radial cut was only estimated for the incoming beam. For the lowest scattering angle of 0.2 mrad, which is the most probable value, the maximal effect of this can be estimated. An event scattering near the anode with this angle, changes its transversal component by 71.4 µm over the distance of 0.357 m to the downstream end cap. By reducing the radius from 1.99 cm to 1.98286 cm, the number of events is only reduced by 0.716 %. This effect is larger for larger scattering angles, which are less probable. Therefore, this effect is negligible.

Furthermore, the efficiency of the TPC was not estimated during the measurement. An upper limit can be given with the dead time of $\tau = 108\,\mu\text{s}$. With a maximum measured TPC trigger rate of $r_{\text{TPC,meas}} = 230\,\text{s}^{-1}$, this leads to a loss of 2.5 % [40]:

$$r_{\text{TPC,real}} = \frac{r_{\text{TPC,meas}}}{1 - r_{\text{TPC,meas}} \cdot \tau} = 235.9 \quad . \tag{4.4}$$

Implying these three correction factors, approximately 1500 events are expected, which is still much more than the measured 892 ± 11 events.

For the further analysis, 700 events with an average of 16 mismatched events are used. To cross-check the combination, one can look for different effects like the drift velocity of the electrons in the TPC. Additionally, the change in the angle which is measured by the silicon-trackers should correspond to a scattering process. The calculated energy should be measured within the TPC.

4.4.1 Drift velocity

As the electrons need to drift the anode, an event which occurred near the anode (z = 24.3 cm) is measured earlier in the TPC than an event near the cathode (z = 46.8 cm). Both events should be measured equally fast in the silicon detectors. Therefore, the time difference (t_{SI}-t_{TPC}) should be larger at the position of the anode than near the cathode. A negative slope is visible in figure 4.16 and the extracted drift velocity (3.99 ± 0.18) mm µs^{-1} is larger than the estimated value of 3.702 mm µs^{-1}.

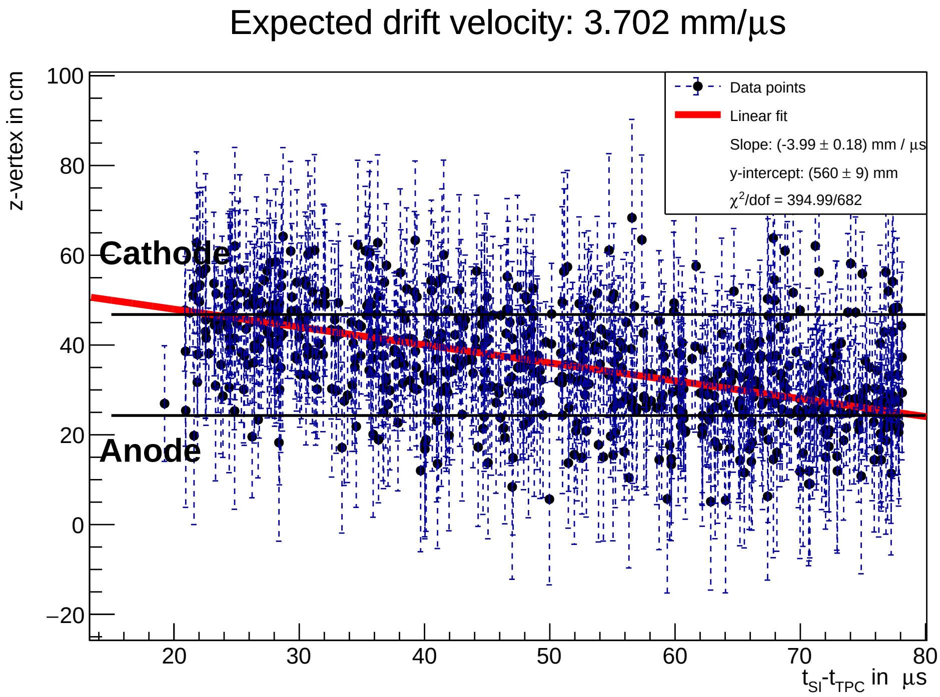

Figure 4.16: The figure shows the z-vertex versus the time difference for events that were measured with a pressure of 8 bar. Events near the anode (z = 24.3 cm) should have less drift time and are therefore measured earlier in the TPC. This leads to a higher time difference. Subsequently events near the cathode (z = 46.8 cm) have a higher drift time and a smaller time difference.

4.4.2 Verify the assumption of a recoil proton

The energy deposited on the first two rings of the TPC can be simulated for a recoil proton with different kinetic energies starting at the centre [22]. A proton with a kinetic energy of roughly 1.5 MeV starts depositing energy on the second ring. For a lighter particle this is shifted to smaller energies. In picture 4.17 the simulation, all TPC events and the matched events are drawn. It is visible that the matched events are in good agreement with the simulated curve, implying that these events are protons.

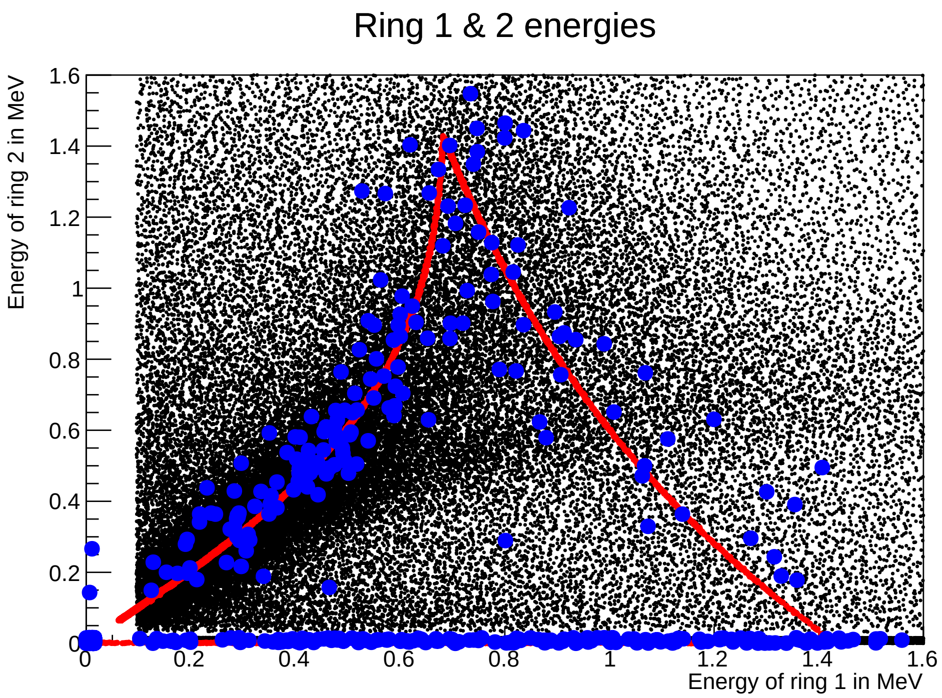

Figure 4.17: The simulation of the energy loss of a proton starting at the centre of the TPC readout on ring 1 and 2 is shown in red. All data points measured in the TPC are marked in black. The data points matched with the silicon tracking stations are shown in blue. There are less events on the right flank. A reason could be the smaller kinetic energy range of a proton to be stopped between the first and second ring with respect to a proton that reaches the third ring and further.

4.4.3 Energy comparison

The kinetic energy of the recoil proton can be either calculated by the scattering angle θ determined by the silicon detectors[5] or measured directly by the energy deposited in the TPC. Protons with a kinetic energy of at least 3.5 MeV in 8 bar hydrogen and 2.25 MeV in 4 bar hydrogen have a range of roughly 10 cm and can therefore escape the readout plane of the TPC. In figure 4.18 these events are cut out. As there is a hard cut at 744 keV ($\theta = 0.2$ mrad) for the silicon data, the corresponding fit is done only for TPC energies larger than this value. The resulting is slope is 0.89 ± 0.04, meaning that the energies measured in the TPC are larger than the calculated energy of the silicon stations. This effect is probably originating from the cut on the scattering angle. This leads to a larger y-intercept of the fit which is highly correlated to the slope with a correlation coefficient is -0.9318.

4.4.4 φ-difference

The rotation of the TPC reference system was not marked beforehand but it can be measured by taking the difference of the φ-angle measured by the silicon trackers and the TPC. This rotation is of no further interest, since it is an arbitrary value. In figure 4.19 the rotation value of $\Delta\varphi = -2.075$ rad is

[5] The kinetic energy is calculated in equation (B.3) in section B.2. The corresponding uncertainty due to the uncertainty of θ and of the beam momentum is given in equation (B.4) in section B.3.

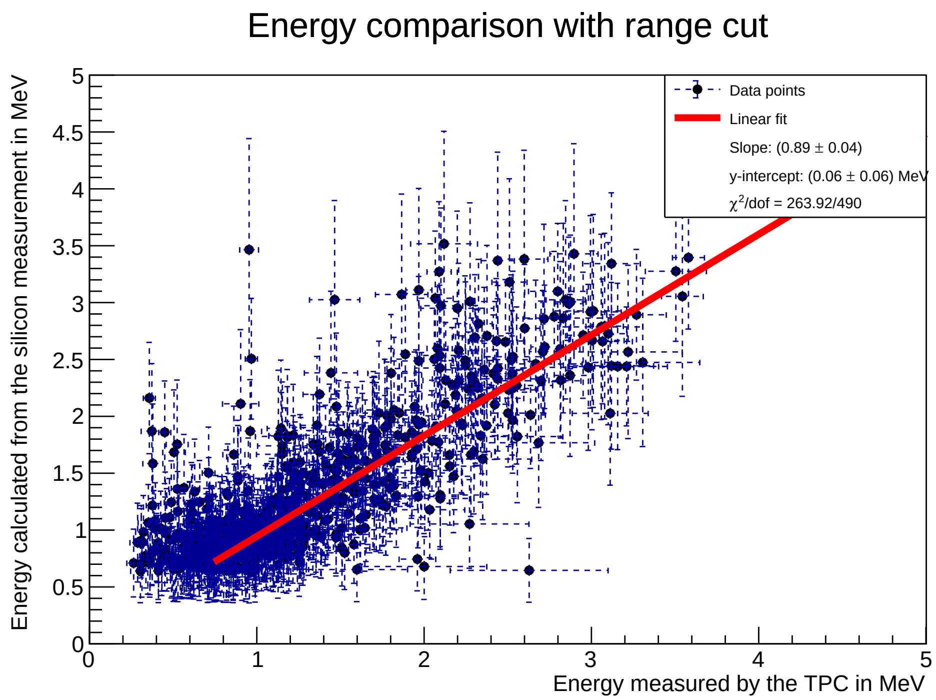

Figure 4.18: The energy calculated from the scattering angle θ measured by the silicon trackers versus the energy deposit measured in the TPC. The TPC events are cut so that events which can escape the active readout due to a range larger than 10 cm are taken out. The fit is limited to energies larger than 0.744 MeV in order to account for the θ-cut on the silicon data.

already subtracted and after this, the mean value is around 0. The TPC reference system is rotated around this angle with respect to the silicon coordinate system. The peak is broad due to the finite pad-size of the TPC detector, with each pad covering a φ-range of 0.3927 rad.

4.4.5 Tracks of the TPC and silicon measurement

Using the translation of the silicon and TPC coordinate system by having the central position of the beam windows of the TPC in the silicon system and $\Delta\varphi$ between both systems, one can plot the information of the silicon tracking system into the TPC measurement. Therefore, the xy-vertex measured by the silicon tracking system is translated to the origin of the TPC system and then rotated according to $\Delta\varphi$. The direction of the proton is given by the silicon φ-angle minus $\Delta\varphi$. The kinetic energy of the proton given by the scattering angle in the silicon system can be transformed into a range of the recoil proton in the hydrogen volume [32]. Then all information about the proton we have from the silicon tracking stations are given in the TPC system and can be plotted. In figure 4.12, we can see that both are in good agreement. The range of the proton measured by the TPC is slightly smaller, which might originate from the fact that the range is a statistical process.

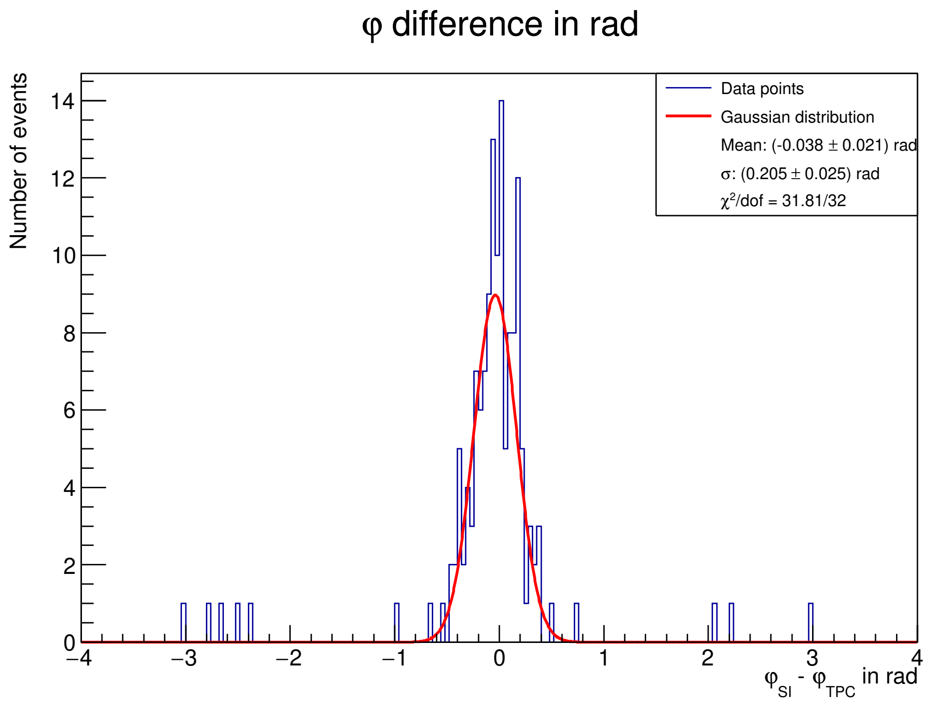

Figure 4.19: The φ-difference between the calculation from the silicon positions and the result of the tracks in the TPC. The planes of the silicon stations and the TPC readout plane are rotated by an angle of $\Delta\varphi = -2.075$ rad which is already subtracted in this plot.

CHAPTER 5

Monte Carlo simulation with Geant4

Monte **C**arlo (MC) simulations are performed in order to extract the expected resolution of the silicon tracking detectors. Additionally, correlations of kinetic energy and direction, given in φ, of the recoil proton are compared between the reconstruction in both detector systems and the generated "Monte Carlo truth" value. The working principle of the simulation program Geant4 is described in the following section and simplifications of the simulation are mentioned.

5.1 Geant4

Geometry **an**d **t**racking is a program, which simulates particles in matter [41][42]. In the following, the required input from the user and the working principle of the program is described.

The user has to provide a physical model, where all processes of the particles are defined. There are many predefined models that are designed for high-energy or low-energy processes or even optimized for a low processing time. In the further analysis, the model "QGSP_BERT_HP" is used. It stands for "quark gluon string model", which uses the Bertini cascade for protons and other particles below 10 GeV.

In the next step, one has to provide the material that is going to be simulated. The material implementation of the silicon stations is taken from the TGEANT documentation [43]. The model of the TPC is based on [27] and then modified to fit the right geometry at the time of the experiment. A pressure of 8 bar hydrogen is used. The bending of the beam windows is neglected. Also the grid, the holding structure of the cathode and the cables are not simulated. The z-positions of the detectors are taken from the results of the test measurement. As a simplification, the rotation away from the z-axis is not considered here, so all x and y positions are set to zero. The setup is shown in figure 5.1.

Then, one can define primary particles. The momentum of the incoming beam muon is set to 190 GeV. For the elastic scattering simulation, a vertex is simulated following a flat distribution with the xy-coordinates between -2 to 2 cm and the z-coordinate between the anode and the cathode. Corresponding to the Rosenbluth cross-section, see section 2.1, the scattering angle θ is simulated between 0.18 to 5 mrad for studies of the energy correlation. For investigations of the φ-distributions, θ is simulated following the Rosenbluth cross-section between 0.5 to 5 mrad, as protons with larger energies are required in order to reconstruct the direction in the TPC, because at least three rings have to be hit. With this, the kinematics of all three particles can be set. The incoming muon starts at the vertex and flies in the upstream direction. This should have no effect on the simulation results. The

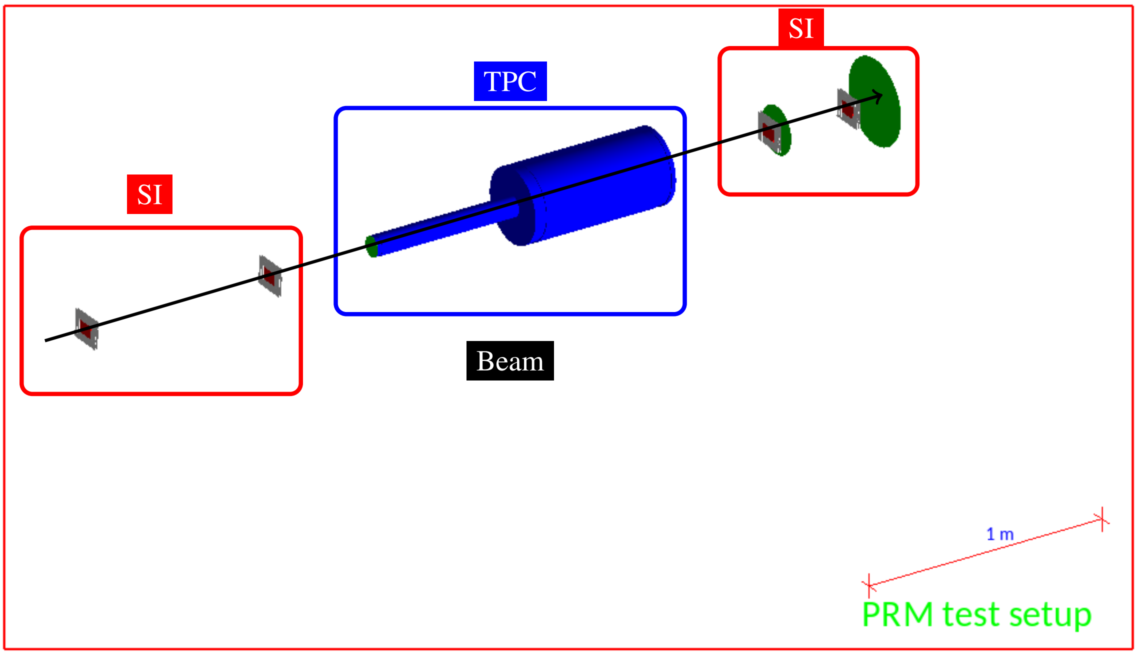

Figure 5.1: The test setup as it is implemented in the Geant4 model. The silicon stations are marked in red with the supportive structures in grey. The beam windows and the windows of the conical cryostat around the downstream silicon stations are pictured in green. Structures outside the beam area like the cone of the conical cryostat and larger supportive structures of the silicon stations are implemented but not drawn here.

incoming muon is assumed to have no beam spread into the transversal plane. For the simulation of the resolution of the silicon tracking detectors, the xy-coordinates of the vertices are created like described above. The z-coordinate is set to the position of the anode or cathode and distributed with their corresponding thickness of 20 µm. The θ-values are fixed and not randomly drawn.

Geant4 has the following procedure. A run is started with a given number of events. Each event starts with the simulation of the first primary particle. Depending on the energy of the particle and the radiation length of the material, a step size is calculated. The step size inside the active volume of the TPC is limited to be maximal 1 mm. The energy loss for each step inside the active volume of the TPC and inside the silicon tracking detectors is stored. When the primary particle creates a new particle, in essence electrons, these secondary particles are stored and their behaviour is simulated after the simulation of the primary particle has ended. A simulation of a particle ends, when it has no kinetic energy or when it leaves the given geometry boundaries. After all primary particles and their corresponding secondary particles are simulated, the event ends. At this point, the output data is saved. In order to process the output data of the silicon tracking detectors with CORAL, the existing output format of TGEANT is used. The run ends when the given number of events is simulated.

5.2 Processing of the simulated data

The hits of the silicon tracking detectors are reconstructed in CORAL. Therefore, one has to provide the positions of the detectors, which is known perfectly for the Monte Carlo data. The material of the experiment should be provided as well. This is exported from the Geant4 model using the **V**irtual **G**eometry **M**odel [44]. The reconstruction inside CORAL smears all hits by the estimated spatial detector resolution of 15.8 µm for the U- and X-planes and 14.9 µm for the V- and Y-planes. The spatial resolution estimated by the pitch overestimates the uncertainty on most planes and does not simulate the faulty planes SI02U and SI03X. Spatial resolutions between 9.8 to 16.6 µm are extracted in real data for most planes, 43.8 µm for SI03X and SI02U was not working [45].

The TPC response is simplified by neglecting effects from diffusion and the drift velocity. Every hit has xy-coordinates, which correspond to one pad. Using this information, the deposited energies for every pad can be summed up. The beam noise is taken into account by smearing the pad energies with a Gaussian distribution and a standard deviation of 30 keV.

Some cuts are applied on the data to match the expected behaviour of the real data. For the resolution studies, see the following section 5.3, the incoming and scattered beam have to pass a radial cut on the downstream endcap pipe with a radius of 1.99 cm. The cut at the position of the cathode is not applied, as this holding structure is not simulated.

For the studies of the φ and energy of the recoil proton, see section 5.4, additional cuts are applied. At least one pad has to have an energy larger than 200 keV, which corresponds to the TPC trigger. The z-vertex has to be reconstructed within an 1 σ-uncertainty inside the active TPC volume. It is required that one of the two central pads is hit, which is like in the real data analysis defined by an energy larger than 3 times the energy resolution. The cut on the scattering angle $\theta \geq 0.2$ mrad is applied for the φ correlations but not for all energy correlations.

5.3 Resolution studies

The z-resolution of the scattering vertex is extracted in a similar way compared to real data. Events with different scattering angles θ are simulated at the z-position of the anode and the cathode smeared over the corresponding thickness of 20 µm. Fitting a single Gaussian distribution to both peaks for each simulated θ-value, gives the resolution of the z-vertex for this θ-value. The results are given in the table F.1 in the appendix F. This resolution follows a $1/\theta$ curve like it was extracted from real data, see figure 5.2. The resolution at the position of the cathode is slightly worse than at the position of the anode.

The θ-resolution can be measured directly with Monte-Carlo simulations. An event with a specific scattering angle is generated, and after the propagation of the particles using Geant4, reconstructed in the silicon tracking stations. The resulting θ-spectrum is fitted with a Gaussian distribution. The results are given in table F.2 in the appendix F and the σ-widths are depicted in figure 5.3. Additionally, the uncertainty on the scattering angle is estimated using the previously extracted z-vertex resolution with equation (B.1) given in section B.1. It is visible that this estimation overestimates the uncertainty.

As the measured θ-uncertainty is larger than the estimated multiple scattering of 17.9 µrad for a beam momentum of 190 GeV, see section 3.7, the setup can be improved by increasing the distance between the silicon tracking stations. When this distance is enlarged by 2 m, the resulting combined uncertainty on θ is roughly 16 µrad, see figure 5.4, which is below the effect from only multiple

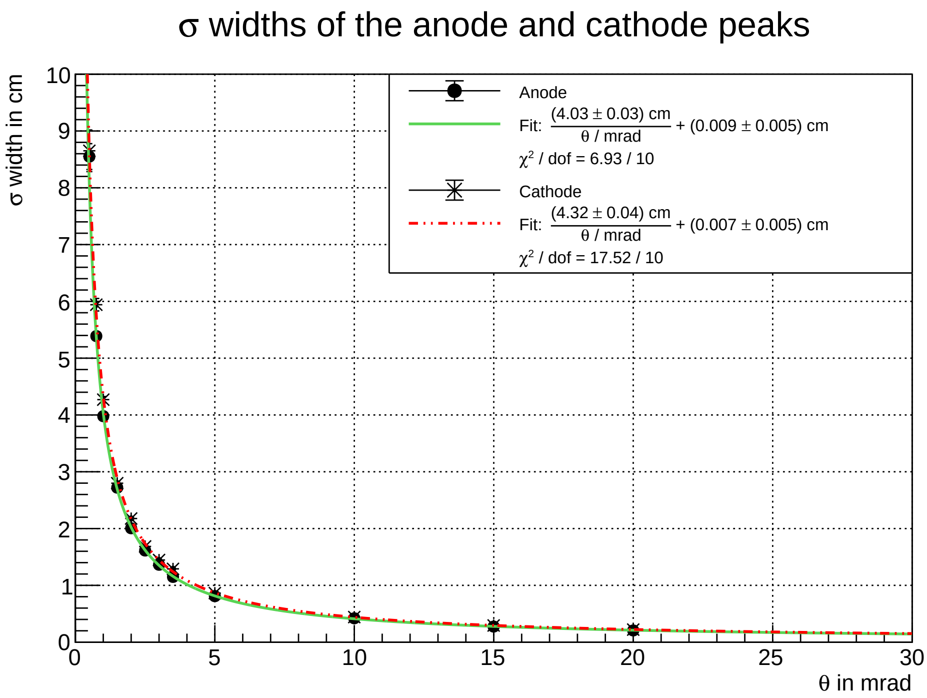

Figure 5.2: The z-vertex resolution of MC simulated events at the position of the anode and the cathode. It is visible that the z-resolution has a slight dependence on the z-vertex. For both structures, an $1/\theta$ curve is fitted.

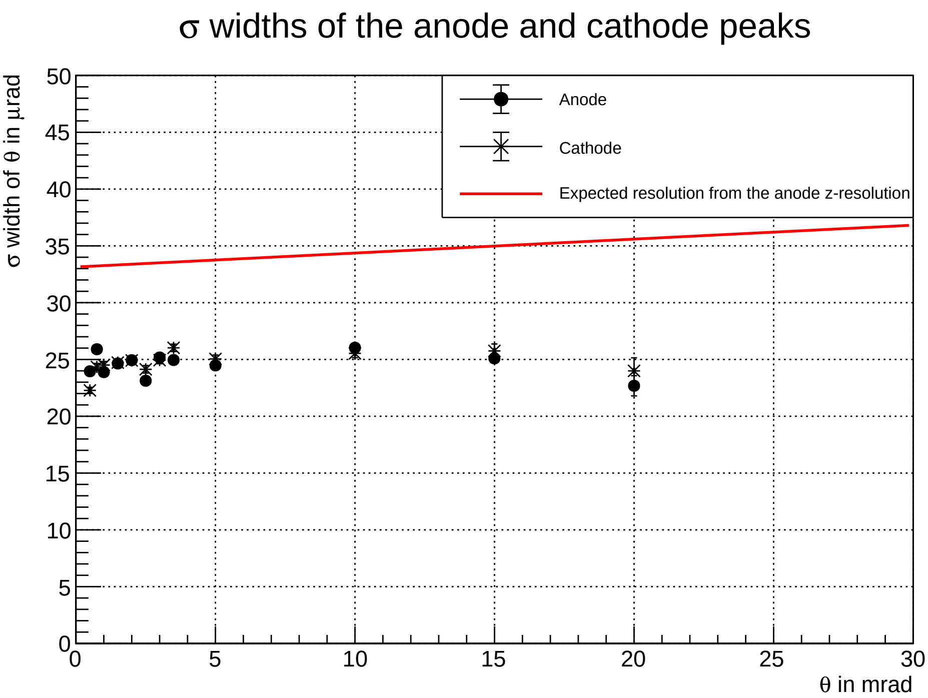

Figure 5.3: The θ-resolution can be extracted from the simulation. The estimation from the z-resolution is drawn in red. It is visible that gives an upper limit on the uncertainty.

scattering. The reason for this resolution, which is better than the expectation from multiple scattering, is that the material of the first and last silicon tracking station will not contribute completely to the uncertainty of the scattering angle[1]. Thus, any larger distance would only decrease the acceptance of the setup.

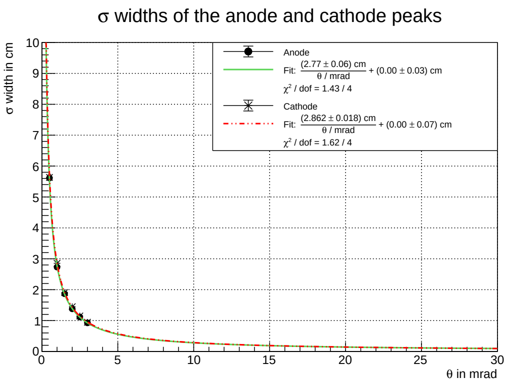

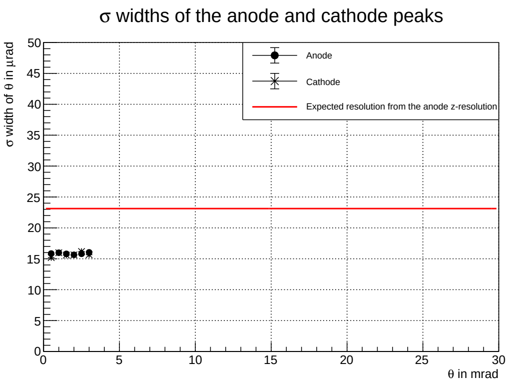

Figure 5.4: After shifting the first silicon station SI01 1 m upstream and the last station SI04 1 m downstream, resulting in a total distance of 5.28 m, the resulting z-resolution can be seen on the left and the θ-uncertainty on the right.

5.4 φ and kinetic energy of the recoil proton

The primary interaction is simulated in the active volume of the TPC with θ following the Rosenbluth cross-section between 0.5 to 5 mrad and 0.18 to 5 mrad for studies of the φ-angle and the kinetic energy of the recoil proton, respectively.

The direction of the recoil proton and therefore the φ-angle can be reconstructed like in real data. The φ-distribution was simulated with equal probabilities. The reconstructed distributions can be seen in figure 5.5. The distribution measured in the silicon stations is nearly flat with some spikes and dips at 0, $\pm\pi/2$. and $-\pi$ rad. The reconstruction inside the TPC shows 16 spikes, which are coming from the wide pads. These events only hit one pad per ring and have therefore only one possible φ-value in the tracking algorithm. The difference of the φ-angle reconstructed from the silicon tracking stations to the TPC is depicted in figure 5.6. The difference of the reconstructed to the simulated φ-angle is given in figure G.1. It is visible that the resolution of the silicon tracking stations, (0.03588 ± 0.00014) rad, is better than the resolution of the TPC, (0.1889 ± 0.0006) rad, which is limited by the pad size of 0.3927 rad. One can see as well that the distribution is not a pure Gaussian function but has a plateau instead. This plateau is probably coming from events which do not hit more than one pad per ring. The uncertainty on the difference between both detector systems of (0.1971 ± 0.0006) rad is thus dominated by the TPC pad width.

[1] When the effect of multiple scattering is calculated for only three silicon tracking stations and a beam momentum of 190 GeV, the result is 15.98 µrad.

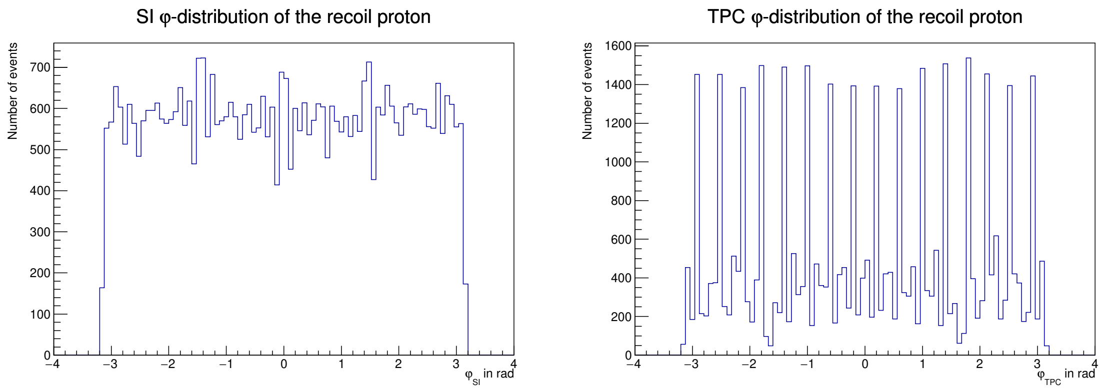

Figure 5.5: The φ-distribution of the recoil proton reconstructed from the silicon tracking stations (left) and the TPC (right). The φ-distribution was created with equal probabilities. The reconstruction of the silicon tracking stations is nearly flat with some spikes and dips at 0, $\pm\pi/2$. and $-\pi$ rad. The φ-distribution measured by the TPC has 16 clearly visible peaks, which originate from events that only hit one pad per ring.

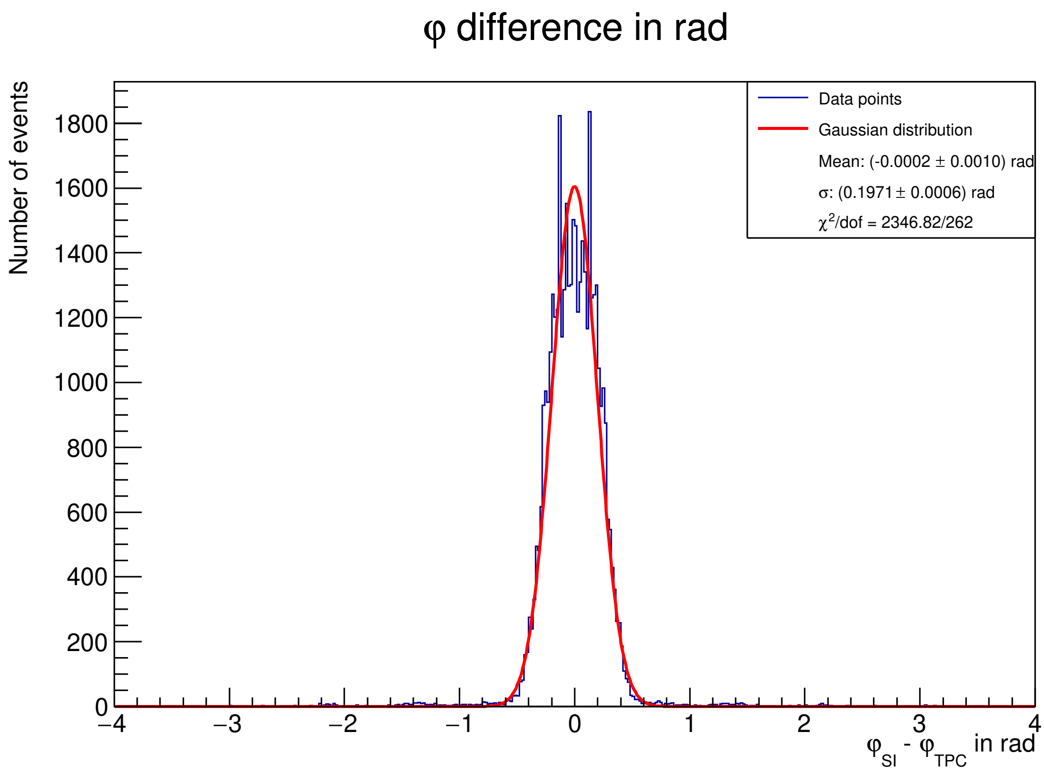

Figure 5.6: The difference of the reconstructed φ-angle between the silicon tracking stations and the TPC.

With the simulation, it is possible to compare the influence of different cuts on the energy correlation. This is done for the reconstructed data from the silicon tracking stations and the TPC in comparison to the MC truth value as well as for the comparison of both detector systems. For all pictures, a cut was applied that the range of the recoil proton inside the hydrogen volume is smaller than the distance to the end of the active readout volume. This should exclude events, where the recoil proton leaves the TPC and therefore does not deposit the total kinetic energy inside.

The comparison of the silicon data reconstruction with respect to the MC truth values is shown in figure G.2. The slope with no additional cuts is compatible with 1. By applying the cut on the scattering angle $\theta \geq 0.2$ mrad, this is not valid any longer. This behaviour originates from the uncertainty of the reconstruction. Near the threshold for the cut, only events that are reconstructed with larger scattering angles, pass this cut. This breaks the symmetry of the reconstruction uncertainty. For the reconstruction of the kinetic energy of the recoil proton in the TPC, such a behaviour is not seen in figure G.3.

Comparing the energy correlation of the TPC and silicon measurement in figure 5.7, the slope is close to 1. After applying the cut on the scattering angle, the slope is decreased to 0.613 ± 0.011, as it was seen in the correlation between the silicon and Monte Carlo truth data. Accounting for this hard cut by starting the fit at $T_{\mathrm{p,TPC}} = 0.744$ MeV, improves the slope to 0.715 ± 0.012. Starting the fit at much larger energies is not reasonable, as the measurement range of the TPC is limited by the range of the proton to roughly 3.5 MeV at 8 bar hydrogen.

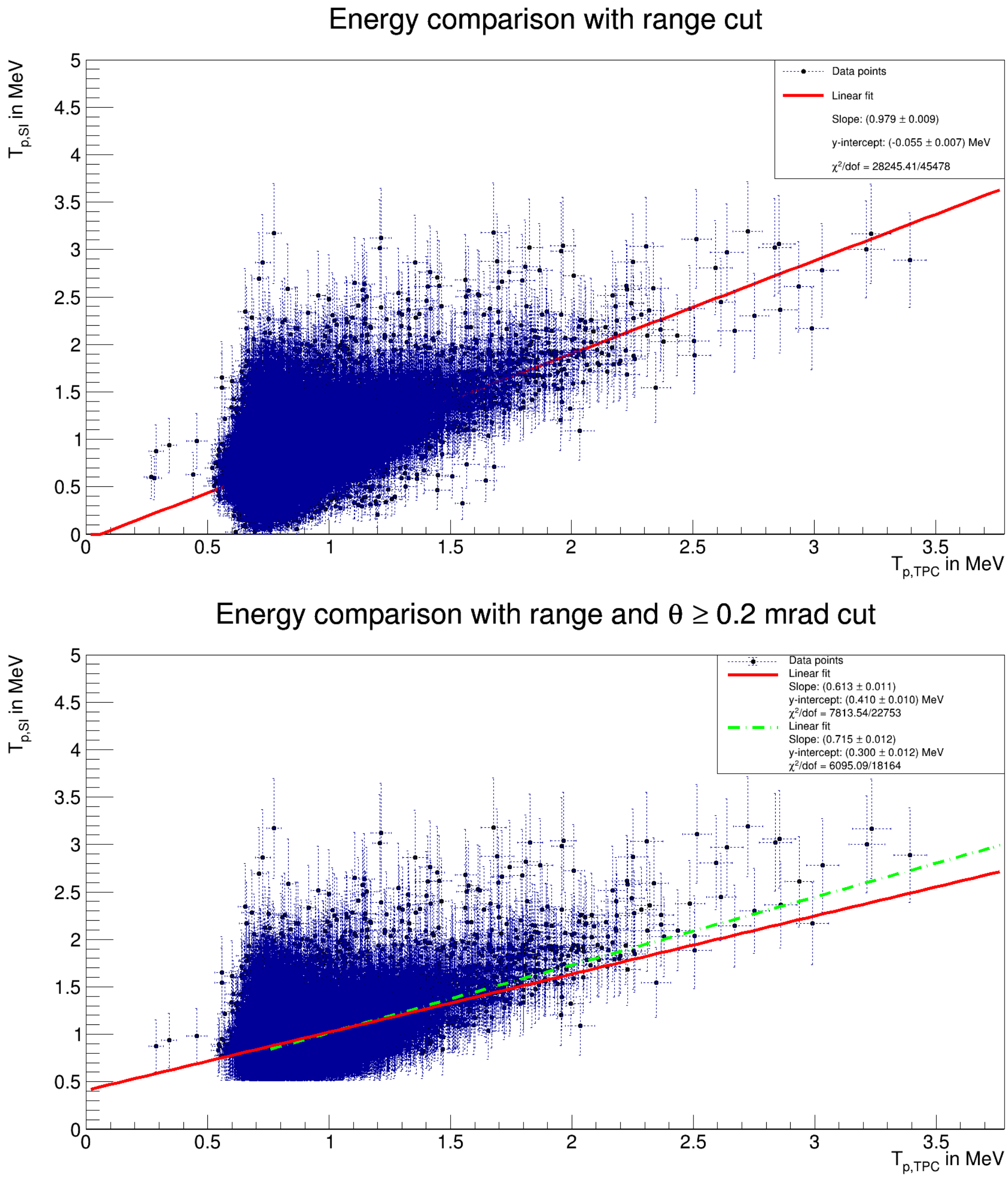

Figure 5.7: The energy correlation between the reconstruction of the silicon tracking stations and in the TPC is plotted (top) and with the additional cut on $\theta \geq 0.2$ mrad (bottom). For the bottom plot, two linear functions are fitted, one covering the whole range (red) and the other one starting at $T_{\mathrm{p,TPC}} = 0.744$ MeV (green, dashed).

CHAPTER 6

Discussion

In this chapter, the results from the real data analysis and the Monte Carlo simulation are discussed.

The run-by-run alignment improves the precision of the reconstructed z-vertex position roughly by a factor of 2.3, see section 4.1.5. This is a large improvement, which originates from a detector shift larger than the spatial resolution over the duration of the experiment. After the run-by-run alignment, the z-vertex resolution measured in real data is comparable with simulation results, given in section 5.3, even with several simplifications of the simulation. Firstly, events are simulated at certain θ-values and not distributed continuously like in real data. Secondly, the incoming beam is simulated to follow the z-axis with no transversal momentum component. Thirdly, the material of the grid and the cables is missing in the simulation, which leads to less multiple scattering. The spatial resolution is given by the pitch$/\sqrt{12}$. The propagation of the z-vertex resolution to the uncertainty of the scattering angle was studied in the simulation and it was observed that this propagation overestimates the uncertainty, see section 5.3. Therefore, a better model to propagate the resolution has to be created by extending the model from one to two transversal dimensions. Additionally, the direction of the incoming muon should be included.

The expected correlation of the kinetic energy of the recoil proton from the TPC and silicon tracking measurement was studied in the simulation, see section 5.4. It was found that the cut on the muon scattering angle leads to a slope, which is smaller than 1. This can be compensated to some extent by limiting the fit to TPC energies, that are also larger than the kinetic energy calculated at this scattering angle. In the real data analysis, a similar effect can be seen, see figure 4.18. The slopes of both analyses are not comparable, which might come from some simplifications of the simulation. Still, one can expect that the correlation of energies in real data is given, even if the slope is different from 1. The main uncertainty of the measurement for low energetic protons originates from the silicon tracking reconstruction. This shows that the combination of these data sets with the reconstruction of the TPC will greatly improve uncertainties on the momentum transfer.

Distributions of the azimuthal φ-angle are measured with both detector systems. The reconstruction with silicon tracking stations has prominent peaks at $0, \pm\pi/2, \pm\pi$, which are expected to come from a bias in the silicon readout if the muon scatters mainly on the silicon planes, see figure 4.9. This distribution is flat for the combined events, see figure C.5. In the Monte Carlo simulation, this distribution is flat as well because a primary vertex was simulated inside the TPC volume, see figure 5.5. Therefore, events that mainly scatter on the silicon planes are not simulated. There are several structures in the reconstruction of φ from the TPC, see figure 4.14. Events that hit only one pad per ring lead to one specific φ-value, thus yielding 16 peaks. Those are visible in distribution of real and Monte Carlo data. The smaller number of events between 2 to 3 rad in real data can be explained by the larger threshold for pads around the α-source. This threshold could be implemented in the simulations to cross-check this effect but is currently not included.

There is a discrepancy between the expected and measured number of 892 ± 11 events. By estimating the effect from the efficiency of the silicon tracking stations and the dead time of the TPC as well as a possible misalignment between the silicon tracking stations and the trigger, the expected number of events is reduced from 3280 to approximately 1500, which is discussed in section 4.4. The efficiency of the TPC was not studied during the measurement, which could reduce the number of expected events further.

CHAPTER 7

Conclusion and Outlook

In this thesis, data of the 2018 test experiment was analysed. The data of the silicon tracking station stations was used to select for scattering events inside the TPC. After combining both data sets, correlations of the recoil proton kinematics were studied. In order to compare the results, Monte Carlo simulations were carried out. In this chapter a short summary of the analysis is given. At the end, the current status of the main experiment in 2022/2023 is presented.

It is clear that the run-by-run alignment reduced the uncertainty on the muon scattering angle. However, there is a slight misalignment according to the residuals at the beginning and the end of each run. In order to reduce this, the silicon trackers should have a stabilised temperature in the main experiment in 2022/2023. This can be achieved by cooling the silicon tracking stations, which would also improve their spatial resolution. Alternatively, the alignment could be done for shorter time periods. The quality of the vertex finding can be improved by having a larger distance between the stations, reducing the uncertainty on the scattering angle and the vertex point. For the test experiment, it was shown that enlarging the distance by 2 m, which is planned for the final experiment, is sufficient in order to be only limited by multiple scattering. In order to achieve an even better resolution, the amount of multiple scattering has to be reduced.

The α-source of the TPC had no large effect on the combined data of the test experiment. Nevertheless, it is planned to shield the α-source during the measurement of the main experiment. The calibration of the TPC energies depended on the time as well as on the z-vertex position due to attachment. Therefore, a constant refilling of the hydrogen gas to minimise the effects of gas impurities would be preferable. Additionally, the energy of the α-source should be monitored frequently like in the test experiment to make sure that the calibration is constant with time. The drift velocity can be estimated by the gas parameters and was measured in advance with the drift time. These values differ from the drift velocity extracted from the z-vertex versus time difference plot. Thus, it would be good to have a separate measurement of the drift velocity, for example by a low-intensity laser system. Even when the TPC was originally built for a thin electron beam, it was shown that the TPC can produce good results within a broad muon beam. There are possible improvements of the TPC readout structure, which can be simulated. With more rings of smaller radii, the direction information of recoil proton can be extracted at smaller kinetic energies, thus giving an additional parameter to reject background events. This has the disadvantage that it may lead to more noise, deteriorating the energy resolution. Different geometric shapes may be suitable for a broader beam. Shifting pads on neighbouring rings should improve the spatial resolution without introducing additional noise.

The matching of different DAQ systems with the timestamp is working. This can be seen in the correlation of the energy and the direction of the recoil proton. By looking at the energy uncertainty, it is clear, that the TPC massively improves the resolution in the low Q^2 region, while the silicon trackers can select possible candidates for elastic scattering. For this reason, such a setup is well suited to measure the cross section and form factors over a large Q^2 region between 0.001 to 0.040 GeV^2, which is planned for the main experiment 2022/2023.

Several simplifications were done in the simulation. These are the missing transversal momentum component and energy spread of the incoming muon beam. The material of the grid and the cables is currently missing in the simulation. The spatial resolution and efficiency of the silicon tracking stations is not given by the real data values. For the simulation of the TPC, beam noise was only introduced by smearing energies with a Gaussian distribution. Nevertheless, many effects can be reproduced with the simulation. The z-vertex resolution does also compare quantitatively to the real data value. The values of the energy correlation do not converge quantitatively to the values of real data, which will originate from these approximations. Furthermore, the systematic uncertainty on the simulation results due to the given physical model should be estimated.

The current planning of the experiment in 2022/2023 is shortly described in the following. Further details can be found in [13][14]. The data taking should run with a 60 GeV or 100 GeV muon beam. Silicon-pixel detectors with low material budget should be used to achieve a high resolution on the scattering angle and to reduce multiple scattering. The distance between the silicon detectors on both sides should be enlarged to 3.5 m or 3.1 m for a TPC with two or four interaction regions, respectively. Multiple scattering should additionally be limited with a helium filled pipe between the silicon trackers.

It is discussed if scintillating fibres or gas electron multipliers can be used as a kink trigger in order to reduce the trigger rate.

The TPC will have either two or four interaction regions with a drift length of 40 cm. The readout will be segmented into eight rings. The TPC will run at a pressure of 4 and 20 bar. A gas purity of hydrogen below 1 ppm will be assured.

Bibliography

[1] R. Frisch and O. Stern, *Über die magnetische Ablenkung von Wasserstoffmolekülen und das magnetische Moment des Protons. I*, Zeitschrift für Physik **85** (1933) 4, ISSN: 0044-3328, URL: `https://doi.org/10.1007/BF01330773` (cit. on p. 1).

[2] P. J. Mohr, D. B. Newell and B. N. Taylor, *CODATA recommended values of the fundamental physical constants: 2014*, Rev. Mod. Phys. **88** (3 2016) 035009, URL: `https://link.aps.org/doi/10.1103/RevModPhys.88.035009` (cit. on p. 1).

[3] R. Pohl et al., *The size of the proton*, Nature **466** (2010) 213 EP, URL: `https://doi.org/10.1038/nature09250` (cit. on p. 1).

[4] A. Antognini et al., *Proton Structure from the Measurement of 2S-2P Transition Frequencies of Muonic Hydrogen*, Science **339** (2013) 417, ISSN: 0036-8075, eprint: `https://science.sciencemag.org/content/339/6118/417.full.pdf`, URL: `https://science.sciencemag.org/content/339/6118/417` (cit. on p. 1).

[5] A. Beyer et al., *The Rydberg constant and proton size from atomic hydrogen*, Science **358** (2017) 79 (cit. on p. 1).

[6] H. Fleurbaey et al., *New Measurement of the 1S−3S Transition Frequency of Hydrogen: Contribution to the Proton Charge Radius Puzzle*, Phys. Rev. Lett. **120** (18 2018) 183001, URL: `https://link.aps.org/doi/10.1103/PhysRevLett.120.183001` (cit. on p. 1).

[7] J. J. Krauth et al., *The proton radius puzzle*, arXiv e-prints, arXiv:1706.00696 (2017) arXiv:1706.00696, arXiv: `1706.00696 [physics.atom-ph]` (cit. on p. 1).

[8] A. Antognini et al., "Experiments towards resolving the proton charge radius puzzle", *European Physical Journal Web of Conferences*, vol. 113, European Physical Journal Web of Conferences, 2016 01006, arXiv: `1509.03235 [physics.atom-ph]` (cit. on p. 1).

[9] C. Peng and H. Gao, "Proton Charge Radius (PRad) Experiment at Jefferson Lab", *European Physical Journal Web of Conferences*, vol. 113, 2016 03007 (cit. on p. 1).

[10] R. Gilman et al., *Technical Design Report for the Paul Scherrer Institute Experiment R-12-01.1: Studying the Proton "Radius" Puzzle with μp Elastic Scattering*, arXiv e-prints, arXiv:1709.09753 (2017) arXiv:1709.09753, arXiv: `1709.09753 [physics.ins-det]` (cit. on p. 2).

[11] B. Henderson and Olympus Collaboration, “Results from the OLYMPUS Experiment on the Contribution of Hard Two-Photon Exchange to Elastic Electron-Proton Scattering”, *Proceedings of the XVII International Conference on Hadron Spectroscopy and Structure. 25-29 September*, 2017 149, arXiv: 1712.02274 [nucl-ex] (cit. on p. 2).

[12] A. Vorobyev and A. Denig, *High Precision Measurement of the ep elastic cross section at small Q^2, Proposal to perform an experiment at the A2 hall, MAMI*, (2017) (cit. on p. 2).

[13] B. Adams et al., *Letter of Intent: A New QCD facility at the M2 beam line of the CERN SPS (COMPASS++/AMBER)*, (2018), arXiv: 1808.00848 [hep-ex] (cit. on pp. 2, 50).

[14] B. Adams and C. collaboration, *Proposal for Measurements at the M2 beam line of the CERN SPS, Phase-1: 2022-2024*, Not published, Approximately June 2019 (cit. on pp. 2, 50).

[15] R. J. Rengelink, *A magic wavelength optical dipole trapfor high-precision spectroscopyof ultracold metastable helium*, PhD thesis: VRIJE UNIVERSITEIT, 2018 (cit. on p. 3).

[16] B. Povh et al., *Particles and Nuclei, An Introduction to the Physical Concepts*, 7th ed., Springer Verlag, 2014 (cit. on p. 5).

[17] J. C. Bernauer et al., *High-precision determination of the electric and magnetic form factors of the proton*, Phys. Rev. Lett. **105** (2010) 242001, arXiv: 1007.5076 [nucl-ex] (cit. on p. 6).

[18] P. Abbon et al., *The COMPASS Setup for Physics with Hadron Beams*, Nucl. Instrum. Meth. **A779** (2015) 69, arXiv: 1410.1797 [physics.ins-det] (cit. on p. 8).

[19] H. Kolanski and N. Wermes, *Teilchendetektoren, Grundlagen und Anwendungen*, 1st ed., Springer Verlag, 2016 (cit. on pp. 9, 14).

[20] C. Dreisbach, PhD thesis in progress, Approximately 2020 (cit. on pp. 9–11, 13).

[21] B. M. Veit, internal communication, April 04, 2018, URL: https://twiki.cern.ch/twiki/pub/Compass/ProtonRadius/Meeting20180404/muonp_bt.pdf (cit. on p. 9).

[22] A. Inglessi, personal communication (cit. on pp. 11, 12, 27, 34).

[23] J. Ottnad, *Optimierung der GEM-basierten Verstärkungsstufe einer TPC für das CBELSA/TAPS-Experiment*, PhD thesis in progress, Approximately 2019 (cit. on p. 11).

[24] H. Schindler and R. Veenhof, *Garfield++–simulation of tracking detectors*, 2015 (cit. on p. 11).

[25] *GARFIELD++*, http://garfieldpp.web.cern.ch/garfieldpp/, Last access by Jonathan Ottnad: 2018-09-06 (cit. on p. 11).

[26] S. Biagi, *Magboltz-transport of electrons in gas mixtures*, CERN program library (2011) (cit. on p. 11).

[27] A. Dzyuba, internal communication, July 11, 2018, URL: https://twiki.cern.ch/twiki/pub/Compass/ProtonRadius/Meeting20180711/A.Dzyuba_4COMPASS-2018-07.pdf (cit. on pp. 12, 15, 39).

[28] Christian Dreisbach, *Proton Radius Measurement Test Beam 2018*, COMPASS Weekly Meeting, The simulation was done by Johannes Bernhard, April 20, 2018, URL: https://twiki.cern.ch/twiki/pub/Compass/ProtonRadius/Talks/2018.04.20_-_COMPASS_Weekly_Meeting_-_Proton_Radius_.pdf (cit. on p. 13).

[29] L. Gatignon et al., *Report from the Conventional Beams Working Group to the Physics beyond Colliider Study and to the European Strategy for Particle Physics*, tech. rep. CERN-PBC-REPORT-2018-002, CERN, 2018, URL: https://cds.cern.ch/record/2650989 (cit. on p. 13).

[30] Christian Dreisbach, *Proton Radius Measurement Meeting*, January 23, 2019, URL: https://twiki.cern.ch/twiki/pub/Compass/ProtonRadius/Meeting20190123/2019.01.23_-_COMPASS_Proton_Radius_Meeting.pdf (cit. on p. 13).

[31] M. Tanabashi et al., *Review of Particle Physics*, Phys. Rev. D **98** (3 2018) 030001, URL: https://link.aps.org/doi/10.1103/PhysRevD.98.030001 (cit. on p. 15).

[32] M. J. Berger et al., *(2005) ESTAR, PSTAR, and ASTAR: Computer Programs for Calculating Stopping-Power and Range Tables for Electrons, Protons, and Helium Ions (version 1.2.3).* URL: http://physics.nist.gov/Star%20[2019,01,18] (cit. on pp. 15, 36).

[33] S. Uhl, internal communication, April 25, 2018 (cit. on p. 20).

[34] V. Blobel and C. Kleinwort, *A New Method for the High-Precision Alignment of Track Detectors*, arXiv e-prints, hep-ex/0208021 (2002) hep, arXiv: hep-ex/0208021 [hep-ex] (cit. on p. 22).

[35] P. Abbon et al., *The COMPASS experiment at CERN*, Nuclear Instruments and Methods in Physics Research Section A: Accelerators, Spectrometers, Detectors and Associated Equipment **577** (2007) 455, ISSN: 0168-9002, URL: http://www.sciencedirect.com/science/article/pii/S0168900207005001 (cit. on p. 22).

[36] K. Eichhorn, internal communication, January 23, 2019, URL: https://twiki.cern.ch/twiki/bin/view/Compass/ProtonRadius/Meeting20190123 (cit. on p. 22).

[37] M. R. Mynter, *Performanz-Untersuchung von Silizium-Mikrostreifendetektoren im COMPASS Experiment am CERN*, September 03, 2018, Bachelor's Thesis (cit. on p. 22).

[38] S. Neumaier et al., *Small-angle proton elastic scattering from the neutron-rich isotopes 6He and 8He, and from 4He, at 0.7 GeV in inverse kinematics*, Nuclear Physics A **712** (2002) 247, ISSN: 0375-9474, URL: http://www.sciencedirect.com/science/article/pii/S0375947402012745 (cit. on p. 27).

[39] F. Sauli, *Gaseous Radiation Detectors*, Camb. Monogr. Part. Phys. Nucl. Phys. Cosmol. **36** (2014) pp.1 (cit. on p. 27).

[40] W. R. Leo, *Techniques for Nuclear and Particle Physics Experiments, A How-to Approach*, 2nd ed., Springer Verlag, 1994 (cit. on p. 33).

[41] S. Agostinelli et al., *Geant4—a simulation toolkit*, Nuclear Instruments and Methods in Physics Research Section A: Accelerators, Spectrometers, Detectors and Associated Equipment **506** (2003) 250, ISSN: 0168-9002, URL: `http://www.sciencedirect.com/science/article/pii/S0168900203013688` (cit. on p. 39).

[42] J. Allison et al., *Recent developments in Geant4*, Nuclear Instruments and Methods in Physics Research Section A: Accelerators, Spectrometers, Detectors and Associated Equipment **835** (2016) 186, ISSN: 0168-9002, URL: `http://www.sciencedirect.com/science/article/pii/S0168900216306957` (cit. on p. 39).

[43] T. Kunz, *Entwicklung einer Simulationsumgebung für das COMPASS-II-Experiment mit Geant4*, PhD thesis: Freiburg U., 2012, URL: `http://wwwhad.physik.uni-freiburg.de/arbeiten/diplomarbeiten/kunz_tobias_diplom.pdf` (cit. on p. 39).

[44] I. Hřivnáčová and B. Viren, *The virtual geometry model*, Journal of Physics: Conference Series **119** (2008) 042016, URL: `https://doi.org/10.1088%2F1742-6596%2F119%2F4%2F042016` (cit. on p. 41).

[45] K. Eichhorn, *Performance of Silicon Microstrip Detectors in the Proton Radius Test Measurement at COMPASS*, Bachelor's Thesis in progress, Approximately May 2019 (cit. on p. 41).

APPENDIX A

Own contributions

- Participation in the data taking of the test experiment.
- Setting the high-voltages of the silicon tracking stations, which are required in order to reduce noise.
- GEM expert-on-call for the COMPASS experiment
- Analysis of the data, as presented in this thesis:
  - Run-by-run alignment
  - Extracted z-vertex resolution
  - Calculated kinetic energy of the recoil proton using the scattering angle
  - Time-dependent TPC calibration
  - TPC tracking algorithm
  - Improved signal-to-noise ratio of the time difference peak
  - Extracted drift velocity
  - Correlation of energy and direction of the recoil proton
- Monte Carlo simulation of the setup, as presented in this thesis:
  - Improved the implementation of the experimental setup in Geant4
  - Implemented a generator for scattering angles following the Rosenbluth formula
  - Full analysis of the generated events

APPENDIX B

Calculation of the kinetic energy and the corresponding error

In this chapter, the resolution of the scattering is estimated. Furthermore, the kinetic energy T_p of the recoil proton is calculated with the scattering angle θ. The uncertainty of the kinetic energy due to the uncertainty of the scattering angle and the beam momentum is given.

B.1 Resolution of θ

Using the resolution of the z-position of the vertex one can calculate an upper limit for the resolution of θ and the kinetic energy using a simple model, see figure B.1. The effect of the incoming beam slope on the uncertainty is neglected, which overestimates the uncertainty, and the small-angle approximation is used. Additionally, this model parametrises the scattering process only in one transversal dimension instead of two. The resulting resolution is given in equation (B.1).

$$\theta = \arctan\left(\frac{l}{z_4 - z}\right), \quad \Delta\theta = \theta\frac{\Delta z}{z_4 - z} \tag{B.1}$$

B.2 Calculation of the kinetic energy

For a fixed target experiment with a muon beam and a proton target, the invariant mass s is given by:

$$s = m_\mu^2 + m_p^2 + 2m_p E_\mu$$

with m_μ the muon mass; m_p the proton mass and E_μ the energy of the incoming muon beam.

The energy E'_μ and momentum p'_μ of the scattered muon can be calculated in the centre of mass frame:

$$E'_{\mu,\mathrm{CM}} = \frac{s + m_\mu^2 - m_p^2}{2\sqrt{s}} \quad .$$

The momentum of the scattered muon parallel to the z-axis in the centre of mass frame $p'_{\mu,\mathrm{CM},||}$ can be calculated with the scattering angle in this frame θ_{CM}:

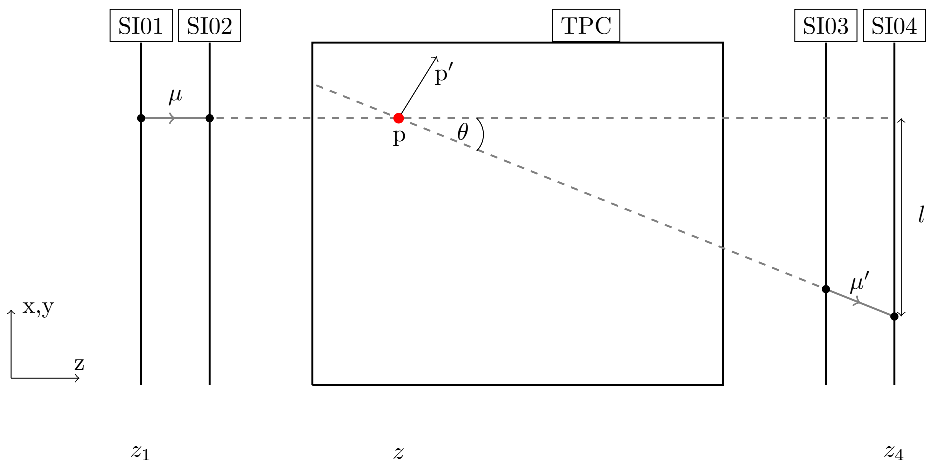

Figure B.1: This sketch shows the model to estimate the uncertainty of θ with the z-vertex resolution.

$$p'_{\mu,\mathrm{CM},||} = p'_{\mu,\mathrm{CM}} \cdot \cos(\theta_{\mathrm{CM}}) = \sqrt{E'^2_{\mu,\mathrm{CM}} - m^2_\mu} \cdot \cos(\theta_{\mathrm{CM}}) \ .$$

From the centre of mass energy one can boost into the lab frame with the lorentz factors:

$$\gamma = \frac{E_\mu + m_p}{\sqrt{s}} \ ,$$

which gives the energy and momentum of the scattered muon in the lab frame:

$$E'_{\mu,\mathrm{lab}} = \gamma \cdot E'_{\mu,\mathrm{CM}} + \sqrt{\gamma^2 - 1} \cdot p'_{\mu,CM,||}$$

$$p'_{\mu,\mathrm{lab},||} = \sqrt{\gamma^2 - 1} \cdot E'_{\mu,\mathrm{CM}} + \gamma \cdot p'_{\mu,CM,||}$$

The energy of the recoil proton E'_p is given by the energy conservation:

$$E'_p = m_p + T'_p = E_\mu + E_p - E'_\mu \ .$$

With the initial proton being at rest, the kinetic energy T'_p is:

$$T'_p = E_\mu - E'_\mu = E_\mu - \left(\gamma \cdot E'_{\mu,\mathrm{CM}} + \sqrt{\gamma^2 - 1} \cdot p'_{\mu,CM,||}\right) \ .$$

The scattering angle in the lab frame θ_{lab} depends on the scattering angle in the centre of mass frame:

$$\theta_{\mathrm{lab}} = \arctan\left(\frac{p'_{\mu,\mathrm{lab},\perp}}{p'_{\mu,\mathrm{lab},||}}\right) = \arctan\left(\frac{p'_{\mu,\mathrm{CM}} \sin(\theta_{\mathrm{CM}})}{p'_{\mu,\mathrm{lab},||}}\right) \ .$$

With the following substitutions and $\theta = \theta_{\mathrm{lab}}$:

$$a = E_\mu + m_\mathrm{p} \ , \quad b = m_\mu^2 \ , \quad c = m_\mathrm{p}^2 + p_\mu^2 \ , \quad d = 2p_\mu \cos(\theta)$$

the momentum of the scattered muon can be calculated:

$$p'_\mu = \frac{a^2 d + 2\sqrt{a^6 - 2a^4(b+c) + a^2b^2 - 2a^2bc + a^2bd^2 + a^2c^2} + bd - cd}{4a^2 - d^2} = \frac{f}{g} \ . \tag{B.2}$$

Using this formula, the kinetic energy of the recoil proton can be calculated:

$$T'_p = E_\mu - E'_\mu = E_\mu - \sqrt{p'^2_\mu + m_\mu^2} \ . \tag{B.3}$$

B.3 Uncertainty of the recoil proton kinetic energy

The uncertainty of the recoil proton momentum originates from the uncertainty on the muon beam momentum, which was not measured, and the scattering angle.

First, the dependence on the scattering angle is given. As the kinetic energy of the beam does not depend on the scattering angle, only the kinetic energy of the scattered muon contributes to this uncertainty:

$$T'_\mu = E'_\mu - m_\mu = \sqrt{\left(m_\mu^2 + p'^2_\mu\right)} - m_\mu$$

$$\frac{dT'_\mu}{d\theta} = \frac{p'_\mu}{E'_\mu}\frac{dp'_\mu}{d\theta}$$

In equation (B.2), only the variable d depends on the scattering angle:

$$\frac{\delta p'_\mu}{\delta\theta} = \frac{\partial p'_\mu}{\partial d}\frac{\partial d}{\partial\theta} = g^{-2}\left(\frac{\partial f}{\partial d}g - \frac{\partial g}{\partial d}f\right) \cdot (-2p\mu\sin(\theta))$$

with

$$\frac{\partial f}{\partial d} = a^2 + \frac{2a^2bd}{\sqrt{a^6 - 2a^4(b+c) + a^2b^2 - 2a^2bc + a^2bd^2 + a^2c^2}} + b - c$$

and

$$\frac{\partial g}{\partial d} = -2 \cdot d \ .$$

This gives the uncertainty on the kinetic energy of the recoil proton due to the uncertainty of the scattering angle:

$$\Delta T_{\mathrm{p},\theta} = \Delta T'_\mu = \frac{p'_\mu}{E'_\mu}\frac{\partial p'_\mu}{\partial d}\left(-2p_\mu\sin(\theta)\right)\Delta\theta \ .$$

Then the dependence on the muon momentum is derived. In equation (B.2), the variables a, c and d depend on the beam momentum or energy. Therefore, the variables are inserted and the equation is simplified as much as possible. This gives the following result:

$$p'_\mu = \frac{\cos(\theta) \cdot \left(4E_\mu m_p p_\mu + 4m_\mu^2 p_\mu + 2h\right)}{4E_\mu^2 + 8E_\mu m_p + 4m_p^2 - 4p_\mu^2 \cos^2(\theta)} = \frac{f}{g}$$

with

$$\begin{aligned} h = \Big[& -2E_\mu^5 m_p + 3E_\mu^4 m_p^2 + 8E_\mu^3 m_p^3 - 4E_\mu^3 m_p m_\mu^2 - 6E_\mu^2 m_p^2 m_\mu^2 + 4E_\mu^2 m_p^4 \\ & -4E_\mu^2 m_\mu^2 p_\mu^2 + E_\mu^2 m_\mu^2 p_\mu^2 \cos^2(\theta) - 8E_\mu m_p^3 m_\mu^2 + 6E_\mu m_p m_\mu^4 + 2E_\mu m_p p_\mu^4 \\ & +8E_\mu m_p m_\mu^2 p_\mu^2 \cos^2(\theta) + 3m_p^2 m_\mu^4 - 4m_p^4 m_\mu^2 + m_p^2 p_\mu^4 + 4m_p^2 m_\mu^2 p_\mu^2 \cos^2(\theta)\Big]^{0.5} \quad . \end{aligned}$$

Deriving the momentum of the scattered muon after the beam momentum yields:

$$\frac{\partial p'_\mu}{\partial p_\mu} = \frac{\frac{\partial f}{\partial p_\mu} g + f \frac{\partial g}{\partial p_\mu}}{g^2}$$

with

$$\frac{\partial g}{\partial p_\mu} = 8p_\mu + 8m_p \frac{p_\mu}{E_\mu} - 8p_\mu \cos^2(\theta) \ ,$$

$$\frac{\partial f}{\partial p_\mu} = \cos(\theta) \left(\frac{4m_p p_\mu^2}{E_\mu} + 4E_\mu m_p + 4m_\mu^2 \right) + 2\frac{\partial h}{\partial p_\mu}$$

and

$$\begin{aligned} \frac{\partial h}{\partial p_\mu} = \frac{1}{2h} \Big[& -10E_\mu^3 p_\mu m_p + 12E_\mu^2 p_\mu m_p^2 + 24E_\mu p_\mu m_p^3 - 12E_\mu p_\mu m_p m_\mu^2 - 12p_\mu m_p^2 m_\mu^2 + 8p_\mu m_p^4 \\ & -8p_\mu^3 m_\mu^2 - 8E_\mu^2 m_\mu^2 p_\mu + 8p_\mu^3 m_\mu^2 \cos^2(\theta) + 8E_\mu^2 m_\mu^2 p_\mu \cos^2(\theta) - 8\frac{p_\mu}{E_\mu} m_p^3 m_\mu^2 \\ & +6\frac{p_\mu}{E_\mu} m_p m_\mu^4 + 2\frac{p_\mu^5}{E_\mu} m_p + 8E_\mu m_p p\mu^3 + 8\frac{p_\mu^3}{E_\mu} m_p m_\mu^2 \cos^2(\theta) + 16E_\mu m_p m_\mu^2 p_\mu \cos^2(\theta) \\ & +4m_p^2 p_\mu^3 + 8m_p^2 m_\mu^2 p_\mu \cos^2(\theta)\Big] \quad . \end{aligned}$$

The uncertainty on the kinetic energy of the proton due to the uncertainty of the beam momentum can be calculated with:

$$\Delta T_{\mathrm{p},p_\mu} = \frac{\partial T_p}{\partial p_\mu} \Delta p_\mu = \left(\frac{p_\mu}{E_\mu} - \frac{p'_\mu}{E'_\mu} \frac{\partial p'_\mu}{\partial p_\mu} \right) \Delta p_\mu$$

The combined uncertainty is then given with Gaussian error propagation assuming no correlation on the errors:

$$\Delta T_p = \sqrt{\left(\Delta T_{\mathrm{p},p_\mu}\right)^2 + \left(\Delta T_{\mathrm{p},\theta}\right)^2} \ . \tag{B.4}$$

APPENDIX C

Additional figures for the analysis

C.1 Radial cuts

Figure C.1 shows the xy-distribution of the incoming beam at the downstream endcap and the distribution at the cathode position is depicted in figure C.2.

C.2 Alignment and residuals

The changes in the y-position of SI04V are plotted in figure C.3.

The residuals of SI04X are drawn in figure C.4. The residuals are not centred around 0, which might be caused by a wrong determination of the pitch or the angle between the planes.

C.3 Matched events

The φ-distribution of all recoil protons that are matched with the TPC is drawn in figure C.5. The distribution is flat.

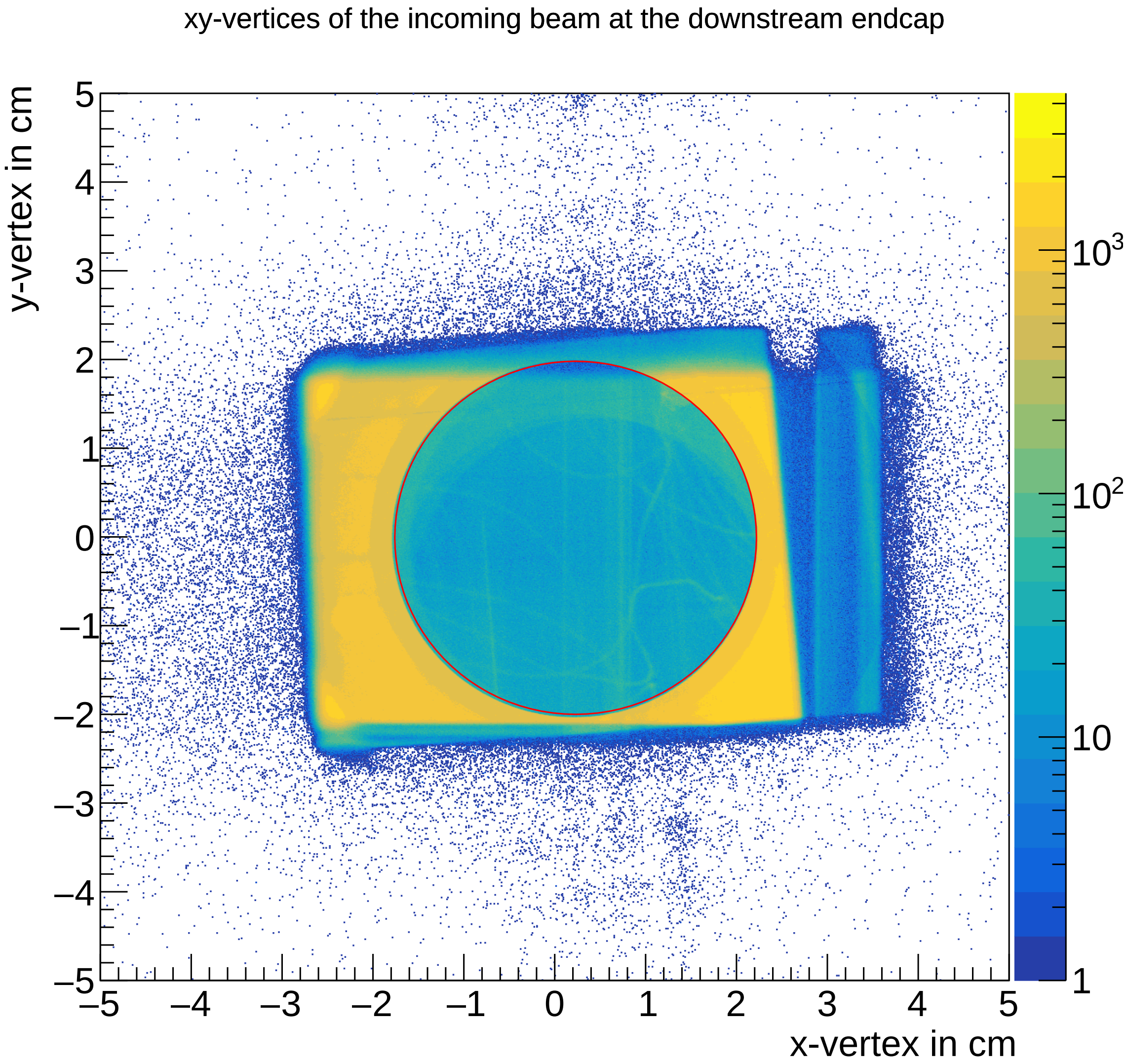

Figure C.1: The xy-vertices of the incoming beam at the position of the downstream end cap. The number of events is shown with the colour scheme. The red circle indicates the applied radial cut.

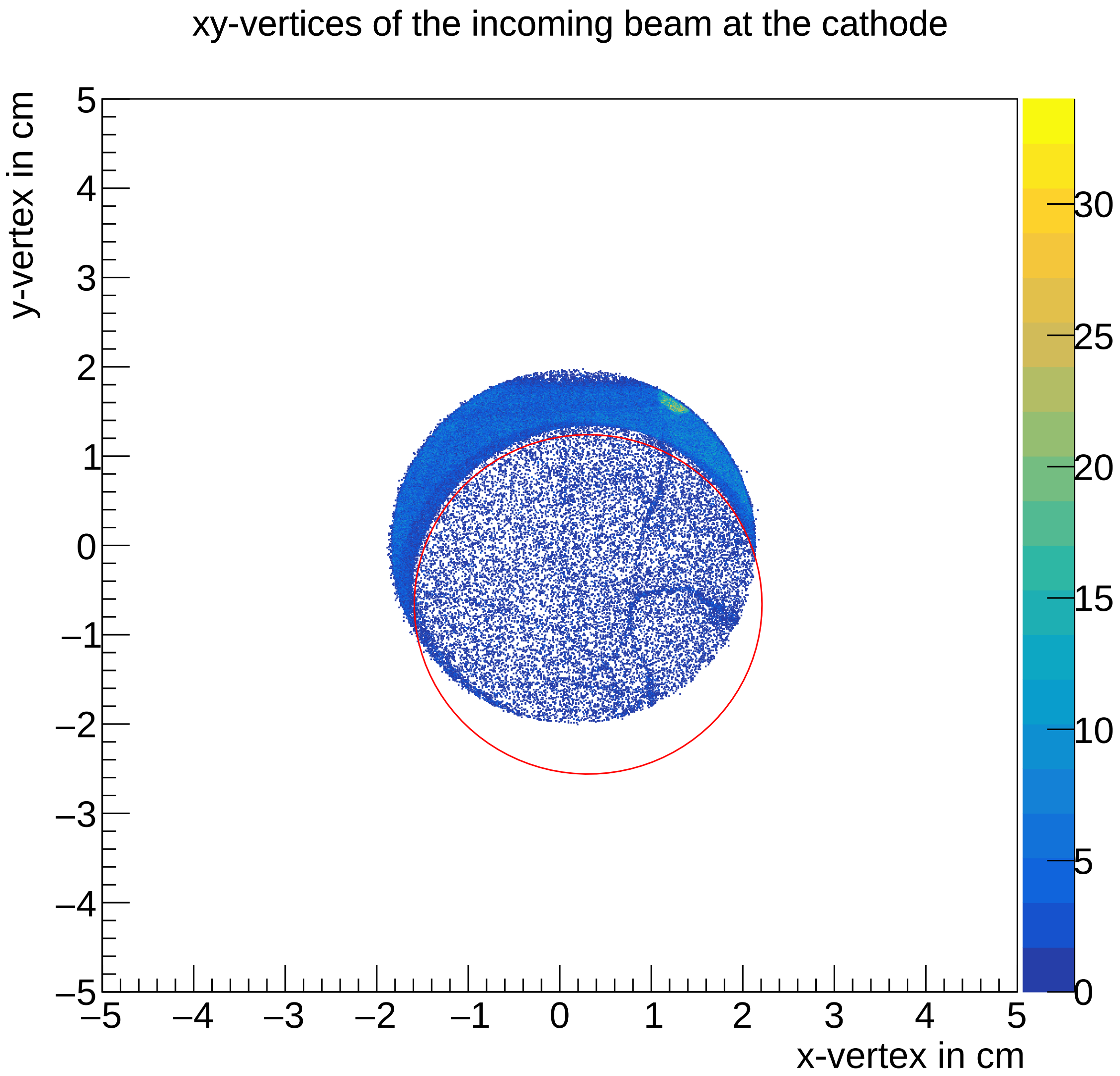

Figure C.2: The xy-vertices of the incoming beam at the position of the cathode. The number of events is shown with the colour scheme. The red circle indicates the applied radial cut.

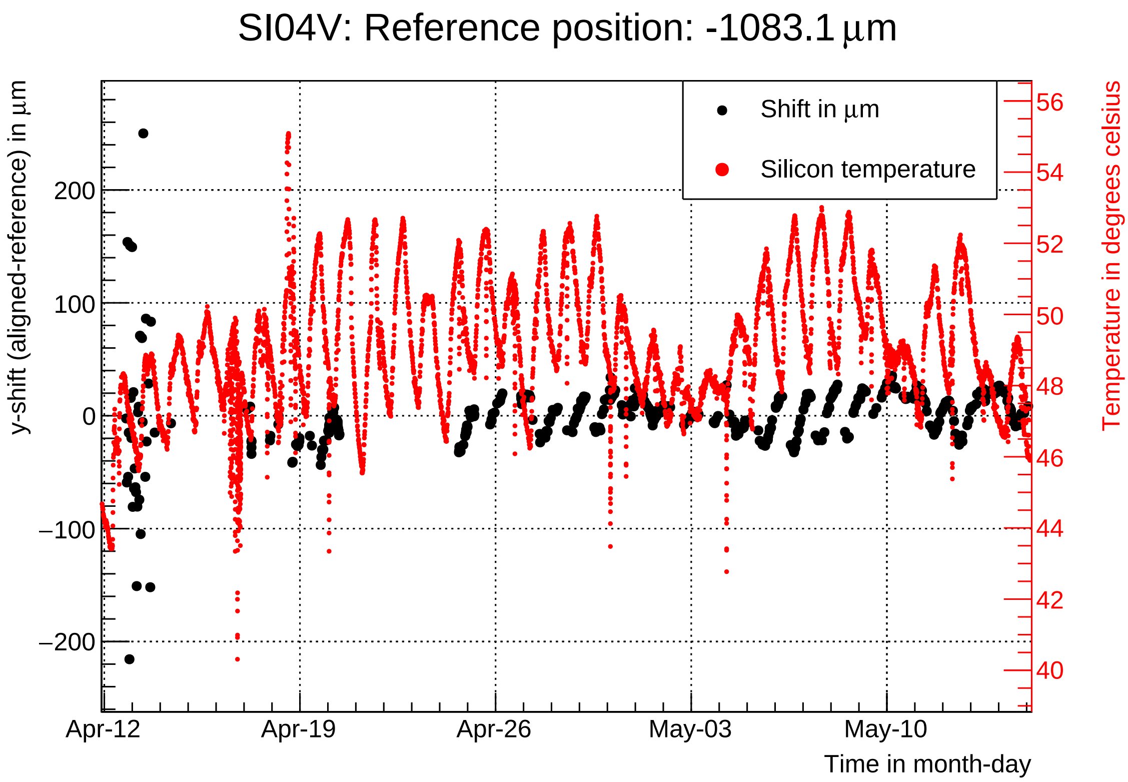

Figure C.3: The shift in the y-position of the SI04V-plane (black) and the temperature measured by the silicon station (red) is drawn for the whole measurement. There is no large overall shift but daily fluctuations, which follow the measured temperatures.

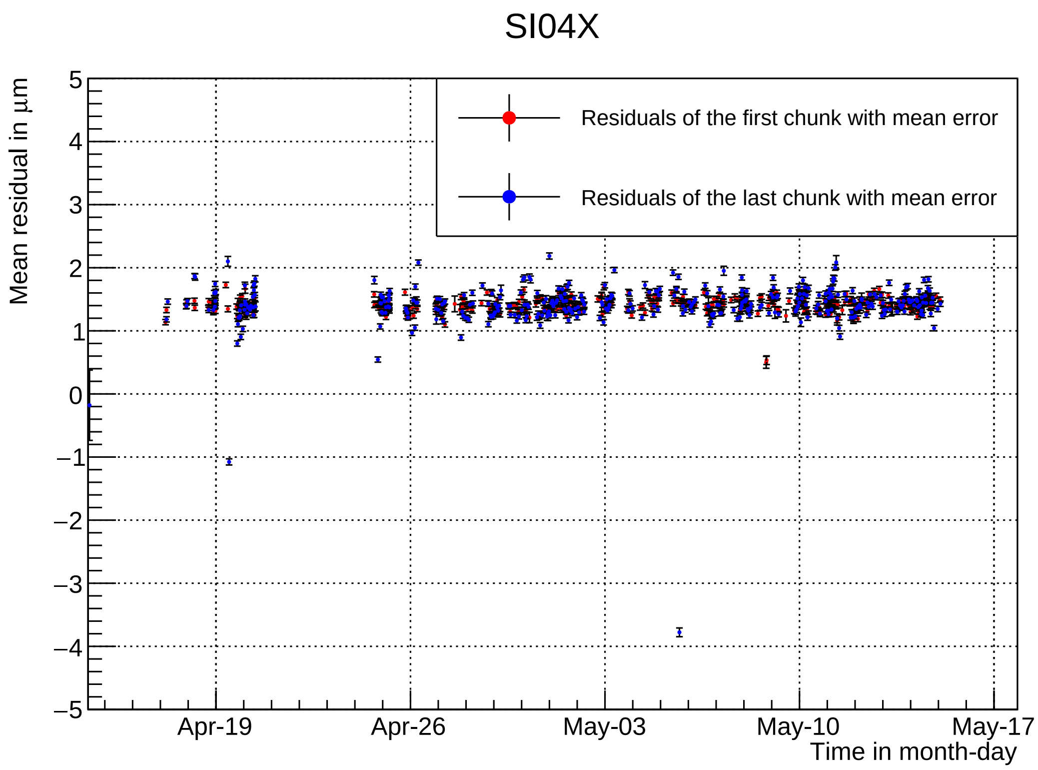

Figure C.4: The residuals measured from the second 100k events of the first chunk (red) and the first 100k events of the last chunk (blue) of each run. The residuals are constant with time but not centred at 0. This might originate from a wrong determination of the pitch or the rotation angle between the XY- and UV-planes. The blue points have larger variations due to a detector movement over time. Only chunks with more than 1,000 events and a reduced χ^2 of less than 10 are plotted.

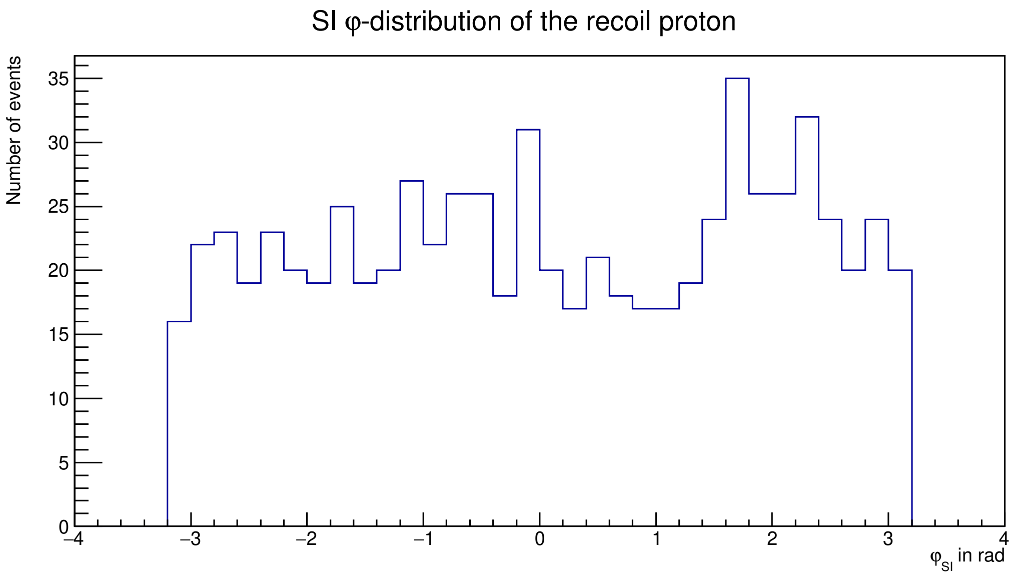

Figure C.5: The φ-distribution measured by the silicon tracking stations for all events that are matched with the TPC. The distribution is nearly flat.

APPENDIX D

High-voltage scan of the silicon trackers

The rate of the silicon trackers is measured with increasing high voltage. The high voltage is set to the minimal value, at which the noise level saturates.

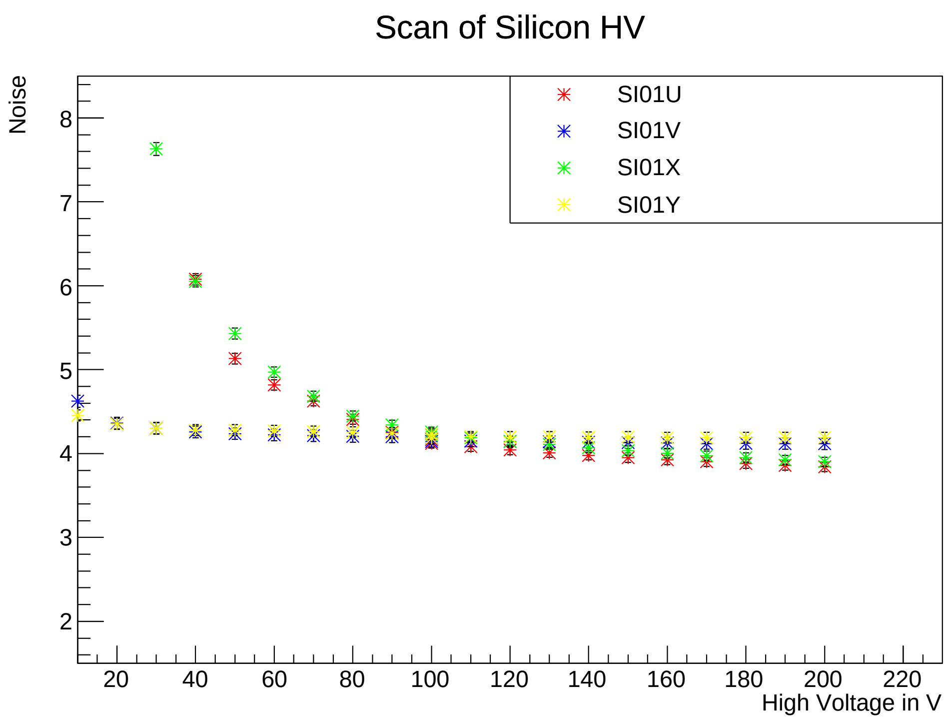

Figure D.1: The high voltage scan of silicon station SI01. The noise level is given in arbitrary units. The voltage has been set to 100 V.

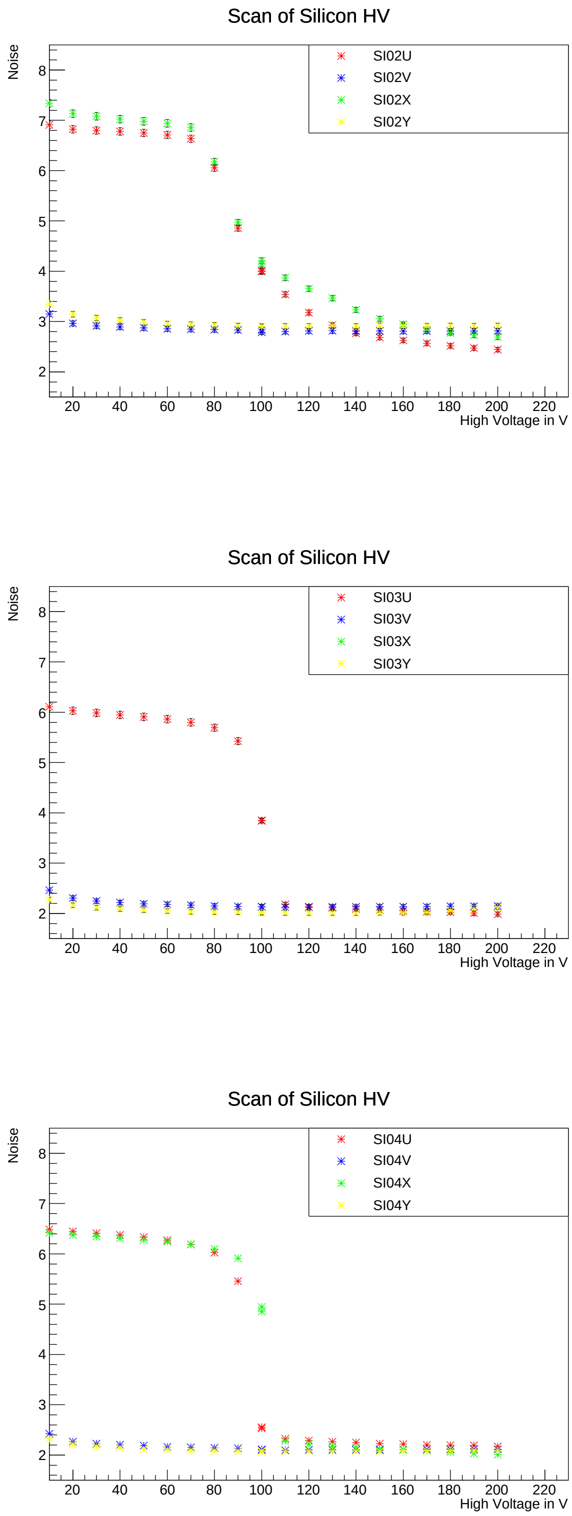

Figure D.2: The high voltage scan of silicon stations SI02 (top), SI03 (middle) and SI04 (bottom). The noise level is given in arbitrary units. The voltage of SI02 has been set to 170 V, the voltage of SI03 has been set to 120 V and the voltage of SI04 has been set to 120 V.

APPENDIX E

Fits of the z-resolution

The fits of the z-vertex distribution for all θ-bins are shown in this section.

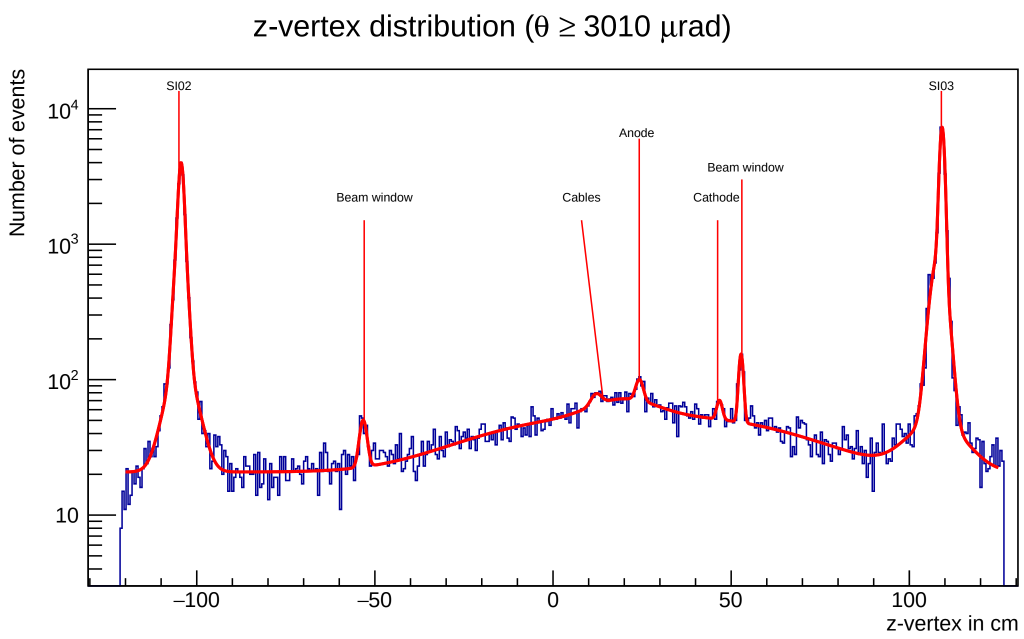

Figure E.1: The figure shows the distribution of the z-vertex with $\theta \geq 3.010$ mrad for the run-by-run alignment (χ^2/dof=847.754/395).

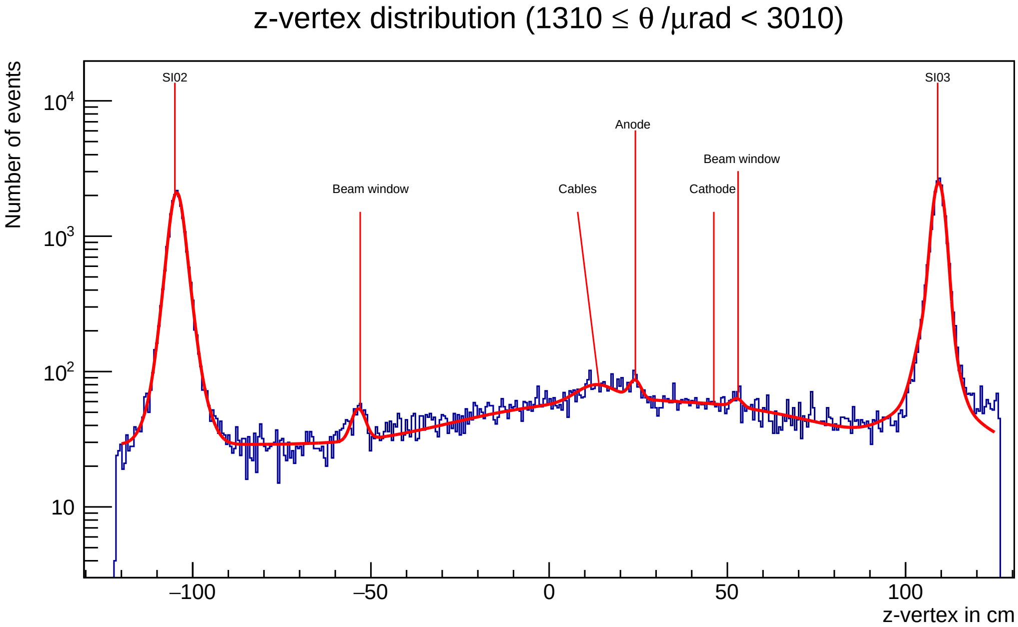

Figure E.2: The figure shows the distribution of the z-vertex with $1.310 \leq \theta/\text{mrad} < 3.010$ for the run-by-run alignment (χ^2/dof=721.085/395).

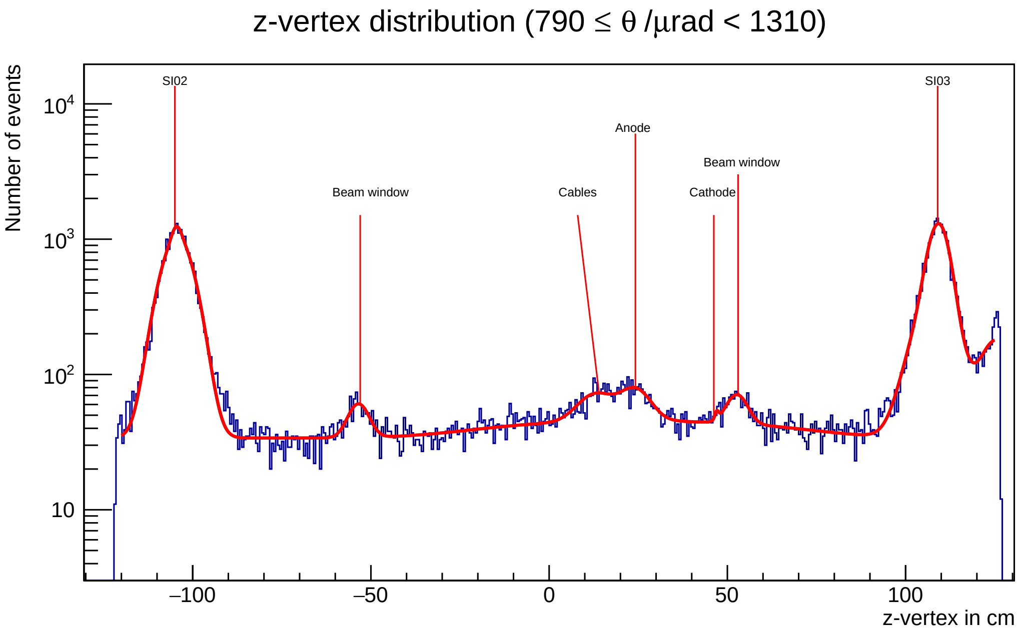

Figure E.3: The figure shows the distribution of the z-vertex with $0.790 \leq \theta/\text{mrad} < 1.310$ for the run-by-run alignment (χ^2/dof=877.684/392).

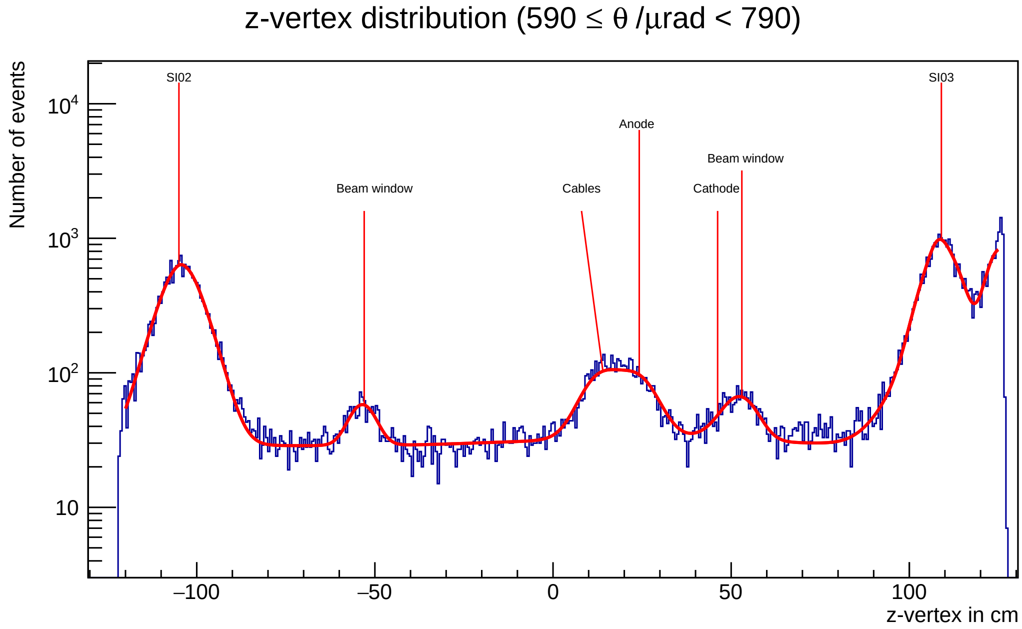

Figure E.4: The figure shows the distribution of the z-vertex with $0.590 \leq \theta/\mathrm{mrad} < 0.790$ for the run-by-run alignment (χ^2/dof=1043.25/392).

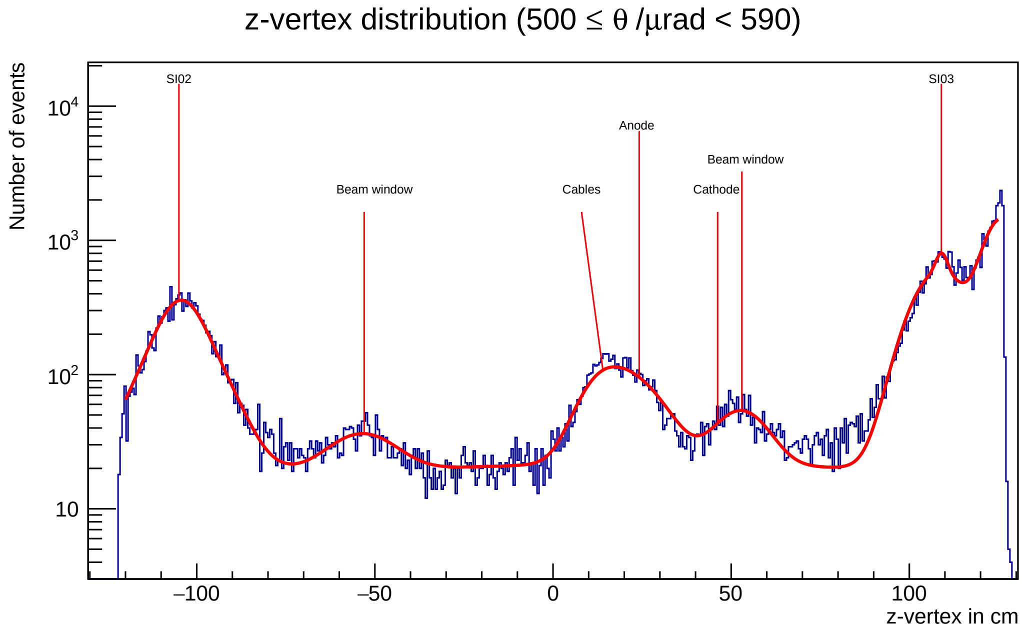

Figure E.5: The figure shows the distribution of the z-vertex with $0.500 \leq \theta/\mathrm{mrad} < 0.590$ for the run-by-run alignment (χ^2/dof=1688.35/392).

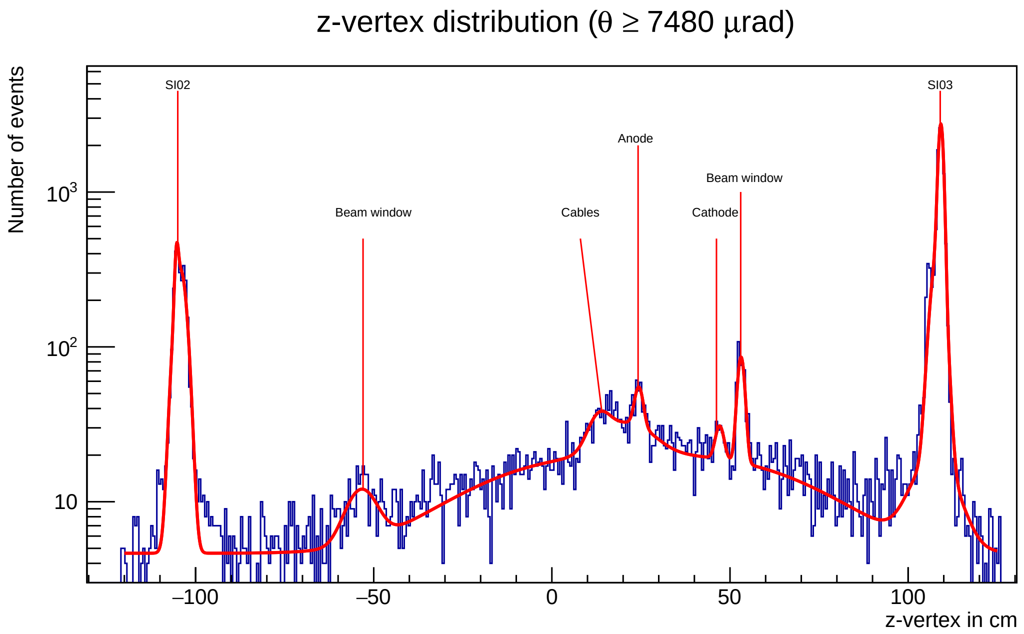

Figure E.6: The figure shows the distribution of the z-vertex with $\theta \geq 7.480$ mrad for the preliminary alignment (χ^2/dof=1105.46/394).

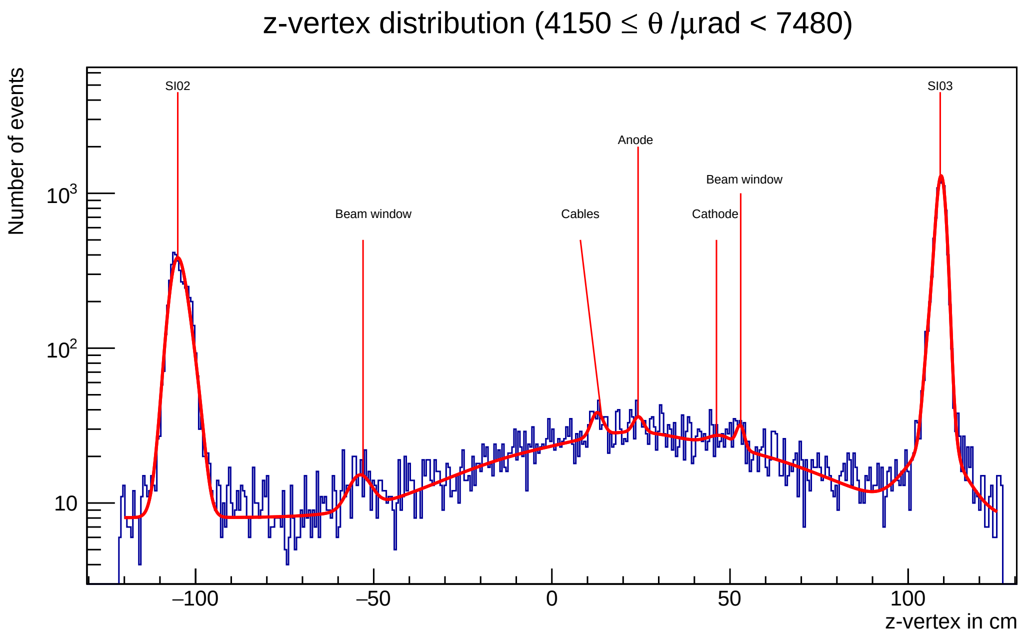

Figure E.7: The figure shows the distribution of the z-vertex with $4.150 \leq \theta/\mathrm{mrad} < 7.480$ for the preliminary alignment (χ^2/dof=600.259/395).

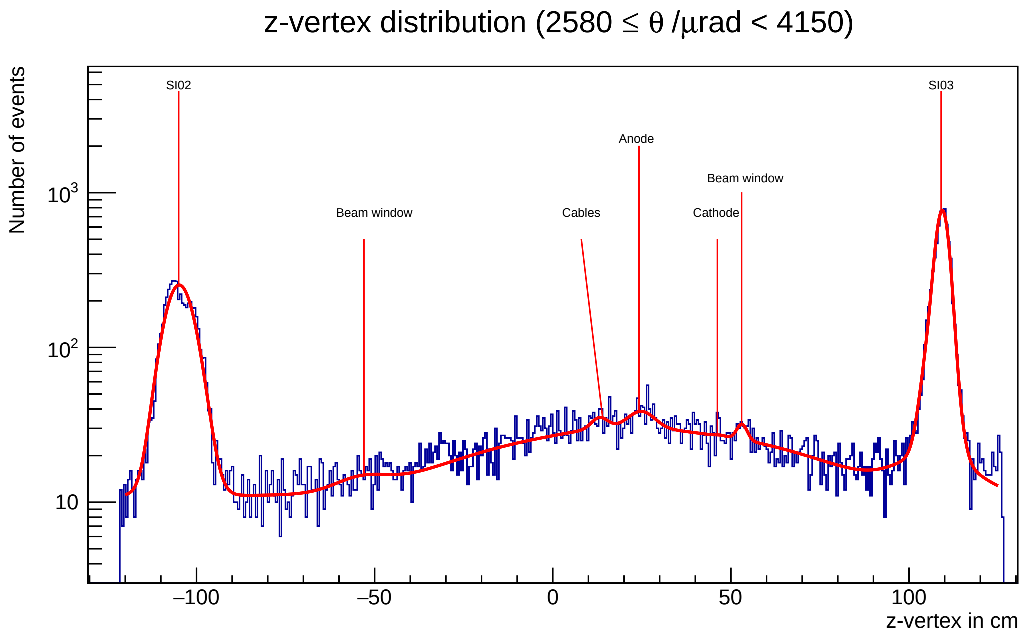

Figure E.8: The figure shows the distribution of the z-vertex with $2.580 \leq \theta/\mathrm{mrad} < 4.150$ for the preliminary alignment (χ^2/dof=577.88/395).

APPENDIX F

Fit Parameters for the MC resolution studies

Events were simulated with fixed scattering angles at the position of the anode and the cathode. The results of fits with two Gaussian distributions to the z-vertex distribution are given in table F.1. The θ-distribution can be fitted as well. Here, the reconstruction of events in the anode and the cathode is separated. The results are given in table F.2.

The same procedure is done for the studies with a 2 m longer distance between the first and last silicon tracking station. The results are given in tables F.3 and F.4.

θ_{MC}/mrad	a_{Anode}	$z_{0,Anode}$/cm	σ_{Anode}/cm	$a_{Cathode}$	$z_{0,Cathode}$/cm	$\sigma_{Cathode}$/cm	χ^2/dof
0.5	25.4 ± 0.6	24.8 ± 0.4	8.55 ± 0.23	17.7 ± 0.5	47.2 ± 0.6	8.7 ± 0.4	1550/713
0.75	37.5 ± 0.7	24.3 ± 0.1	5.39 ± 0.08	29.8 ± 0.7	46.11 ± 0.12	5.94 ± 0.11	1388/571
1.0	53 ± 1	24.36 ± 0.06	3.98 ± 0.05	40.4 ± 0.8	46.87 ± 0.07	4.27 ± 0.06	1297/488
1.5	76.8 ± 1.4	24.27 ± 0.04	2.72 ± 0.03	67.4 ± 1.3	46.91 ± 0.05	2.80 ± 0.04	867/368
2.0	106.2 ± 1.9	24.31 ± 0.028	2.005 ± 0.022	87.8 ± 1.6	46.76 ± 0.04	2.177 ± 0.024	627/286
2.5	132.4 ± 2.3	24.332 ± 0.023	1.613 ± 0.017	115.7 ± 2.1	46.796 ± 0.025	1.685 ± 0.019	467/231
3.0	152.1 ± 2.6	24.280 ± 0.019	1.363 ± 0.014	134.5 ± 2.4	46.768 ± 0.021	1.446 ± 0.016	535/201
3.5	181 ± 4	24.297 ± 0.016	1.149 ± 0.012	150.6 ± 2.7	46.804 ± 0.019	1.290 ± 0.014	393/177
5.0	245 ± 5	24.298 ± 0.012	0.810 ± 0.009	219 ± 4	46.808 ± 0.013	0.86 ± 0.01	255/133
10.0	353 ± 8	24.295 ± 0.007	0.420 ± 0.006	320 ± 7	46.798 ± 0.008	0.441 ± 0.006	77/61
15.0	256 ± 8	24.293 ± 0.007	0.274 ± 0.005	228 ± 7	46.793 ± 0.008	0.294 ± 0.005	58/39
20.0	74 ± 5	24.292 ± 0.011	0.206 ± 0.008	70 ± 5	46.814 ± 0.012	0.22 ± 0.01	14.1/20

Table F.1: The amplitude a, position z_0 and width σ of a fit with a Gaussian distribution to the z-vertex distribution of Monte Carlo simulated data with a generated scattering angle of θ_{MC}.

θ_{MC}/mrad	Anode/Cathode	a	θ_0/mrad	σ_θ/mrad	χ^2/dof
0.5	Anode	908 ± 16	0.5058 ± 0.0004	0.02396 ± 0.00028	595/24
0.5	Cathode	770 ± 15	0.4954 ± 0.0004	0.02228 ± 0.00028	282/23
0.75	Anode	850 ± 16	0.7517 ± 0.0004	0.0259 ± 0.0003	280/23
0.75	Cathode	778 ± 15	0.7497 ± 0.0004	0.0243 ± 0.0004	313/23
1.0	Anode	920 ± 17	1.0001 ± 0.0004	0.0239 ± 0.0003	254/25
1.0	Cathode	803 ± 16	1.0003 ± 0.0004	0.0245 ± 0.0004	208/26
1.5	Anode	867 ± 16	1.5007 ± 0.0004	0.0246 ± 0.0003	190/30
1.5	Cathode	814 ± 16	1.5000 ± 0.0004	0.0247 ± 0.0004	217/26
2.0	Anode	860 ± 16	2.0006 ± 0.0004	0.0249 ± 0.0003	220/31
2.0	Cathode	787 ± 16	1.9997 ± 0.0004	0.0249 ± 0.0004	221/28
2.5	Anode	909 ± 17	2.5000 ± 0.0004	0.02313 ± 0.00029	278/30
2.5	Cathode	811 ± 16	2.5002 ± 0.0004	0.0241 ± 0.0004	248/28
3.0	Anode	825 ± 16	3.0000 ± 0.0004	0.0252 ± 0.0004	232/26
3.0	Cathode	796 ± 15	3.0003 ± 0.0004	0.0249 ± 0.0004	180/26
3.5	Anode	833 ± 16	3.5001 ± 0.0004	0.0249 ± 0.0003	194/29
3.5	Cathode	752 ± 15	3.5002 ± 0.0004	0.0260 ± 0.0004	169/30
5.0	Anode	795 ± 16	5.0012 ± 0.0004	0.0245 ± 0.0004	200/33
5.0	Cathode	744 ± 15	5.0004 ± 0.0004	0.0250 ± 0.0004	214/33
10.0	Anode	554 ± 13	10.0003 ± 0.0005	0.0260 ± 0.0005	130/25
10.0	Cathode	538 ± 13	10.0001 ± 0.0005	0.0255 ± 0.0004	143/27
15.0	Anode	274 ± 9	14.9999 ± 0.0006	0.0251 ± 0.0005	63/26
15.0	Cathode	252 ± 9	15.0000 ± 0.0007	0.0258 ± 0.0007	76/24
20.0	Anode	64 ± 5	20.0014 ± 0.0013	0.0227 ± 0.0009	19/14
20.0	Cathode	63 ± 5	19.9989 ± 0.0013	0.0240 ± 0.0012	18/19

Table F.2: The amplitude a, position θ_0 and width σ_θ of a fit with a Gaussian distribution to the θ-distribution of Monte Carlo simulated data with a generated scattering angle of θ_{MC}. The data of scattering processes at the anode and at the cathode are separated.

θ_{MC}/mrad	Anode/Cathode	a	z_0/cm	σ/cm	χ^2/dof
0.5	Anode	30.9 ± 0.7	24.50 ± 0.11	5.6 ± 0.1	
	Cathode	28.6 ± 0.7	46.62 ± 0.11	5.6 ± 0.1	1420/554
1.0	Anode	65.4 ± 1.3	24.30 ± 0.05	2.73 ± 0.04	
	Cathode	62.5 ± 1.2	46.78 ± 0.05	2.85 ± 0.04	706/355
1.5	Anode	99.4 ± 1.8	24.29 ± 0.03	1.867 ± 0.021	
	Cathode	98.5 ± 1.8	46.7987 ± 0.017	1.907 ± 0.022	407/242
2.0	Anode	133 ± 3	24.305 ± 0.021	1.379 ± 0.016	
	Cathode	128.6 ± 2.4	46.782 ± 0.022	1.449 ± 0.017	313/182
2.5	Anode	168 ± 3	24.312 ± 0.017	1.114 ± 0.012	
	Cathode	161.6 ± 2.9	46.781 ± 0.017	1.148 ± 0.012	208/155
3.0	Anode	194 ± 4	24.292 ± 0.014	0.93 ± 0.01	
	Cathode	193 ± 4	46.817 ± 0.014	0.95 ± 0.01	188/129

Table F.3: The amplitude a, position z_0 and width σ of a fit with a Gaussian distribution to the z-vertex distribution of Monte Carlo simulated data with a generated scattering angle of θ_{MC} and a 2 m larger distance between the first and the last silicon tracking station.

θ_{MC}/mrad	Anode/Cathode	a	θ_0/mrad	σ_θ/mrad	χ^2/dof
0.5	Anode	1247 ± 24	0.50089 ± 0.00023	0.0158 ± 0.0002	119.3/17
0.5	Cathode	1208 ± 25	0.49961 ± 0.00023	0.01519 ± 0.00021	109.8/15
1.0	Anode	1186 ± 23	0.99990 ± 0.00024	0.0160 ± 0.0002	60.4/13
1.0	Cathode	1189 ± 23	0.99992 ± 0.00024	0.01598 ± 0.00021	59.9/13
1.5	Anode	1201 ± 24	1.49993 ± 0.00023	0.01580 ± 0.00021	64.8/14
1.5	Cathode	1233 ± 25	1.49986 ± 0.00023	0.01559 ± 0.00021	102.7/17
2.0	Anode	1189 ± 24	1.99994 ± 0.00023	0.0156 ± 0.0002	57.9/15
2.0	Cathode	1209 ± 24	2.00068 ± 0.00023	0.01563 ± 0.00021	86.7/15
2.5	Anode	1190 ± 24	2.49960 ± 0.00024	0.01581 ± 0.00021	83.4/16
2.5	Cathode	1161 ± 23	2.49977 ± 0.00024	0.01618 ± 0.00021	51.4/15
3.0	Anode	1126 ± 22	3.00026 ± 0.00024	0.01604 ± 0.00021	55.9/15
3.0	Cathode	1166 ± 24	3.00026 ± 0.00024	0.01565 ± 0.00021	77.2/17

Table F.4: The amplitude a, position θ_0 and width σ_θ of a fit with a Gaussian distribution to the θ-distribution of Monte Carlo simulated data with a generated scattering angle of θ_{MC} and a 2 m larger distance between the first and the last silicon tracking station. The data of scattering processes at the anode and at the cathode are separated.

APPENDIX G

Additional figures for the Monte Carlo studies

In figure G.1, the φ-difference between the reconstruction in both detector systems to the initially simulated value is given.

In figure G.2, the kinetic energy reconstructed in the silicon tracking stations is drawn versus the initially generated energy. It is visible that the cut on the scattering angle reconstructed in the silicon tracking stations leads to a larger y-intercept and a smaller slope.

In figure G.3, the kinetic energy reconstructed in the TPC is drawn versus the initially generated energy. The cut on the scattering angle reconstructed in the silicon tracking stations has no impact on the results.

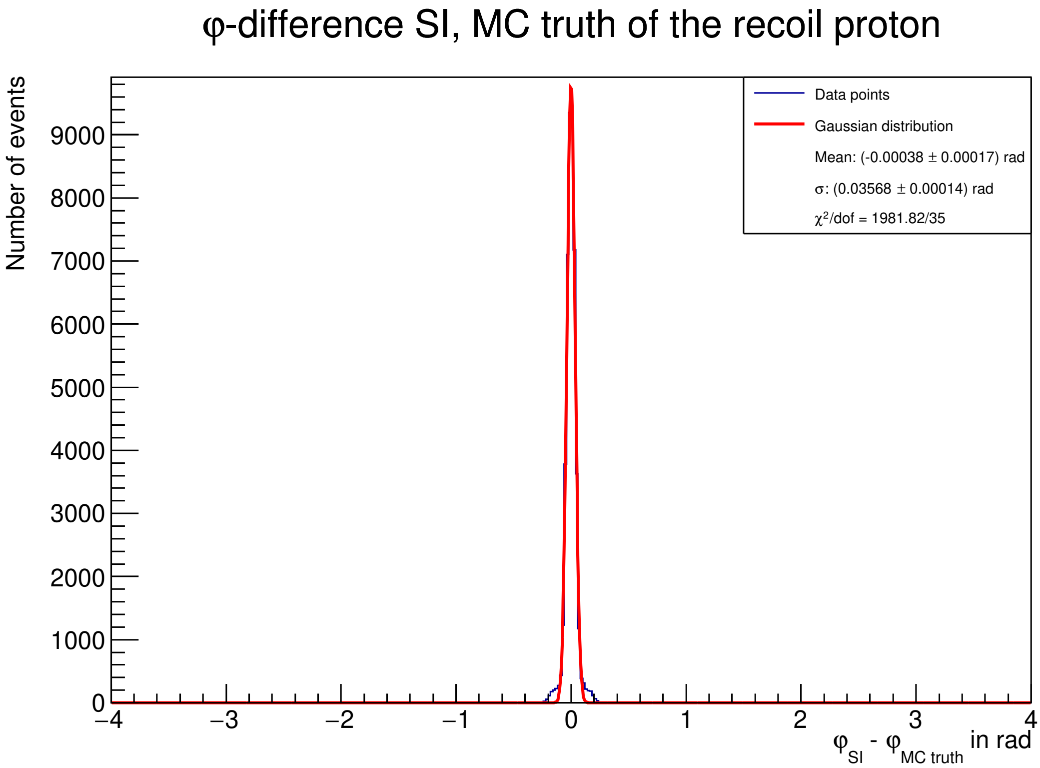

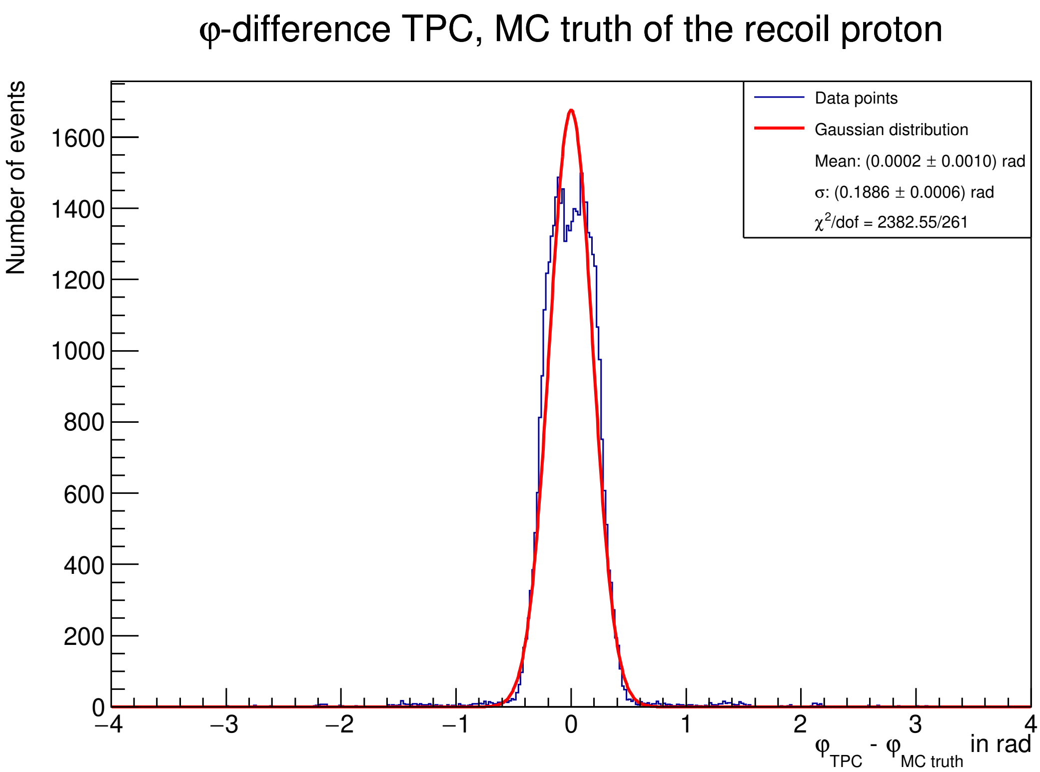

Figure G.1: The difference of the reconstructed φ-angle from the silicon tracking stations (left) and the TPC (right) to the MC truth φ.

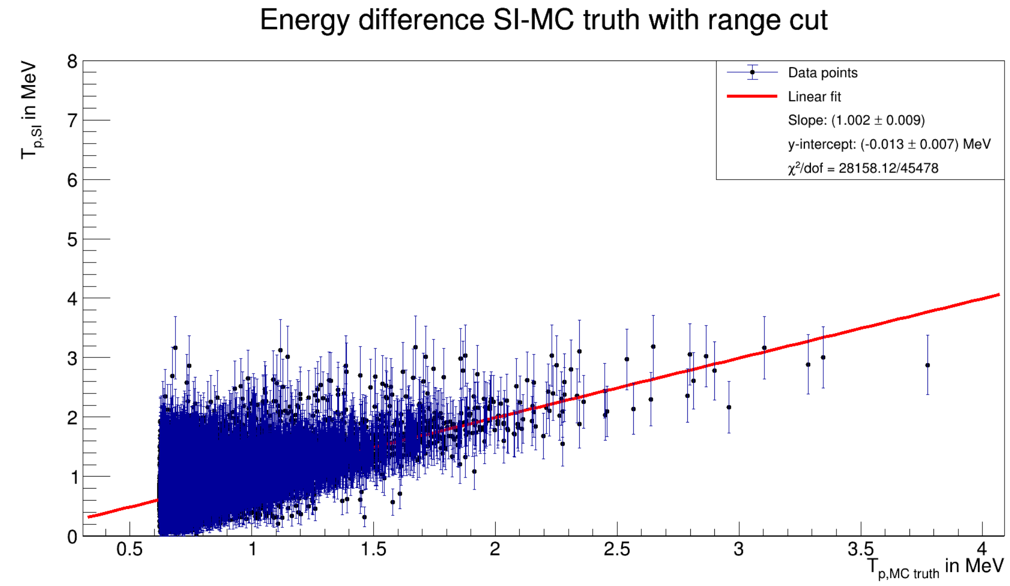

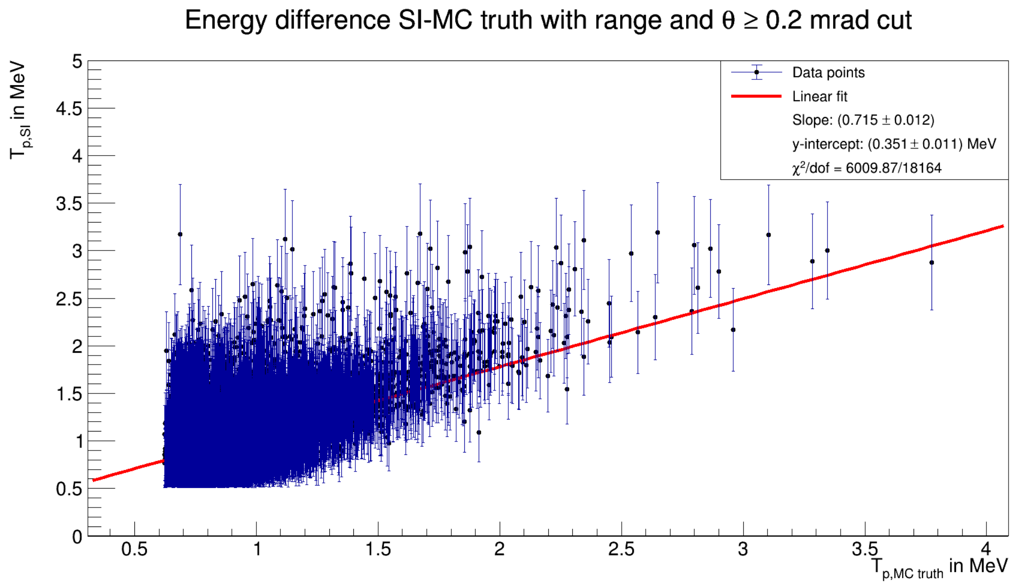

Figure G.2: The kinetic energy of the recoil proton reconstructed by the silicon tracking stations is plotted against the Monte Carlo truth energy. A linear regression is fitted to the data. The top plot has a slope which is comparable with 1, while the bottom plot has a cut on $\theta \geq 0.2$ mrad and the slope is much smaller than 1.

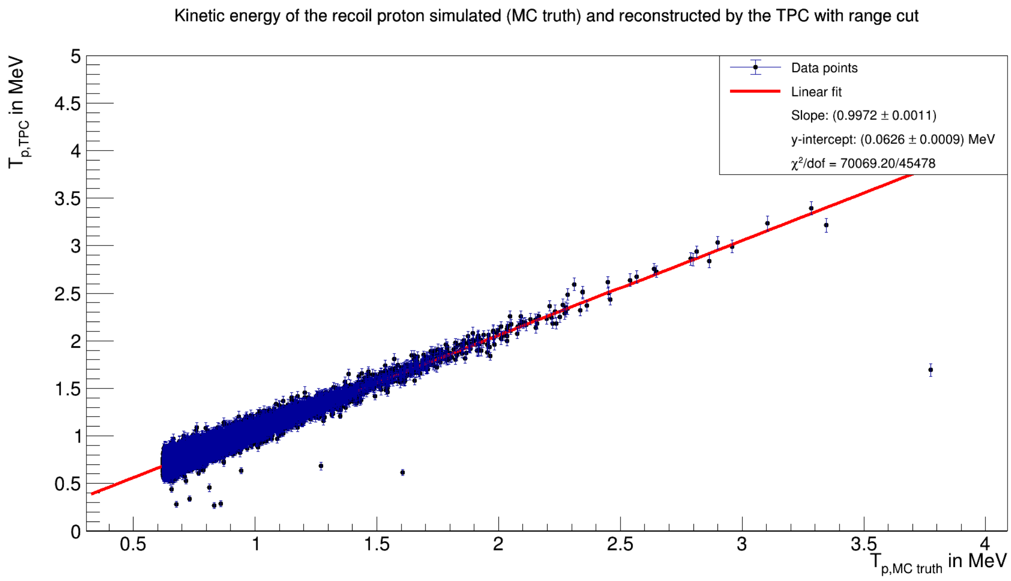

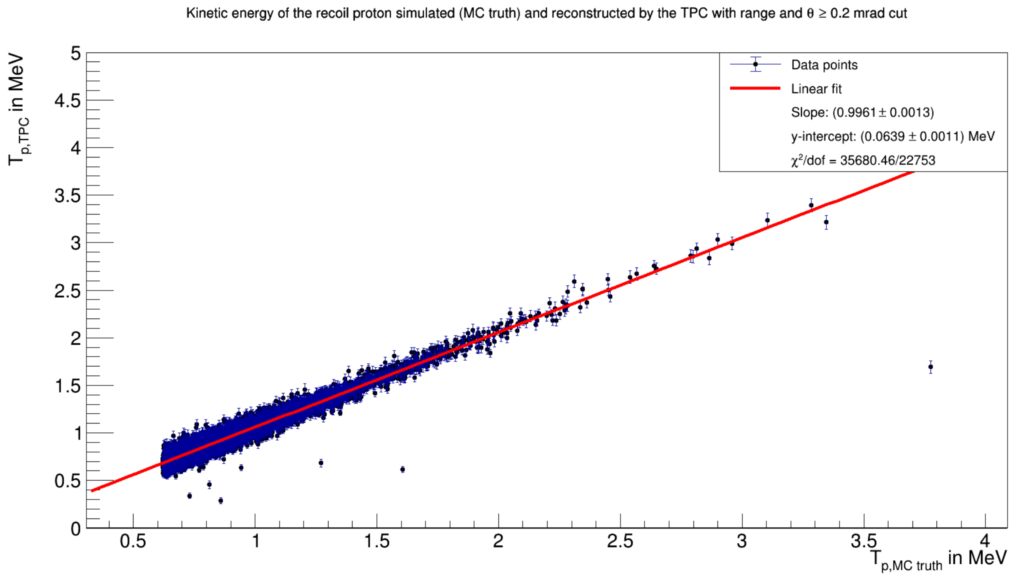

Figure G.3: The kinetic energy of the recoil proton is reconstructed by the TPC and given plotted against the Monte Carlo truth value. The top plot has no additional cut, while the bottom plot has an cut on the scattering angle $\theta \geq 0.2$ mrad.

List of Figures

List of Tables